

ARO-UR Center for

DTIC FILE COPY

2

AD-A218 427

OPTO-ELECTRONIC SYSTEMS RESEARCH

TECHNICAL REPORT

DYNAMICS AND INSTABILITIES IN  
HOMOGENEOUSLY BROADENED LASERS

Karl William Koch III

December 1989

The Institute of Optics  
University of Rochester

DISTRIBUTION STATEMENT A  
Approved for public release;  
Distribution Unlimited

Prepared for:

U.S. Army Research Office  
ATTN: DRXRO-IP-Library  
P. O. Box 12211  
Research Triangle Park, NC 27709

DTIC  
ELECTE  
FEB 26 1990  
S  
E  
D

90 02 26 192

UNCLASSIFIED  
SECURITY CLASSIFICATION OF THIS PAGE

REPORT DOCUMENTATION PAGE

1a. REPORT SECURITY CLASSIFICATION Unclassified		1b. RESTRICTIVE MARKINGS	
2a. SECURITY CLASSIFICATION AUTHORITY		3. DISTRIBUTION / AVAILABILITY OF REPORT Approved for public release; distribution unlimited.	
2b. DECLASSIFICATION / DOWNGRADING SCHEDULE		4. PERFORMING ORGANIZATION REPORT NUMBER(S)	
4. PERFORMING ORGANIZATION REPORT NUMBER(S)		5. MONITORING ORGANIZATION REPORT NUMBER(S) ARO 24626.127-PH-UIR	
6a. NAME OF PERFORMING ORGANIZATION University of Rochester	6b. OFFICE SYMBOL (if applicable)	7a. NAME OF MONITORING ORGANIZATION U. S. Army Research Office	
6c. ADDRESS (City, State, and ZIP Code) The Institute of Optics Rochester, New York 14627		7b. ADDRESS (City, State, and ZIP Code) P. O. Box 12211 Research Triangle Park, NC 27709-2211	
8a. NAME OF FUNDING / SPONSORING ORGANIZATION U. S. Army Research Office	8b. OFFICE SYMBOL (if applicable)	9. PROCUREMENT INSTRUMENT IDENTIFICATION NUMBER DAAL03-86-K-0173	
8c. ADDRESS (City, State, and ZIP Code) P. O. Box 12211 Research Triangle Park, NC 27709-2211		10. SOURCE OF FUNDING NUMBERS	
		PROGRAM ELEMENT NO.	PROJECT NO.
		TASK NO.	WORK UNIT ACCESSION NO.
11. TITLE (Include Security Classification) Dynamics and Instabilities in Homogeneously Broadened Lasers			
12. PERSONAL AUTHOR(S) Karl William Koch III			
13a. TYPE OF REPORT Technical	13b. TIME COVERED FROM TO	14. DATE OF REPORT (Year, Month, Day) December 1989	15. PAGE COUNT 146
15. SUPPLEMENTARY NOTATION The view, opinions and/or findings contained in this report are those of the author(s) and should not be construed as an official Department of the Army position, policy, or decision, unless so designated by other documentation.			
17. COSATI CODES		18. SUBJECT TERMS (Continue on reverse if necessary and identify by block number)	
FIELD	GROUP	SUB-GROUP	
		laser instability; chaos; modulation spectroscopy	
19. ABSTRACT (Continue on reverse if necessary and identify by block number) Please see Abstract on Page iv-v			
20. DISTRIBUTION / AVAILABILITY OF ABSTRACT <input type="checkbox"/> UNCLASSIFIED/UNLIMITED <input type="checkbox"/> SAME AS RPT. <input type="checkbox"/> DTIC USERS		21. ABSTRACT SECURITY CLASSIFICATION Unclassified	
22a. NAME OF RESPONSIBLE INDIVIDUAL Carlos R. Stroud, Jr.		22b. TELEPHONE (Include Area Code) 716-275-2598	22c. OFFICE SYMBOL

DTIC  
ELECTE  
FEB 26 1990  
S E D

**DYNAMICS AND INSTABILITIES IN HOMOGENEOUSLY BROADENED LASERS**

by

**Karl William Koch III**

**Submitted in Partial Fulfillment**

**of the**

**Requirements for the Degree**

**DOCTOR OF PHILOSOPHY**

**Supervised by Professor C. R. Stroud, Jr.**

**The Institute of Optics**

**University of Rochester**

**Rochester, New York**

**1989**

## CURRICULUM VITAE

The author was [REDACTED]. He grew up in New London, Connecticut, Kittery Point, Maine, Pearl City, Hawaii, and Poway, California. In the Fall of 1978 he entered San Diego State University and graduated with honors in the Spring of 1982 with a Bachelor of Science degree in Physics. In the Fall of 1982 he began graduate work in Optics at the Institute of Optics at the University of Rochester. His graduate research has been in the field of laser instabilities and has been directed by Professor Carlos R. Stroud, Jr. While at the University of Rochester, the author was a University Research Initiative fellow. He is also a member of the American Physical Society and the Optical Society of America.

Accession For	
NTIS GRA&I	<input checked="" type="checkbox"/>
DTIC TAB	<input type="checkbox"/>
Unannounced	<input type="checkbox"/>
Justification	
By	
Distribution/	
Availability Codes	
Dist.	Avail and/or Special
A-1	



## ACKNOWLEDGMENTS

I was fortunate enough to begin my graduate career with the assistance of Dr. Jerzy Krasinski in the laboratory. His immense knowledge and experience inspired me to work my hardest. I am also indebted to him and Zagorka Gaeta for the translation of a Russian manuscript. Without the well-equipped and philanthropic laboratory of Dr. Boyd, the execution, analysis, and summary of experiments reported in this thesis would not have been possible. I owe a great deal of thanks for the guidance, advice, physical insight, and clear-minded approach to problems that my advisor Dr. Stroud has given me.

It is with great pleasure that I acknowledge the positive influence the members of the 3<sup>rd</sup>-floor have had on my career, most notably Stephen Chakmakjian, Alex Gaeta, Dan Gauthier, Lloyd Hillman, Stephanos Papademetriou, Maurice Pessot, and John Yeazell. The optics community at the Institute has made life in Rochester an unforgettable experience.

The unconditional love and support of my family throughout my entire academic career has given me the strength to persevere; this is gratefully acknowledged.

I thank the University Research Initiative Army Research Office and the Joint Services Optics program for partially funding my research.

## ABSTRACT

This thesis describes theoretical and experimental studies of a homogeneously broadened ring dye laser. The thesis is particularly concerned with the two-frequency instability in which a bichromatic field emerges from the laser above the instability threshold. The interaction of a bichromatic field with an isolated atomic resonance is examined. The time-averaged inversion and the saturated gain exhibit structure in the form of a series of subharmonic resonances. The stability of a strong bichromatic laser field to the growth of a subharmonic probe field is examined. The gain of the subharmonic bichromatic probe field in the presence of the strong bichromatic laser field is calculated. The strong bichromatic field is stable to the growth of the subharmonic fields when the modulation frequency of the strong field coincides with the Rabi frequency of the lasing transition.

The existence of chaos in a strongly driven nonlinear system is experimentally investigated in a multimode ring dye laser. A dye laser is pumped with a modulated pump source. The response of the dye laser to commensurate and incommensurate modulations is reported. We find that for commensurate modulations, the dye laser responds in a periodic fashion and the rf spectrum of the dye laser is composed of a series of harmonics. For incommensurate mod-

ulations, the dye laser responds in a quasiperiodic fashion with a broadband rf spectrum.

The two-frequency instability in a multimode cw-pumped ring dye laser is shown to occur in a number of cavity configurations. The two-frequency instability is shown to exhibit a sensitive dependence on the cavity detuning.

The recently proposed band model of the laser is examined and theoretical predictions of the model are experimentally analyzed. Experimental evidence is presented which illustrates that conventional theories for two-, three-, and four-level lasers are inadequate to describe the excited state population dynamics of a cw dye laser. Modulation spectroscopy is used in a new signal-limited technique to measure an upper bound on the decay time of the lower levels in a rhodamine-6G dye molecule.

## TABLE OF CONTENTS

	<b>Page</b>
Curriculum Vitae	ii
Acknowledgments	iii
Abstract	iv
Table of Contents	vi
List of Figures	viii
Publications	xii
Presentations	xiv
<b>I. Introduction</b>	<b>1</b>
<b>II. Externally Driven Systems</b>	<b>8</b>
1. Introduction	8
2. Bloch Equations for a Bichromatic Field	9
3. Stationary State Response	12
4. Analysis and Results	15
5. Subharmonic Probe Field	25
<b>III. Modulation Mixing in a Multimode Dye Laser</b>	<b>36</b>
1. Introduction	36
2. Experimental Setup	41
3. Experimental Analysis	43
4. Experimental Results	46
5. Conclusions	57



<b>IV. Dye Laser Experiments</b>	<b>59</b>
1. Introduction	59
2. Robustness of the Two-Frequency Instability	60
3. Effects of Detuning	71
<b>V. The Band Model for Dye Lasers</b>	<b>76</b>
1. Introduction	76
2. The Band Model	79
3. Single-Frequency Steady State Solutions	86
4. Continuum Limit	89
5. Lorentzian and Flat Oscillator Strengths	90
6. Two-Frequency Steady State Solutions	93
7. Lorentzian and Flat Oscillator Strengths	97
<b>VI. Band Model Experiments</b>	<b>100</b>
1. Introduction	100
2. Analysis and Results of Inversion Clamping	103
3. Modulation Spectroscopy of Lower Levels	111
4. Analysis and Results	115
5. Conclusions	117
<b>Summary</b>	<b>123</b>
<b>Appendix A</b>	<b>126</b>
1. Multimode Rate Equation Stability Analysis	129
2. Multimode Maxwell-Bloch Equation Stability Analysis	132
<b>References</b>	<b>139</b>

## List of Figures

Figure	Titles	Page
Fig. 2.1	Time-averaged inversion of a collisionally broadened medium as a function of modulation frequency for a series of bichromatic field intensities.	16
Fig. 2.2	Time-averaged inversion of a radiatively broadened medium as a function of modulation frequency for a series of bichromatic field intensities.	18
Fig. 2.3	(a) Time-averaged inversion of a collisionally broadened medium as a function of modulation frequency for large bichromatic field amplitude. (b) Time-averaged inversion of a radiatively broadened medium as a function of modulation frequency for large bichromatic field amplitude. (c) Time-averaged inversion of a system undergoing strong collisions as a function of modulation frequency for large bichromatic field amplitude.	20
Fig. 2.4	Peak positions of the time-averaged inversion as a function of modulation frequency and bichromatic field amplitude.	22
Fig. 2.5	Time-averaged inversion as a function of bichromatic field amplitude for a fixed modulation frequency.	23
Fig. 2.6	(a) Real part of the second harmonic component of the inversion as a function of modulation frequency for a series of bichromatic field intensities. (b) Imaginary part of the second harmonic component of the inversion as a function of modulation frequency for a series of bichromatic field intensities. (c) Magnitude of the second harmonic component of the inversion as a function of modulation frequency for a series of bichromatic field intensities.	24
Fig. 2.7	Applied field spectrum for the $\frac{1}{2}$ -subharmonic probe field and strong bichromatic field.	26
Fig. 2.8	(a) Gain of the in-phase $\frac{1}{2}$ -subharmonic probe field as a function of modulation frequency for a series of strong-field intensities. (b) Gain of the in-quadrature $\frac{1}{2}$ -subharmonic probe field as a function of modulation frequency for a series of strong-field intensities.	32

Fig. 2.9	Gain of the in-phase and in-quadrature $\frac{1}{2}$ -subharmonic probe fields and the gain of the strong bichromatic field as a function of modulation frequency.	34
Fig. 3.1	Dye laser output power versus normalized pump power for a high-Q multimode ring dye laser.	40
Fig. 3.2	Experimental setup to observe modulation mixing in a high-Q multimode ring dye laser.	42
Fig. 3.3	(a) Logarithm of the correlation sum $C_n(\epsilon)$ as a function of the logarithm of the hypersphere radius for the time series of the pump laser modulated at three commensurate frequencies. (b) Logarithm of the correlation sum $C_n(\epsilon)$ as a function of the logarithm of the hypersphere radius for the time series of the dye laser driven by the pump laser modulated at three commensurate frequencies.	47
Fig. 3.4	(a) The slopes of the curves in Fig. (3.3a) derived from a 13-point linear regression analysis. (b) The slopes of the curves in Fig. (3.3b) derived from a 13-point linear regression analysis.	49
Fig. 3.5	(a) Correlation dimension, $D_2(n)$ , as a function of the embedding dimension for the case of three commensurate frequencies. (b) Order-2 Renyi entropy, $K_2(n)$ , as a function of the embedding dimension for the case of three commensurate frequencies.	50
Fig. 3.6	(a) Fourier transform of the time series for the pump laser modulated at three commensurate frequencies. (b) Fourier transform of the time series for the dye laser driven by the pump laser modulated at three commensurate frequencies.	51
Fig. 3.7	(a) Logarithm of the correlation sum $C_n(\epsilon)$ as a function of the logarithm of the hypersphere radius for the time series of the pump laser modulated at three incommensurate frequencies. (b) Logarithm of the correlation sum $C_n(\epsilon)$ as a function of the logarithm of the hypersphere radius for the time series of the dye laser driven by the pump laser modulated at three incommensurate frequencies.	53
Fig. 3.8	(a) The slopes of the curves in Fig. (3.7a) derived from a 13-point linear regression analysis. (b) The slopes of the curves in Fig. (3.7b) derived from a 13-point linear regression analysis.	54

Fig. 3.9	(a) Correlation dimension, $D_2(n)$ , as a function of the embedding dimension for the case of three incommensurate frequencies. (b) Order-2 Renyi entropy, $K_2(n)$ , as a function of the embedding dimension for the case of three incommensurate frequencies.	55
Fig. 3.10	(a) Fourier transform of the time series for the pump laser modulated at three incommensurate frequencies. (b) Fourier transform of the time series for the dye laser driven by the pump laser modulated at three incommensurate frequencies.	56
Fig. 4.1	Experimental setup to observe dye laser spectra as a function of pump power.	63
Fig. 4.2	Optical spectrum of the bidirectional ring dye laser as a function of pump power.	65
Fig. 4.3	Optical spectrum of the unidirectional ring dye laser as a function of pump power.	67
Fig. 4.4	Schematic diagram of a cw pumped multimode ring dye laser with Faraday rotator.	68
Fig. 4.5	Optical spectrum of the bidirectional ring dye laser as a function of pump power.	69
Fig. 4.6	Optical spectrum of the unidirectional ring dye laser as a function of pump power.	70
Fig. 4.7	The effects of cavity detuning on the two-frequency instability.	73
Fig. 4.8	Giant mode splitting in a ring dye laser.	75
Fig. 5.1	Energy level diagram for the band model atom.	81
Fig. 5.2	Excited state population as a function of pump parameter in the continuum limit of the band model for the flat-oscillator-strength approximation.	92
Fig. 5.3	Dimensionless laser intensity as a function of pump parameter in the continuum limit of the band model for the flat-oscillator-strength approximation.	94

Fig. 5.4	Total inversion as a function of pump parameter in the continuum limit of the band model for the flat-oscillator-strength approximation.	96
Fig. 6.1	Experimental setup to observe the absence of inversion clamping in a cw pumped multimode dye laser.	102
Fig. 6.2	Energy level diagram for a three-level laser medium.	104
Fig. 6.3	$\chi^2$ for the experimental data versus the parameter $w_0$ for the best fits to $w_0$ and $\tau_a$ to three-level laser theory.	107
Fig. 6.4	$\chi^2$ for the experimental data versus the parameter $\tau_a$ for the best fits to $w_0$ and $\tau_a$ to three-level laser theory.	108
Fig. 6.5	Best fits of $w_0$ versus $\tau_a$ for the experimental data fit to three-level laser theory.	109
Fig. 6.6	Fluorescence versus pump power from a cw pumped multimode dye laser.	112
Fig. 6.7	Best fits of $\tau_a$ versus $d_{th}$ for the experimental data fit to band model laser theory.	114
Fig. 6.8	Fluorescence versus pump power from a cw pumped multimode dye laser.	118
Fig. 6.9	Experimental setup for fluorescence modulation spectroscopy experiment.	119
Fig. 6.10	Magnitude of the first harmonic component of the excited state population driven by a weakly modulated pump for series of $\tau_a$ -values.	120
Fig. 6.11	Magnitude of the first harmonic component of the fluorescence from dye molecules driven by a weakly modulated single-mode argon-ion laser.	121

## PUBLICATIONS

- [1] Karl Koch, Stephen H. Chakmakjian, Stephanos Papademetriou, and C. R. Stroud, Jr., "Excited-State Relaxation Dynamics in a Continuous-Wave Dye Laser," Proceedings of the Coherence and Quantum Optics VI conference (Plenum, New York, NY).
- [2] Stephen H. Chakmakjian, Stephanos Papademetriou, Karl Koch, Michael Noel, and C. R. Stroud, Jr., "Near Threshold Behavior of Multimode Continuous-wave Dye Lasers with an Amplitude-Modulated Pump," Proceedings of the Coherence and Quantum Optics VI conference (Plenum, New York, NY).
- [3] Stephen H. Chakmakjian, Karl Koch, Stephanos Papademetriou, and C. R. Stroud, Jr., "Effects of Pump Modulation on a Four-Level Amplifier," J. Opt. Soc. Amer. B **6**, 1746-1751 (1989).
- [4] Stephen H. Chakmakjian, Stephanos Papademetriou, Karl Koch, and C. R. Stroud, Jr., "Near-Threshold Behavior of Multimode CW Dye Lasers with Amplitude-Modulated Pump," Phys. Rev. A **40**, 1858-1867 (1989).
- [5] Karl Koch, Stephen H. Chakmakjian, Stephanos Papademetriou, and C. R. Stroud, Jr., "Modulation Mixing in a Multimode Dye Laser," Phys. Rev. A **39**, 5744-5750 (1989).
- [6] Karl Koch, Brian J. Oliver, Stephen H. Chakmakjian, C. R. Stroud, Jr., and Lloyd W. Hillman, "Subharmonic Instabilities in Resonant Interactions with Bichromatic Fields," J. Opt. Soc. Amer. B **6**, 58-65 (1989).
- [7] Stephen H. Chakmakjian, Karl Koch, and C. R. Stroud, Jr., "Observation of Resonances at Subharmonics of the Rabi Frequency in the Saturated Absorption of a 100% Amplitude Modulated Laser Beam," J. Opt. Soc.

Amer B 5, 2015-2020 (1988).

- [8] C. R. Stroud, Jr., Karl Koch, Stephen H. Chakmakjian, and Lloyd W. Hillman, "Multimode Instabilities in CW Dye Lasers," *Optical Chaos*, J. Chrostowski, N. B. Abraham, Editors, Proc. SPIE 667, 47-50 (1986).
- [9] Stephen H. Chakmakjian, Lloyd W. Hillman, Karl Koch, and C. R. Stroud, Jr., "Multimode Instabilities of Homogeneously Broadened Lasers", *Optical Bistability*, Edited by H. M. Gibbs, P. Mandel, N. Peyghambarian, and S. D. Smith (Springer-Verlag, Berlin, 1986).
- [10] Lloyd W. Hillman and Karl Koch, "Multimode Instabilities in Homogeneously Broadened Lasers," *Optical Instabilities*, Edited by R. W. Boyd, M. G. Raymer, and L. M. Narducci (Cambridge Press, Cambridge, 1986).
- [11] C. R. Stroud, Jr., Karl Koch, and Stephen H. Chakmakjian, "Instabilities and Higher-Order States of CW Ring Dye Lasers," *Optical Instabilities*, Edited by R. W. Boyd, M. G. Raymer, and L. M. Narducci (Cambridge Press, Cambridge, 1986).
- [12] Lloyd W. Hillman, Jerzy Krasinski, Karl Koch, and C. R. Stroud, Jr., "Dynamics of Homogeneously Broadened Lasers: Higher-Order Bichromatic States of Operation," *J. Opt. Soc. Amer. B* 2, 211-217 (1985).

## PRESENTATIONS

- [1] Karl Koch, Stephen H. Chakmakjian, Stephanos Papademetriou, and C. R. Stroud, Jr., "Excited-State Relaxation Dynamics in Dye Lasers," Sixth Rochester Conference on Coherence and Quantum Optics, Rochester, New York, June 1989.
- [2] Stephen H. Chakmakjian, Stephanos Papademetriou, Karl Koch, and C. R. Stroud, Jr., "Near-Threshold Behavior of Multimode CW Dye Lasers with Amplitude Modulated Pump," Sixth Rochester Conference on Coherence and Quantum Optics, Rochester, New York, June 1989.
- [3] Stephen H. Chakmakjian, Karl Koch, Stephanos Papademetriou, and C. R. Stroud, Jr., "Homogeneous Hole Burning in an Inverted System," Annual Meeting of the Optical Society of America, Santa Clara, California, October 1988.
- [4] Stephen H. Chakmakjian, Karl Koch, and C. R. Stroud, Jr., "Incoherent Pump Effects in AM Spectroscopy," Annual Meeting of the Optical Society of America, Rochester, New York, October 1987.
- [5] Karl Koch, Stephen H. Chakmakjian, C. R. Stroud, Jr., and Lloyd W. Hillman, "Broadband Atomic Response to Incommensurate Modulation Frequencies," Annual Meeting of the Optical Society of America, Rochester, New York, October 1987.
- [6] Karl Koch, Brian J. Oliver, C. R. Stroud, Jr., and Lloyd W. Hillman, "Subharmonic Instabilities in Resonant Interactions with Bichromatic Fields," Annual Meeting of the Optical Society of America, Rochester, New York, October 1987.
- [7] Stephen H. Chakmakjian, Karl Koch, C. R. Stroud, Jr., and Lloyd W. Hill-



- man, "Resonance Fluorescence with Modulated Excitation," Annual Meeting of the Optical Society of America, Rochester, New York, October 1987.
- [8] Stephen H. Chakmakjian, Karl Koch, C. R. Stroud, Jr., "Multi-Level Dynamics in a Rhodamine 6G Dye Laser," International Workshop on Instabilities, Dynamics, and Chaos in Nonlinear Optical Systems, Il Ciocco, Lucca Italy, July 1987.
- [9] Karl Koch, Stephen H. Chakmakjian, Lloyd W. Hillman, and C. R. Stroud, Jr., "Effects of Detuning on Laser Instabilities," Annual Meeting of the Optical Society of America, Seattle, Washington, October 1986.
- [10] C.R. Stroud, Jr., Karl Koch, Stephen H. Chakmakjian, and Lloyd W. Hillman, "Multimode Instabilities in CW Dye Lasers," SPIE meeting on Optical Chaos, Québec City, Canada, June 1986.
- [11] Stephen H. Chakmakjian, Lloyd W. Hillman, Karl Koch, and C. R. Stroud, Jr., "Multimode Instabilities of Homogeneously Broadened Lasers," Topical Meeting on Optical Bistability, Tucson, Arizona, December 1985.
- [12] Karl Koch, Lloyd W. Hillman, and C. R. Stroud, Jr., "Multimode Instabilities in Homogeneously Broadened Lasers," Annual Meeting of the Optical Society of America, Washington, D. C., October 1985.
- [13] C. R. Stroud, Jr., Karl Koch, and Stephen H. Chakmakjian, "Instabilities and Higher-Order States of CW Ring Dye Lasers," International Meeting on Instabilities and Dynamics of Lasers and Nonlinear Optical Systems, Rochester, New York, June 1985.
- [14] Lloyd W. Hillman and Karl Koch, "The Source of Multimode Instabilities in Homogeneously Broadened Lasers," International Meeting on Instabilities and Dynamics of Lasers and Nonlinear Optical Systems, Rochester, New

York, June 1985.

- [15] Lloyd, W. Hillman, Jia-Yong Yuan, Karl Koch, Jerzy Krasinski, and C. R. Stroud, Jr., "Behavior of Homogeneously Broadened Lasers Operating Far Above Threshold," XIII International Quantum Electronics Conference, Anaheim, California, June 1984.

## Chapter I

### INTRODUCTION

#### 1. Introduction

Instabilities in lasers have existed since the first demonstration of the laser by Maiman<sup>1</sup>. Maiman's ruby laser exhibited fluctuations and spiking in the output intensity that, to this day, are not well understood. Initially the spiking and noise were attributed to the pulsed nature of the pumping mechanism. However, several authors subsequently demonstrated<sup>2-3</sup> that a ruby laser operated with a continuous-wave pump still displays fluctuations and spiking in the output intensity. A simple theory<sup>4</sup> containing the inversion of a two-level atomic system and the field intensity was developed to understand this behavior. That model has come to be known as the rate equation model. Somewhat later it was shown<sup>5-6</sup> that the rate equation model does not allow time-dependent solutions in the stationary state; therefore, the model is inadequate for explaining the behavior of the ruby laser. The possibility that coherent effects were responsible for the experimental features motivated the derivation of a more rigorous model<sup>7</sup> containing the inversion and coherent polarization of a two-level system,

and the electric field amplitude, even though these equations had been previously derived<sup>8</sup> in maser theory. The set of equations describing this coherent theory is now known as the Maxwell-Bloch equations. It can be shown that, in the limit where the atomic polarization relaxation rate is much faster than any other rate in the system, the Maxwell-Bloch equations reduce to those of the rate equation model. Instabilities in lasers and laser theory have continued to change and progress, developing a better understanding of lasers and the nonlinear dynamics inherent in their behavior.

The theoretical analysis of lasers is greatly simplified if the electric field in the laser consists of a single cavity mode. Furthermore, the analysis is greatly simplified if all the atoms are treated identically, as in a homogeneously broadened medium. While the rate equation model predicts that the steady state operation will always be stable to perturbative fluctuations, the Maxwell-Bloch equations predict<sup>9-12</sup> that in the bad cavity limit (i.e., where the cavity decay rate exceeds the sum of the polarization and inversion decay rates), the steady state will become unstable above a definite threshold value of the pump parameter. Numerical integrations<sup>13-14</sup> of the equations above this threshold reveal pulsing behavior which develops into chaotic fluctuations. Weiss and coworkers<sup>15-18</sup> have observed many of these features experimentally with a single-mode far-infrared ammonia laser.

Some laser media cannot be treated as homogeneously broadened transitions. The transition frequency of atoms in a gas exhibits a velocity-dependent shift. Since the gas of atoms contains a distribution of velocities, the medium contains a distribution of transition frequencies. Similarly, atoms embedded in the amorphous structure of glass experience different local fields and therefore

different Stark shifts of their energy levels. These different Stark shifts cause a distribution of transition frequencies in the laser medium. These and other aspects require the transition be treated as inhomogeneously broadened. In the analysis of an inhomogeneously broadened medium, the medium is treated as an ensemble of homogeneously broadened atoms with a distribution of resonance frequencies. Inhomogeneous broadening can greatly reduce the threshold for instability. The complex dispersion profile generated by spectral hole burning<sup>19</sup> allows for the possibility of more than one frequency oscillating in the same cavity mode.<sup>20-21</sup> In addition, the frequency of the cavity mode depends on the intensity of the field in the mode.<sup>22</sup> For high-gain lasers it is possible for three different frequencies to coexist in the same cavity mode without spectral hole burning.<sup>23-25</sup> Many of these features have been experimentally verified in He-Xe lasers by Casperson and coworkers<sup>20</sup> and Abraham and coworkers.<sup>21,26-27</sup>

There are many lasers that do not operate in a single mode. The cavity mode spacing of a one-meter ring laser is 300 MHz, which is much less than typical laser linewidths. So a laser with a 1 GHz linewidth in a one-meter ring laser would have about three modes under the gain profile. For dyes, alexandrite, titanium-sapphire, semiconductors or similar lasers, with gain bandwidths on the order of hundreds of angstroms, there are hundreds of modes under the gain profile for typical cavity lengths. It is normally the case, rather than the exception, that the cavity mode spacing is much less than the gain bandwidth. Due to this fact, most lasers operate in a multimode fashion. The multimode Maxwell-Bloch equations predict<sup>9-12</sup> that the steady state solution will become unstable above a threshold value of the pump parameter. Numerical integrations of the equations<sup>10,28-29</sup> above this threshold reveal mode locked pulsed

solutions. In Appendix A we discuss the stability analysis of the multimode rate equations and the multimode Maxwell-Bloch equations. There are at least two distinct types of solutions above this threshold. Numerical integration of the equations near the threshold to determine which solution the system will prefer suffer from numerical roundoff errors. Numerical roundoff in regions of instability - where the system is extremely sensitive to initial conditions - can give incorrect answers. Experimental investigation of this point is much more revealing. However, experimentally no one has convincingly observed this instability.

In addition to spectral inhomogeneities, there are also spatial inhomogeneities that complicate and enrich the dynamics of unstable lasers. Spatial inhomogeneities can be caused by counterpropagating fields in a laser. The interference of two counter propagating fields produces a standing-wave pattern with nodes in the field every half wavelength. The atoms of the gain media at these nodes do not experience the laser field. If the gain medium is thin compared with the cavity length, it is possible for two modes to form standing-wave patterns that are  $180^\circ$  out of phase across the entire gain medium. This feature has been studied in pulsed<sup>30</sup> and continuous-wave<sup>31</sup> dye lasers and has been exploited in building stabilized continuous-wave dye lasers.<sup>32</sup> The dynamics and statistics of a two-mode bidirectional laser has been extensively studied by Mandel and coworkers<sup>33-38</sup>.

Spatial inhomogeneities can also exist in the transverse direction. The study of transverse mode behavior has only recently begun to receive attention. The problem is extremely complicated due to the nonuniform character of Gaussian beams.

Quite recently, the homogeneously broadened systems whose lower level consists of a band of levels have drawn considerable attention.<sup>39-41</sup> The lower band of levels provides a large gain bandwidth which is useful for resonant light studies and short pulse production and amplification. Examples of such systems include dyes, CO<sub>2</sub>, alexandrite, semiconductor, and titanium-sapphire. The equations and the dynamics of such a system are different from both a two-level homogeneously broadened system and a two-level inhomogeneously broadened system. Though the behavior is not well understood, the theoretical model of such a system predicts<sup>39-42</sup> a series of instabilities with definite thresholds. Stroud and coworkers<sup>43-45</sup> have seen many of the predicted features experimentally in a continuous-wave dye laser. Two-frequency operation similar to that observed in the dye laser has also been observed in an argon-ion laser and a Nd:glass laser. This is interesting since the dye laser transition is predominantly homogeneously broadened system, while the argon-ion<sup>46-48</sup> and Nd:glass<sup>49</sup> laser transitions are inhomogeneously broadened.

Laser instabilities are intrinsically nonlinear. Even the simple case of the rate equations, where the polarization adiabatically follows the inversion and field intensity, is nonlinear. Nonlinear systems represented by only a few degrees of freedom, can display extreme sensitivity to initial conditions. Two initially closely spaced points in phase space can separate exponentially as a function of time. This behavior is called chaos. Universal routes mark the transition from regular to chaotic behavior. Lasers represent an ideal system for examining such universal behavior. In addition, much that has been learned in other fields can be used to better understand laser dynamics. For instance, the single-mode Maxwell-Bloch equations are identical, via a simple transformation of

variables,<sup>50-51</sup> to the equations that model convective flow, which have been extensively studied numerically by Lorenz.<sup>52</sup>

The Maxwell-Bloch equations derive their name from Maxwell's reduced wave equation, which describes how a field propagates in space and time and is driven by a macroscopic polarization density, and the Bloch equations, which describe how a two-level system interacts with a near-resonant coherent field. The atomic polarization acts as a source term in the wave equation, producing a field; the field in turn, drives the atoms and induces a polarization. When the atomic response induced by the field is the same atomic response that radiates the field, the solution is termed self consistent. Instabilities in self-consistent systems result from changing a parameter of the system. Instabilities can also be investigated in driven systems. For instance, one could analyze the behavior of atoms in a cavity driven by an external field. We conduct both types of experiments on the dye laser.

This thesis is a continuation of the work on the two-frequency instability originally observed by Hillman<sup>54</sup>. The original work demonstrated the instability had a low instability threshold (about 2 times above threshold), exhibited discontinuous jumps in the output intensity and hysteresis at the instability thresholds, spectral splitting proportional to the field amplitude, another instability threshold about 4 times above threshold, and unclear behavior above this second threshold. The aim of the current thesis research was to learn more about this instability, develop a quantitative understanding of these phenomena in terms of laser theory, and to explore the connection between this instability and chaos. We have been successful in some of these quests and others remain elusive.



In chapter II we examine the theoretical approach to analyzing driven systems. In particular we will investigate two- and four-mode fields driving two-level atoms. These two examples are instructive as they illustrate the solution of recurrence relations using scalar and matrix continued fractions, respectively. We also discuss the complications of incommensurate frequencies in the driving field. Then in chapter III, we discuss the results of an experiment of a nonlinear system driven by commensurate and incommensurate driving frequencies. We also discuss how one characterizes a time series and distinguishes between chaotic and quasiperiodic behaviors. In chapter IV we present results of an experimental investigation of a multimode continuous-wave dye laser. In chapter V we will discuss the theoretical approach taken to analyze lasers and their stability. Then in chapter VI, we discuss some experiments that were performed to examine the dye laser using the band model and four-level laser theory.

## Chapter II

### EXTERNALLY DRIVEN SYSTEMS

#### 1. Introduction

In this chapter, we discuss the solutions of the equations describing externally driven systems. We will be particularly concerned with two-level systems interacting with multifrequency fields. These problems can often be formulated as infinite-dimensional matrix diagonalization problems. We illustrate how the solutions to these problems are generated in terms of continued fractions.

*A great deal of insight into the physical dynamics of atoms interacting with light has been gained from considering the interaction of an isolated atomic resonance with an optical field.<sup>53</sup> A real atom has many optical transitions; however, when only one allowed-transition frequency is close to the optical frequency of the light field, the atom can be well-approximated as a two-level atom. This model has been extensively studied and continues to reveal new and fascinating dynamics in its interaction with cavities and fields.*

Theoretical studies of two-level atoms interacting with coherent fields can be used to better understand a laser's dynamics. A general solution to the set

of differential equations describing a multimode laser has not been found. Even if a solution did exist, it would be difficult to obtain physical insight from such a solution because of the large parameter space. Numerical integrations of the equations are also hindered by the large parameter space; in addition, digital computations can give incorrect results in regions of instability where the system is sensitive to perturbations and noise. An alternative method to examining the dynamics of a laser is to calculate the gain of a probe field in the presence of a strong laser field. The gain of the strong laser field clamps to the loss in steady state. When the gain of the probe field exceeds the gain of the strong laser field, it also exceeds the losses and therefore, the probe field can begin to oscillate. When the probe field begins to oscillate, the steady state solution is no longer stable. With this in mind, we calculate the gain of a strong bichromatic field and the gain of a probe field in the presence of a strong field.

## 2. Bloch Equations for a Bichromatic Field

To define a notation, we begin by considering the expression for the optical field

$$\begin{aligned} E(t) &= (\mathcal{E}'(t) + i\mathcal{E}''(t)) \exp(i\omega t) + (\mathcal{E}'(t) - i\mathcal{E}''(t)) \exp(-i\omega t) \\ &= 2\mathcal{E}'(t) \cos \omega t - 2\mathcal{E}''(t) \sin \omega t. \end{aligned} \quad (2.1)$$

We assume that the time rate of change of the amplitudes of the quadratures is much slower than the optical frequency (i.e.,  $|\dot{\mathcal{E}}'| \ll \omega|\mathcal{E}'|$  and  $|\dot{\mathcal{E}}''| \ll \omega|\mathcal{E}''|$ ). The Bloch equations model the response of a two-level atom coherently driven by an optical field. In a reference frame rotating at the frequency  $\omega$ , the optical Bloch equations under the rotating-wave approximation are<sup>53-54</sup>

$$\frac{d}{dt} \begin{bmatrix} u \\ v \\ w \end{bmatrix} = \begin{bmatrix} -1/T_2 & -\Delta & -\Omega''(t) \\ \Delta & -1/T_2 & \Omega'(t) \\ \Omega''(t) & -\Omega'(t) & -1/T_1 \end{bmatrix} \begin{bmatrix} u \\ v \\ w \end{bmatrix} + \begin{bmatrix} 0 \\ 0 \\ w_{eq}/T_1 \end{bmatrix}. \quad (2.2)$$

The slowly varying amplitude of the in-phase (in-quadrature) part of the dipole moment is  $u$  ( $v$ ); the atomic inversion (i.e., the excited-state population minus the ground-state population) is  $w$ ;  $\Delta = \omega_0 - \omega$  is the detuning between the rotating-frame frequency  $\omega$  and the atomic transition frequency  $\omega_0$ ; the exponential decay time of the inversion (polarization) is  $T_1$  ( $T_2$ ). Without a coherent driving field, the inversion relaxes to its equilibrium value,  $w_{eq}$ . The two Rabi frequencies,  $\Omega'(t)$  and  $\Omega''(t)$ , are related to the slowly-varying amplitudes of the electric field

$$\Omega'(t) = 2d\mathcal{E}'(t)/\hbar, \quad (2.3a)$$

$$\Omega''(t) = 2d\mathcal{E}''(t)/\hbar, \quad (2.3b)$$

where  $d$  is the dipole moment matrix element between the two levels and  $\hbar$  is Planck's constant divided by  $2\pi$ . For sufficiently strong constant-amplitude fields (i.e.,  $\Omega > 1/T_2$ ) the solutions to these equations display oscillations that decay to constant steady state solutions.

If the amplitude,  $\mathcal{E}'(t)$  in Eqn. (2.1) is sinusoidally modulated so that we may write  $\mathcal{E}'(t) = \mathcal{E}_0 + 2\delta\mathcal{E}_1 \cos \delta\omega t$ , then the spectrum of the field  $E$  contains three frequency components. These components are identified by using a simple trigonometric relationship to write

$$\begin{aligned} E(t) &= 2\mathcal{E}(t) \cos \omega t \\ &= 2\mathcal{E}_0 \cos \omega t + 4\delta\mathcal{E}_1 \cos \delta\omega t \cos \omega t \\ &= 2\mathcal{E}_0 \cos \omega t + 2\delta\mathcal{E}_1 \cos[(\omega + \delta\omega)t] + 2\delta\mathcal{E}_1 \cos[(\omega - \delta\omega)t] \end{aligned} \quad (2.4)$$

This equation illustrates that sinusoidal modulation of the amplitude produces new field components shifted from the carrier frequency  $\omega$  by the modulation

frequency  $\delta\omega$ . If the modulation takes the intensity to zero, then all the energy goes into the sidebands and the carrier is suppressed. We refer to this two-frequency field as 100% amplitude modulated (AM).

The problem of a bichromatic field interacting with a two-level atom is important to instabilities in dye lasers. Hillman *et al.*<sup>43</sup>, observed a bichromatic field in a dye laser above a second instability threshold. The interaction of a two-frequency field with an isolated atomic resonance is also important to fundamental questions in quantum electrodynamics. Unlike monochromatic excitation, the stationary state response of the atomic system driven by a bichromatic field is not a steady state. The resonance fluorescence spectrum of a two-level atom driven by a bichromatic field has only recently been experimentally investigated.<sup>55</sup> The theoretical expression for the form of the spectrum is still not completely agreed on.<sup>56</sup> In addition, as we shall see, the equations of motion for a 100% AM field within the rotating-wave approximation are identical to the equations of motion for a monochromatic field without making the rotating-wave approximation. We assume the bichromatic field can be written as

$$E(t) = 2\mathcal{E}_1 [\cos((\omega + \delta\omega)t) + \cos((\omega - \delta\omega)t)] . \quad (2.5)$$

We assume the amplitude of each component is  $2\mathcal{E}_1$ . We have made an arbitrary choice of phase so there is no quadrature component of the field. A simple trigonometric relationship allows us to write Eqn. (2.5) as

$$E(t) = 4\mathcal{E}_1 \cos \delta\omega t \cos \omega t . \quad (2.6)$$

Inserting this field into Eqn. (2.2), we see that  $\Omega'(t) = 2\Omega_1 \cos \delta\omega t$  and  $\Omega''(t) = 0$ , where we have defined the frequency  $\Omega_1 = (2d/\hbar)\mathcal{E}_1$ . These expressions allow

us to rewrite Eqn. (2.2) as

$$\frac{d}{dt} \begin{bmatrix} u \\ v \\ w \end{bmatrix} = \begin{bmatrix} -1/T_2 & -\Delta & 0 \\ \Delta & -1/T_2 & 2\Omega_1 \cos \delta\omega t \\ 0 & -2\Omega_1 \cos \delta\omega t & -1/T_1 \end{bmatrix} \begin{bmatrix} u \\ v \\ w \end{bmatrix} + \begin{bmatrix} 0 \\ 0 \\ w_{eq}/T_1 \end{bmatrix}. \quad (2.7)$$

At this point it is interesting to compare these equations with the equations describing a two-level atom interacting with a monochromatic field without making the rotating-wave approximation<sup>53</sup>

$$\frac{d}{dt} \begin{bmatrix} s_1 \\ s_2 \\ w \end{bmatrix} = \begin{bmatrix} -1/T_2 & -\omega_0 & 0 \\ \omega_0 & -1/T_2 & \frac{2d\mathcal{E}}{\hbar} \cos \omega t \\ 0 & -\frac{2d\mathcal{E}}{\hbar} \cos \omega t & -1/T_1 \end{bmatrix} \begin{bmatrix} s_1 \\ s_2 \\ w \end{bmatrix} + \begin{bmatrix} 0 \\ 0 \\ w_{eq}/T_1 \end{bmatrix}. \quad (2.8)$$

The variables  $s_1$  and  $s_2$  are the rapidly oscillating dipole moment quadratures. The detuning  $\Delta$  in Eqn. (2.7) corresponds to the two-level atom's transition frequency  $\omega_0$  in Eqn. (2.8) and the modulation frequency  $\delta\omega$  in Eqn. (2.7) corresponds to the frequency of the driving field  $\omega$  in Eqn. (2.8). The correction to the rotating-wave approximation on the atomic energy is called the Bloch-Siegert shift. The correspondence between a two-level atom being driven by a monochromatic field without making the rotating-wave approximation and a two-level atom being driven by a bichromatic field under the rotating-wave approximation allows one to study the Bloch-Siegert shifts in a much simpler context. This point is discussed by W. Ruyten<sup>57</sup>.

### 3. Stationary State Response

The 3x3-matrix in Eqn. (2.7) is periodic in time. Floquet's theorem<sup>58</sup> tells us that the stationary state solution to such a problem can be expanded as a Fourier series in terms of the fundamental frequency of the matrix. In other words the stationary state solution can be written as

$$\begin{bmatrix} u \\ v \\ w \end{bmatrix} = \sum_{n=-\infty}^{\infty} \begin{bmatrix} u_n \\ v_n \\ w_n \end{bmatrix} \exp(in\delta\omega t). \quad (2.9)$$

Substituting this solution into Eqn. (2.7) and equating terms of equal time dependence we obtain a set of recurrence relations

$$(1 + in\delta\omega T_2)u_n = -\Delta T_2 v_n, \quad (2.10a)$$

$$(1 + in\delta\omega T_2)v_n = \Delta T_2 u_n + \Omega_1 T_2 (w_{n+1} + w_{n-1}), \quad (2.10b)$$

$$(1 + in\delta\omega T_1)w_n = -\Omega_1 T_1 (v_{n+1} + v_{n-1}) + \delta_{n,0} w_{eq}. \quad (2.10c)$$

These equations give the relationships between the Fourier components of the atomic variables in the stationary state. To make the analysis more straightforward, we eliminate the Fourier components describing the polarization to obtain an equation describing the Fourier components of the inversion alone. We use Eqn. (2.10a) to eliminate  $u_n$ . Equation (2.10b) then becomes

$$((1 + in\delta\omega T_2)^2 + (\Delta T_2)^2)v_n = \Omega_1 T_2 (1 + in\delta\omega T_2)(w_{n+1} + w_{n-1}). \quad (2.11)$$

We then use Eqn. (2.11) to eliminate  $v_n$  so that the equation for the harmonic amplitudes of the inversion becomes

$$\frac{1}{2}I_1 A_{n-1} w_{n-2} + B_n w_n + \frac{1}{2}I_1 A_{n+1} w_{n+2} = w_{eq} \delta_{n,0}, \quad (2.12)$$

where

$$A_n = \frac{1 + in\delta\omega T_2}{(1 + in\delta\omega T_2)^2 + (\Delta T_2)^2}, \quad (2.13a)$$

$$B_n = 1 + in\delta\omega T_1 + I_1 (A_{n-1} + A_{n+1}), \quad (2.13b)$$

and

$$I_1 = 2\Omega_1^2 T_1 T_2. \quad (2.13c)$$

$I_1$  is the dimensionless time-averaged intensity in units of the two-level atom's saturation intensity. Equation (2.12) can be thought of as an infinite-dimensional tridiagonal matrix equation. The main diagonal is  $B_n$  and the lower and upper diagonals are  $\frac{1}{2}I_1 A_{n\pm 1}$ . The tridiagonal matrix multiplies the vector whose elements are  $w_n$ . The vector on the right hand side of the equation contains all zeros except for the  $n = 0$  position which is equal to  $w_{eq}$ .

For  $n \neq 0$ , the recurrence relation for the ratio,  $r_n \equiv w_n/w_{n-2}$  is

$$r_n = \frac{-\frac{1}{2}A_{n-1} I_1}{B_n + \frac{1}{2}A_{n+1} I_1 r_{n+2}}. \quad (2.14)$$

Using Eqn. (2.14) with  $n \rightarrow n+2$ , we can obtain an expression for  $r_{n+2}$  in terms of  $r_{n+4}$ . We substitute this expression into Eqn. (2.14) and obtain

$$r_n = \frac{-\frac{1}{2}A_{n-1} I_1}{B_n - \frac{(\frac{1}{2}A_{n+1} I_1)^2}{B_{n+2} + \frac{1}{2}A_{n+3} I_1 r_{n+4}}}. \quad (2.15)$$

Applying this procedure repeatedly leads to the limiting expression

$$\begin{aligned} r_n &= \frac{-\frac{1}{2}A_{n-1} I_1}{B_n - \frac{(\frac{1}{2}A_{n+1} I_1)^2}{B_{n+2} - \frac{(\frac{1}{2}A_{n+3} I_1)^2}{B_{n+4} - \frac{(\frac{1}{2}A_{n+5} I_1)^2}{B_{n+6} - \dots}}}} \\ &= C_n, \end{aligned} \quad (2.16)$$

where  $C_n$  is a continued fraction. This expression can be numerically evaluated on the computer by truncating the fraction to a finite number of divisions. We test the expression for convergence by increasing the number of divisions. When the results are not significantly different, the continued fraction has converged. Equation (2.16) gives the relationship between  $w_n$  and  $w_{n-2}$  for  $n \neq 0$ . For



$n = 2$  it yields the relation between  $w_2$  and  $w_0$

$$w_2 = \frac{-A_1 I_1}{B_2 - \frac{(\frac{1}{2}A_3 I_1)^2}{B_4 - \frac{(\frac{1}{2}A_5 I_1)^2}{B_6 - \frac{(\frac{1}{2}A_7 I_1)^2}{B_8 - \dots}}}} w_0$$

$$= C_2 w_0. \quad (2.17)$$

Using Eqn. (2.17) in Eqn. (2.12) with  $n = 0$ , we obtain an expression for  $w_0$

$$w_0[\frac{1}{2}A_{-1}I_1C_2^* + \frac{1}{2}A_1I_1C_2 + B_0] = w_{eq}, \quad (2.18)$$

or

$$w_0 = \frac{w_{eq}}{B_0 + \Re\{A_1 I_1 C_2\}}, \quad (2.19)$$

where  $\Re\{\cdot\}$  represents the real part of the complex argument. We have also used the fact that  $w$  is a real variable and therefore its Fourier transform is Hermitian (i.e.,  $w_n = w_{-n}^*$ , where the asterisk denotes the complex conjugate).

#### 4. Analysis and Results

Some variables of interest are the time-averaged component of the inversion  $w_0$ , the fundamental-harmonic component of the inversion  $w_2$ , and the gain of the bichromatic field. In Fig. (2.1) we plot  $w_0$  as a function of modulation frequency  $\delta\omega$  for a series of dimensionless field intensities  $I_1$  for the case of  $T_1 = 10T_2$ , which corresponds to a collisionally dephased medium.

We see that as  $I_1 \rightarrow 0$  the time-averaged inversion displays a Lorentzian response in modulation frequency of width  $1/T_2$ . As the dimensionless intensity  $I_1$  is increased, the Lorentzian-shaped response develops a hole of width  $\sim 1/T_1$ . The hole is related to the homogeneous hole burning observed in ruby, alexandrite, and fluorescein-doped boric-acid glass. For the case of  $T_1 = T_2/2$ , which

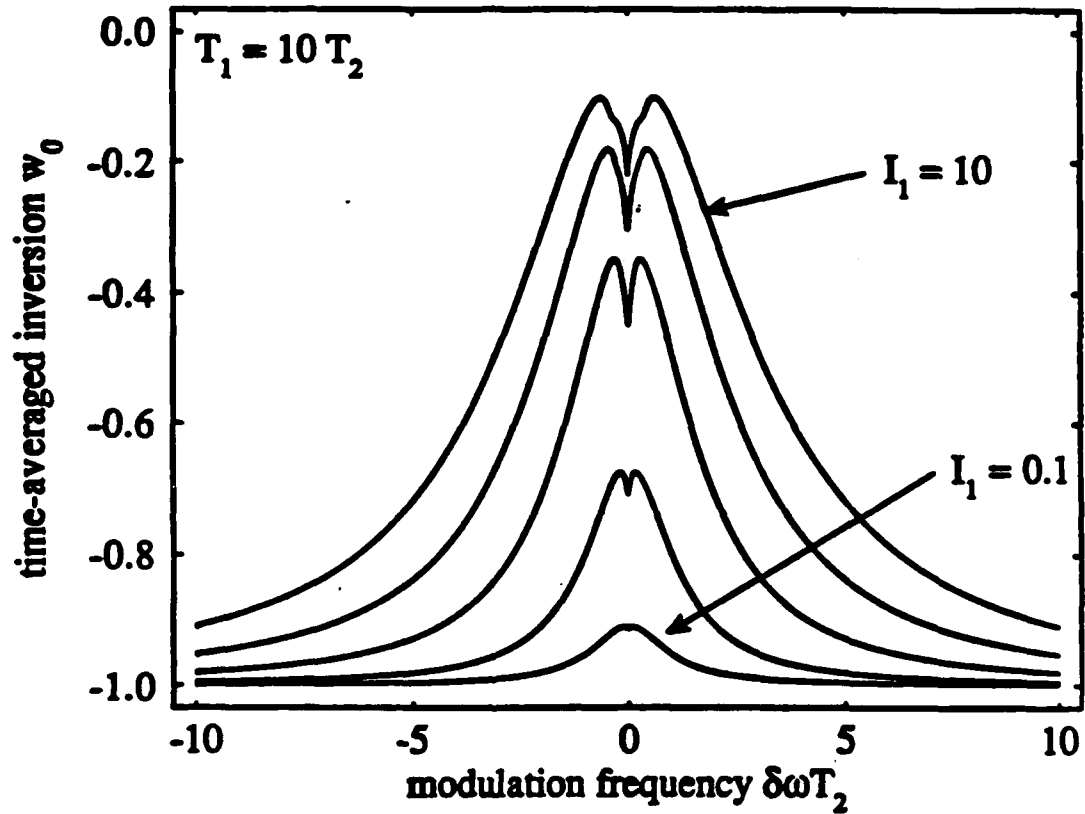


**Fig. 2.1** Time-averaged inversion of a collisionally broadened medium as a function of modulation frequency for a series of bichromatic field intensities. The time-averaged inversion,  $w_0$  is plotted as a function of modulation frequency for  $I_1 = 0.1, 0.5, 1, 2, 10$ . The atomic medium is collisionally broadened with  $T_1 = 10T_2$ .

corresponds to a medium whose transition is radiatively broadened, the hole is not present, as can be seen in Fig. (2.2).

On increasing the intensity further ( $\Omega_1 T_2 \approx 1$ ), structure begins to develop within the hole. It has the form of a series of subharmonic resonances. The time-averaged inversion is plotted as a function of modulation frequency in Figs. (2.3a-c).

This figure illustrates that the subharmonic structure is independent of the damping mechanism of the polarization. The peaks of the curves are plotted as a function of Rabi frequency and modulation frequency in Fig. (2.4).

The positions of the peaks are linearly related to the electric field amplitude. The slopes of the various lines indicate the resonances are nearly the subharmonics of the main resonance.

The inversion oscillates at a frequency called the *Rabi frequency*. For a monochromatic field, this frequency is directly proportional to the field amplitude. For a time-dependent field amplitude, the relationship is more complicated. For the case of 100% AM fields, the Rabi frequency is still proportional to the field amplitude. The main resonance in the time-averaged inversion occurs when the Rabi frequency is equal to the modulation frequency. The atom flips between the excited state and the ground state and back to the excited state in one modulation period. The first subharmonic resonance occurs when the Rabi frequency is approximately twice the modulation frequency. That is, the atom flips between the excited state and the ground state and back to the excited state twice in one modulation period. The other subharmonic resonances are similarly interpreted.

Another way to analyze these resonances is to keep the modulation fre-

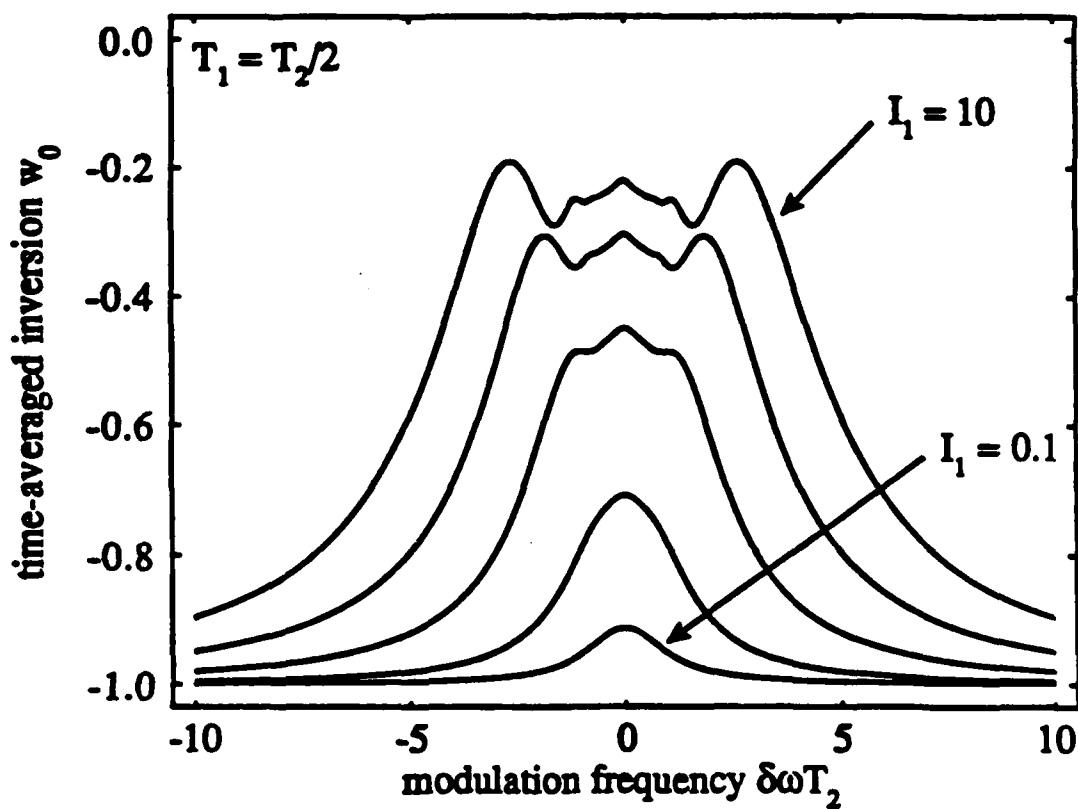


Fig. 2.2 Time-averaged inversion of a radiatively broadened medium as a function of modulation frequency for a series of bichromatic field intensities. The time-averaged inversion,  $w_0$  is plotted as a function of modulation frequency for  $I_1 = 0.1, 0.5, 1, 2, 10$ . The atomic medium is radiatively broadened with  $T_1 = \frac{1}{2}T_2$ .

quency constant and vary the dimensionless intensity. In Fig. (2.5), we plot the time-averaged inversion as a function of the amplitude of the 100% AM field for a fixed modulation frequency. For comparison we also show two additional plots: the inversion of an atom driven by a monochromatic field with the same time-averaged intensity on resonance and detuned by the modulation frequency. We see that the fluorescence induced by the 100% AM field never exceeds that induced by an on-resonance monochromatic field of equal intensity. For higher field amplitudes, the fluorescence induced by the 100% AM field is less than that induced by the detuned monochromatic field of equal intensity. The results of these numerical calculations have been experimentally verified by Chakmakjian *et al.*,<sup>59</sup> using an optically-pumped sodium atomic beam and a stabilized dye laser.

The gain of the bichromatic field can be written as the time-averaged product of the electric field and the time rate of change of the polarization.

$$\begin{aligned} E\dot{P} &= 4\mathcal{E}_1 \cos \delta\omega t \cos \omega t \frac{d}{dt} \left[ \Re \left\{ \frac{(u + iv)}{2} \exp(i\omega t) \right\} \right], \\ &\approx 4\mathcal{E}_1 \cos \delta\omega t \cos \omega t \Re \left\{ \frac{i\omega(u + iv)}{2} \exp(i\omega t) \right\}. \end{aligned} \quad (2.20)$$

Here we have neglected the time derivatives of the  $u$  and  $v$  since they are slowly-varying amplitudes (i.e.,  $|\dot{u}| \ll \omega|u|$  and  $|\dot{v}| \ll \omega|v|$ ). We expand the expression for the real part in Eqn. (2.20) to obtain

$$E\dot{P} = -2\mathcal{E}_1\omega(v \cos \delta\omega t \cos^2 \omega t + u \cos \delta\omega t \cos \omega t \sin \omega t). \quad (2.21)$$

After an optical period, the time average reduces to

$$E\dot{P} \approx -\mathcal{E}_1\omega(v \cos \delta\omega t),$$

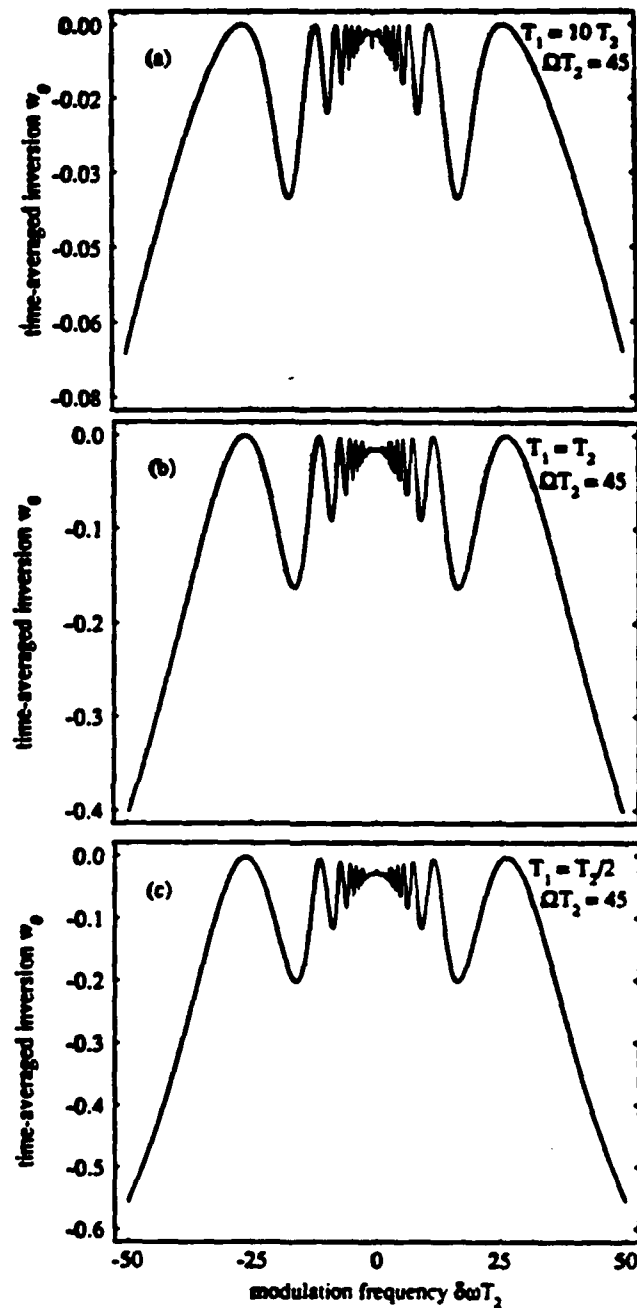


Fig. 2.3 Time-averaged inversion as a function of modulation frequency for large bichromatic field amplitude. The time-averaged inversion,  $w_0$  is plotted as a function of modulation frequency for a strong-field amplitude,  $\Omega_1 T_2 = 45$ . The figure demonstrates that the resonance structure of the time-averaged inversion is independent of the atom's damping mechanism. In (a)  $T_1 = 10T_2$ , in (b)  $T_1 = T_2$ , and in (c)  $T_1 = \frac{1}{2}T_2$ .

$$\begin{aligned}
&= -\frac{1}{2}\mathcal{E}_1\omega \sum_{n=-\infty}^{\infty} v_n(e^{i\delta\omega t} + e^{-i\delta\omega t})e^{in\delta\omega t}, \\
&= -\frac{1}{2}\mathcal{E}_1\omega(v_{-1} + v_1), \\
&= -\mathcal{E}_1\omega\Re\{v_1\},
\end{aligned} \tag{2.22}$$

where the only term surviving the time average is the first harmonic component of the polarization  $v_1$ .

From Eqn. (2.10c) with  $n = 0$ , we see there is a relation between the absorption of the bichromatic field and the time-averaged inversion.

$$w_{eq} - w_0 = 2\Omega_1 T_1 \Re\{v_1\}. \tag{2.23}$$

Therefore the absorption displays the same subharmonic structure in modulation frequency as the time-averaged inversion.

The last quantity we examine is  $w_2$ , the harmonic component of the inversion oscillating at the beat frequency,  $2\delta\omega$ , between the two field components. We use Eqn. (2.17) to calculate  $w_2$  as a function of modulation frequency. The real part of  $w_2$  represents the component of the inversion oscillating at  $2\delta\omega$  in-phase with the driving field. The imaginary part of  $w_2$  represents the component of the inversion oscillating at  $2\delta\omega$  in-quadrature to the driving field. Figure (2.6a-b) show these two quantities and the magnitude of  $w_2$  as a function of modulation frequency for various values of the time-averaged intensity,  $I_1$ . One of the interesting features of this quantity is that the structure of  $w_2$  versus modulation frequency or versus intensity survives a Doppler average over atomic detunings. This is pointed out by W. Ruyten<sup>57</sup> and is attributed to the fact that  $w_2$  plotted against Rabi frequency,  $\Omega_1$  and modulation frequency  $\delta\omega$  has two sets of zero crossings which he calls a doubly branched resonance structure.

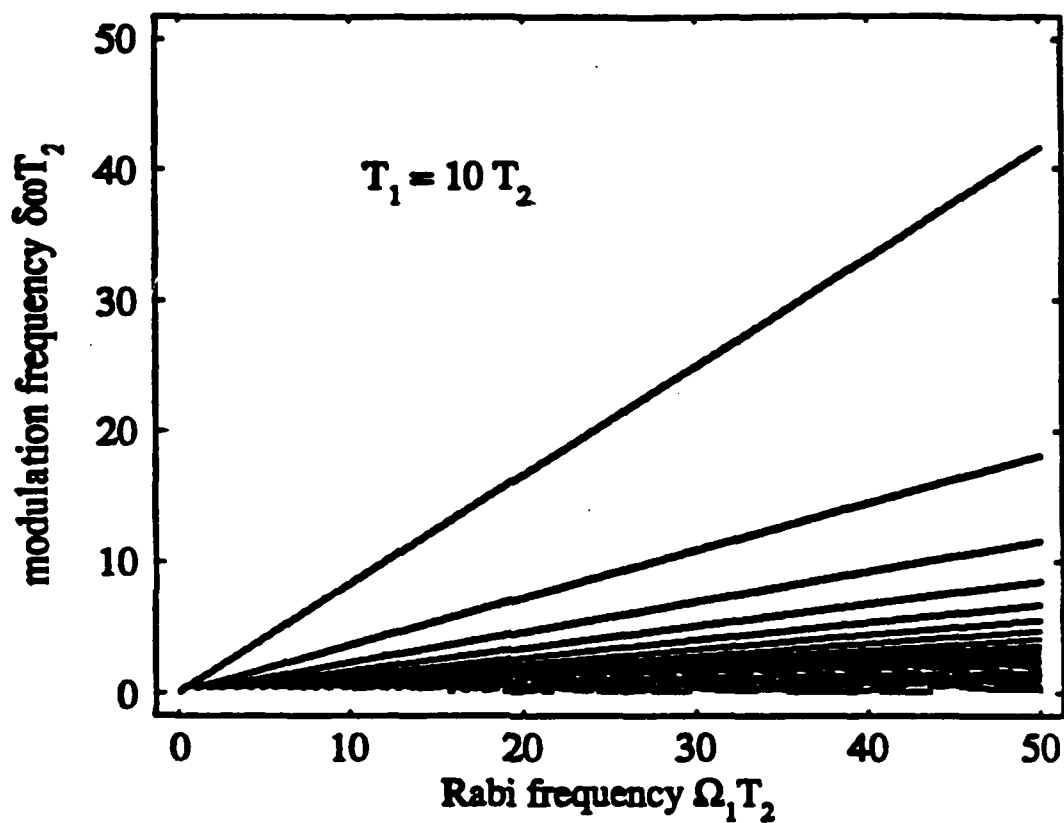


Fig. 2.4 Peak positions of the time-averaged inversion as a function of modulation frequency and bichromatic field amplitude. The peak positions of the time-averaged inversion are plotted as a function of modulation frequency and bichromatic field amplitude. The figure demonstrates that the position of the resonance peaks depends linearly on the field strength of the bichromatic field.



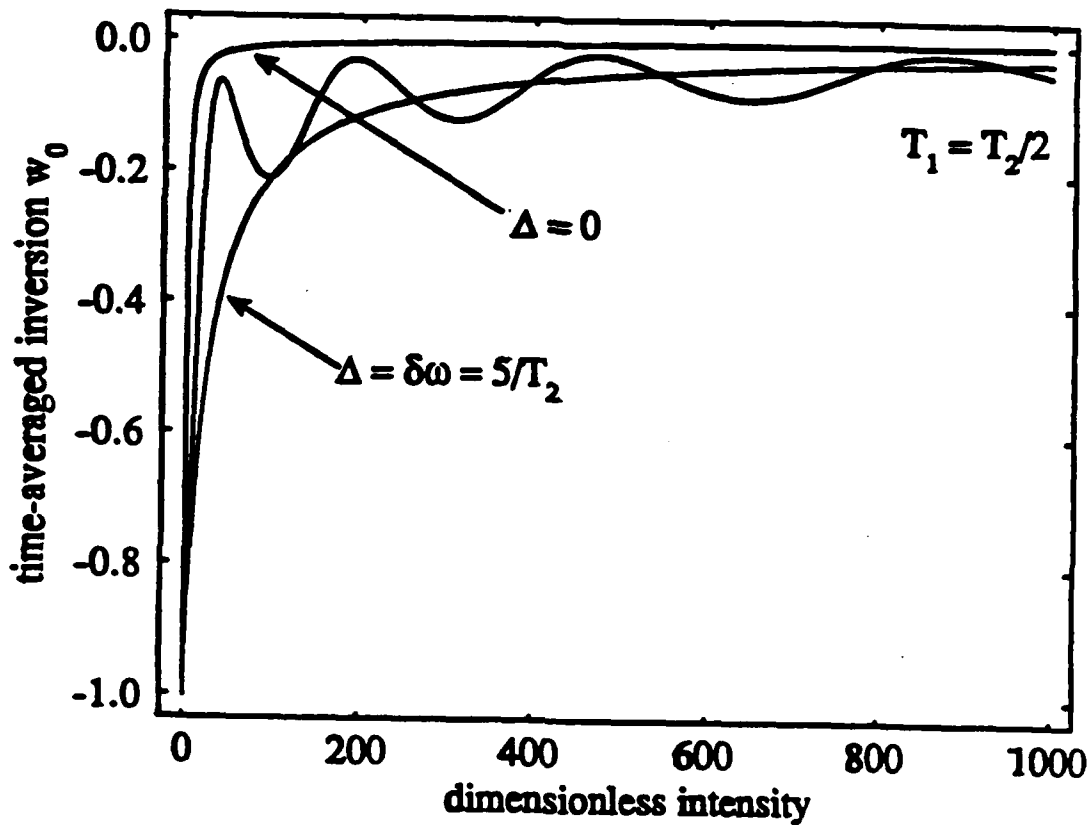


Fig. 2.5 Time-averaged inversion as a function of bichromatic field amplitude for a fixed modulation frequency. The time-averaged inversion is plotted as a function of bichromatic field strength for a fixed modulation frequency,  $\delta\omega T_2 = 5$ . The figure also contains the time-averaged inversion produced by an on-resonance monochromatic field with the same time averaged intensity as the bichromatic field and the time-averaged inversion produced by a monochromatic field of the same time-averaged intensity detuned by the modulation frequency.

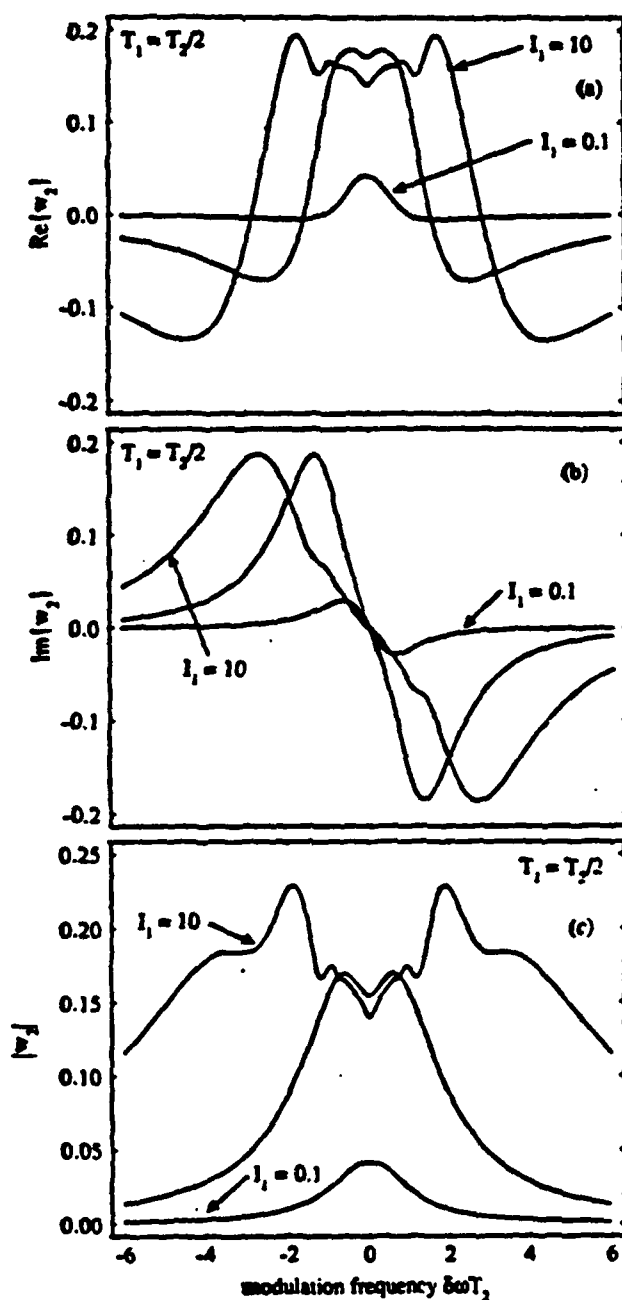


Fig. 2.6 Second harmonic component of the inversion as a function of modulation frequency for a series of bichromatic field intensities. The component of the inversion oscillating at twice the modulation frequency is plotted as a function of modulation frequency. The intensity  $I_1 \approx 0.1, 1, 10$  and  $T_1 = \frac{1}{2}T_2$ . (a) The real part of  $w_2$ , (b) the imaginary part of  $w_2$ , and (c) the magnitude of  $w_2$ .

## 5. Subharmonic Probe Field

Now that we have calculated the gain of the bichromatic field, we will analyze its stability to the growth of a subharmonic probe field. The period doubling sequence is especially interesting since it has been observed in many nonlinear systems enroute to chaos. We will consider the possibility of a period doubling instability in the two-level atom being driven by a strong bichromatic field. Period doubling can be thought of as the generation of the  $\frac{1}{2}$ -subharmonic. We will calculate the gain of a  $\frac{1}{2}$ -subharmonic probe field in the presence of the strong bichromatic field. For each strong-field modulation frequency there are two independent subharmonic fields. When the bichromatic field is symmetric about resonance, the two independent subharmonic fields are in-phase and in-quadrature to the strong bichromatic field. The spectrum of this on-resonance field is shown in Fig. (2.7).

We can write this on-resonance field as

$$E(t) = 4 [\mathcal{E}_1 \cos \delta\omega t + \delta\mathcal{E}' \cos(\frac{1}{2}\delta\omega t + \phi')] \cos \omega t - 4\delta\mathcal{E}'' \sin(\frac{1}{2}\delta\omega t + \phi'') \sin \omega t. \quad (2.24)$$

The amplitude of the probe field in-phase to the rotating frame is  $\delta\mathcal{E}'(t)$ ,  $\delta\mathcal{E}''(t)$  is in-quadrature. The phases of the modulations,  $\phi'$  and  $\phi''$ , are with respect to the modulation of the strong bichromatic field. It is easily shown that the in-quadrature probe-field gain is independent of the phase of the modulations. We include the phase in the analysis for completeness. The Bloch equations for this field are

$$\frac{d}{dt} \begin{bmatrix} u \\ v \\ w \end{bmatrix} = \begin{bmatrix} -1/T_2 & 0 & -\Omega''(t) \\ 0 & -1/T_2 & \Omega'(t) \\ \Omega''(t) & -\Omega'(t) & -1/T_1 \end{bmatrix} \begin{bmatrix} u \\ v \\ w \end{bmatrix} + \begin{bmatrix} 0 \\ 0 \\ w_{eq}/T_1 \end{bmatrix}, \quad (2.25)$$

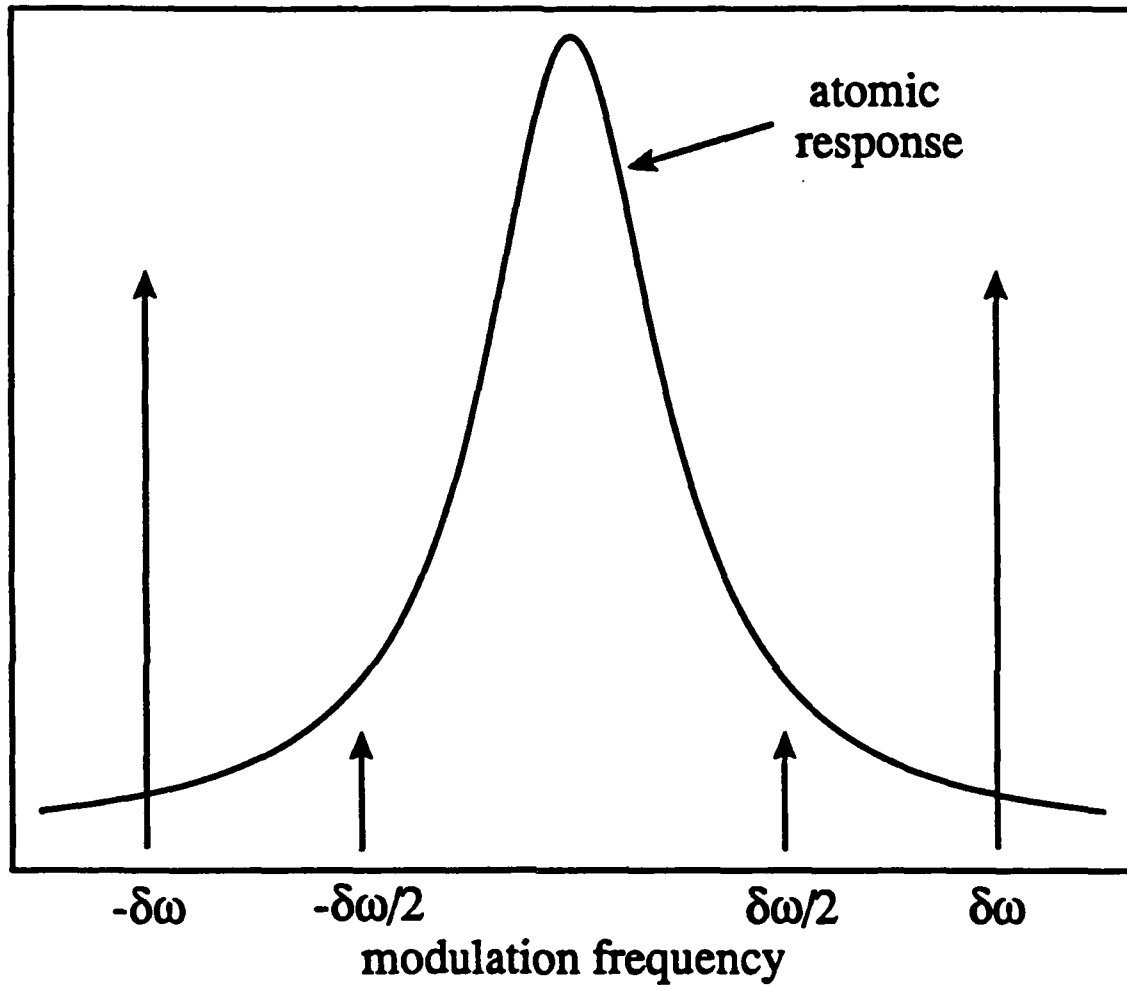


**Fig. 2.7** Applied field spectrum for the  $\frac{1}{2}$ -subharmonic probe field and strong bichromatic field. The Lorentzian lineshape represents the atomic response. The frequency components at  $\pm\delta\omega$  represent the two-frequency strong field. The two frequency components at  $\pm\delta\omega/2$  represent the two-frequency probe field. The field components are assumed to be symmetrically placed about the atomic resonance.

where  $\Omega'(t) = 2(\Omega_1 \cos \delta\omega t + \delta\Omega' \cos(\frac{1}{2}\delta\omega t + \phi'))$  and  $\Omega''(t) = 2\delta\Omega'' \sin(\frac{1}{2}\delta\omega t + \phi'')$ . Since the 3x3-matrix in Eqn. (2.25) is periodic in time, we can employ Floquet's theorem and expand the atomic variables in a Fourier series. The stationary state solution for the atomic variables is written as

$$\begin{bmatrix} u \\ v \\ w \end{bmatrix} = \sum_{n=-\infty}^{\infty} \begin{bmatrix} u_n \\ v_n \\ w_n \end{bmatrix} \exp(\frac{1}{2}in\delta\omega t). \quad (2.26)$$

Substituting this expression into Eqn. (2.25) and equating terms of equal time dependence generates the following recurrence relations

$$(1 + \frac{1}{2}in\delta\omega T_2)u_n = (\delta\bar{\Omega}''w_{n-1} + \delta\bar{\Omega}''^*w_{n+1})T_2, \quad (2.27a)$$

$$(1 + \frac{1}{2}in\delta\omega T_2)v_n = (\Omega_1(w_{n-2} + w_{n+2}) + \delta\bar{\Omega}'w_{n-1} + \delta\bar{\Omega}'^*w_{n+1})T_2, \quad (2.27b)$$

$$(1 + \frac{1}{2}in\delta\omega T_1)w_n = w_{eq}\delta_{n,0} - [\Omega_1(v_{n-2} + v_{n+2}) + \delta\bar{\Omega}''u_{n-1} + \delta\bar{\Omega}''^*u_{n+1} + \delta\bar{\Omega}'v_{n-1} + \delta\bar{\Omega}'^*v_{n+1}]T_1 \quad (2.27c)$$

where

$$\delta\bar{\Omega}' = (2d/\hbar)\mathcal{E}' \exp(i\phi'), \quad (2.28a)$$

$$\delta\bar{\Omega}'' = i(2d/\hbar)\mathcal{E}'' \exp(i\phi''), \quad (2.28b)$$

and the asterisk denotes the complex conjugate. Again to simplify the analysis, we eliminate the variables of the polarization to obtain a relationship for the harmonic components of the inversion alone. Using Eqn. (2.27a), we solve for the n-th Fourier component of the slowly varying in-phase part of the dipole moment

$$u_n = L_n(\delta\bar{\Omega}''w_{n-1} + \delta\bar{\Omega}''^*w_{n+1})T_2, \quad (2.29)$$

where  $L_n$  is the complex Lorentzian function,

$$L_n = \frac{1}{1 + in\delta\omega T_2}. \quad (2.30)$$

We use Eqn. (2.27b) to obtain an expression for the  $n$ -th Fourier component of the slowly varying in-quadrature part of the dipole moment

$$v_n = L_n[\Omega_1(w_{n-2} + w_{n-2}) + \delta\bar{\Omega}'w_{n-1} + \delta\bar{\Omega}''w_{n+1}]T_2. \quad (2.31)$$

We now substitute Eqns. (2.29) and (2.31) into Eqn.(2.27c) to obtain a recurrence relation for the inversion's harmonic components alone.

$$\begin{aligned} a_n w_{n-4} + b_n w_{n-3} + c_n w_{n-2} + d_n w_{n-1} + e_n w_n \\ + i_n w_{n+4} + h_n w_{n+3} + g_n w_{n+2} + f_n w_{n+1} = \delta_{n,0}, \end{aligned} \quad (2.32)$$

where the coefficients of the recurrence relation are functions of the field amplitudes, modulation frequency, and relaxation times

$$a_n = L_{n-2}\Omega_1^2 T_1 T_2, \quad (2.33a)$$

$$b_n = (L_{n-2} + L_{n-1})\Omega_1 \delta\bar{\Omega}' T_1 T_2, \quad (2.33b)$$

$$c_n = L_{n-1}(\delta\bar{\Omega}'^2 + \delta\bar{\Omega}''^2) T_1 T_2, \quad (2.33c)$$

$$d_n = (L_{n-2} + L_{n+1})\Omega_1 \delta\bar{\Omega}'' T_1 T_2, \quad (2.33d)$$

$$\begin{aligned} e_n = 1 + in\delta\omega T_1 + \Omega_1^2 T_1 T_2 (L_{n-2} + L_{n+2}) \\ (|\delta\bar{\Omega}'|^2 T_1 T_2 + |\delta\bar{\Omega}''|^2 T_1 T_2)(L_{n-1} + L_{n+1}), \end{aligned} \quad (2.33e)$$

$$f_n = (L_{n-2} + L_{n-1})\Omega_1 \delta\bar{\Omega}' T_1 T_2, \quad (2.33f)$$

$$g_n = L_{n+1}[(\delta\bar{\Omega}'')^2 + (\delta\bar{\Omega}''')^2] T_1 T_2, \quad (2.33g)$$

$$h_n = (L_{n+2} + L_{n+1})\Omega_1 \delta\bar{\Omega}'' T_1 T_2, \quad (2.33h)$$

$$i_n = L_{n+2}\Omega_1^2 T_1 T_2. \quad (2.33i)$$

We simplify the analysis by defining the matrices

$$P_n = \begin{bmatrix} a_{4n-3} & b_{4n-3} & c_{4n-3} & d_{4n-3} \\ 0 & a_{4n-2} & b_{4n-2} & c_{4n-2} \\ 0 & 0 & a_{4n-1} & b_{4n-1} \\ 0 & 0 & 0 & a_{4n} \end{bmatrix}, \quad (2.34)$$

$$Q_n = \begin{bmatrix} e_{4n-3} & f_{4n-3} & g_{4n-3} & h_{4n-3} \\ d_{4n-2} & e_{4n-2} & f_{4n-2} & g_{4n-2} \\ c_{4n-1} & d_{4n-1} & e_{4n-1} & f_{4n-1} \\ b_{4n} & c_{4n} & d_{4n} & e_{4n} \end{bmatrix}, \quad (2.35)$$

$$R_n = \begin{bmatrix} i_{4n-3} & 0 & 0 & 0 \\ h_{4n-2} & i_{4n-2} & 0 & 0 \\ g_{4n-1} & h_{4n-1} & i_{4n-1} & 0 \\ f_{4n} & g_{4n} & h_{4n} & i_{4n} \end{bmatrix}, \quad (2.36)$$

$$W_n = \begin{bmatrix} w_{4n-3} \\ w_{4n-2} \\ w_{4n-1} \\ w_{4n} \end{bmatrix}, \quad (2.37)$$

and

$$D_n = \begin{bmatrix} 0 \\ 0 \\ 0 \\ \delta_{n,0} \end{bmatrix}. \quad (2.38)$$

The rows of each of the matrices are elements of the recurrence relation, Eqn. (2.32), shifted by four to make them independent of each other. We can now write a three-term matrix recurrence relation

$$P_n W_{n-1} + Q_n W_n + R_n W_{n+1} = w_{eq} D_n. \quad (2.39)$$

Any n-term recurrence relation can be reduced to a three-term matrix recurrence relation such as this one.<sup>60</sup> The solution to Eqn.(2.39) depends on the fact that the larger index variables eventually become insignificant. The larger harmonic components of  $w$  must become less significant if the Fourier series in Eqn. (2.26) are to converge and if the rotating-wave approximation is to remain valid. Therefore, we assume that the vectors of harmonic components of the

inversion  $W_n$  are negligible for  $n > N$ . With this assumption, the recurrence relation, Eqn. (2.39), for  $n = N$  can be written as

$$P_N W_{N-1} + Q_N W_N = 0, \quad (2.40)$$

since  $W_{N+1} \approx 0$ . This allows us to solve for  $W_N$  in terms of  $W_{N-1}$ . That is

$$W_N = -Q_N^{-1} P_N W_{N-1}. \quad (2.41)$$

For  $n=N-1$ , Eqn. (2.39) becomes

$$P_{N-1} W_{N-2} + Q_{N-1} W_{N-1} + R_{N-1} W_N = 0 \quad (2.42)$$

Using Eqn. (2.41), this becomes

$$P_{N-1} W_{N-2} + (Q_{N-1} - R_{N-1} Q_N^{-1} P_N) W_{N-1} = 0, \quad (2.43)$$

or

$$W_{N-1} = -(Q_{N-1} - R_{N-1} Q_N^{-1} P_N)^{-1} P_{N-1} W_{N-2}. \quad (2.44)$$

We can continue in such a manner, defining the larger index Fourier amplitudes in terms of the smaller index amplitudes, until we reach the relation for  $n=1$  when we have

$$W_1 = -[Q_1 - R_1(Q_2 - R_2(\cdots(Q_{N-1} - R_{N-1} Q_N^{-1} P_N)^{-1} P_{N-1})^{-1} \cdots)^{-1} P_2]^{-1} P_1 W_0, \quad (2.45)$$

or more simply

$$W_1 = M_+ W_0, \quad (2.46)$$



where  $M_+$  is the matrix continued fraction. We can obtain a similar expression using the fact that the negative Fourier components will be less significant for  $n < -N$ . For  $n = -N$  Eqn. (2.39) can be written as

$$Q_{-N}W_{-N} + R_{-N}W_{-N+1} = 0, \quad (2.47)$$

since  $W_{-N-1} \approx 0$ . This allows us to solve for  $W_{-N}$  in terms of  $W_{-N+1}$ . That is

$$W_{-N} = -Q_{-N}^{-1}R_{-N}W_{-N+1}. \quad (2.48)$$

We proceed as before until we reach the relation for  $n = -1$  where we obtain

$$W_{-1} = -[Q_{-1} - P_{-1}(Q_{-2} - P_{-2}(\cdots(Q_{-N+1} - P_{-N+1}Q_{-N}^{-1}R_{-N})^{-1}R_{-N+1})^{-1}\cdots)^{-1}R_{-2}]^{-1}R_{-1}W_0, \quad (2.49)$$

or more simply

$$W_{-1} = M_- W_0. \quad (2.50)$$

Strictly speaking, the matrices  $M_+$  and  $M_-$  are functions of  $N$ . However, we choose  $N$  sufficiently large so that  $M_+$  and  $M_-$  become independent of  $N$  to the desired accuracy of the calculation. We now return to Eqn. (2.39) with  $n = 0$  and use Eqns. (2.46) and (2.50) to obtain

$$[P_0M_- + Q_0 + R_0M_+]W_0 = w_{eq}D_0. \quad (2.51)$$

This matrix equation represents a set of four linear equations that can easily be evaluated on a computer. The results of this calculation are shown in Fig. (2.8).

We have plotted the gain of the  $\frac{1}{3}$ -subharmonic field as a function of the modulation frequency for various values of the strong-field intensity. In Fig. (2.9),

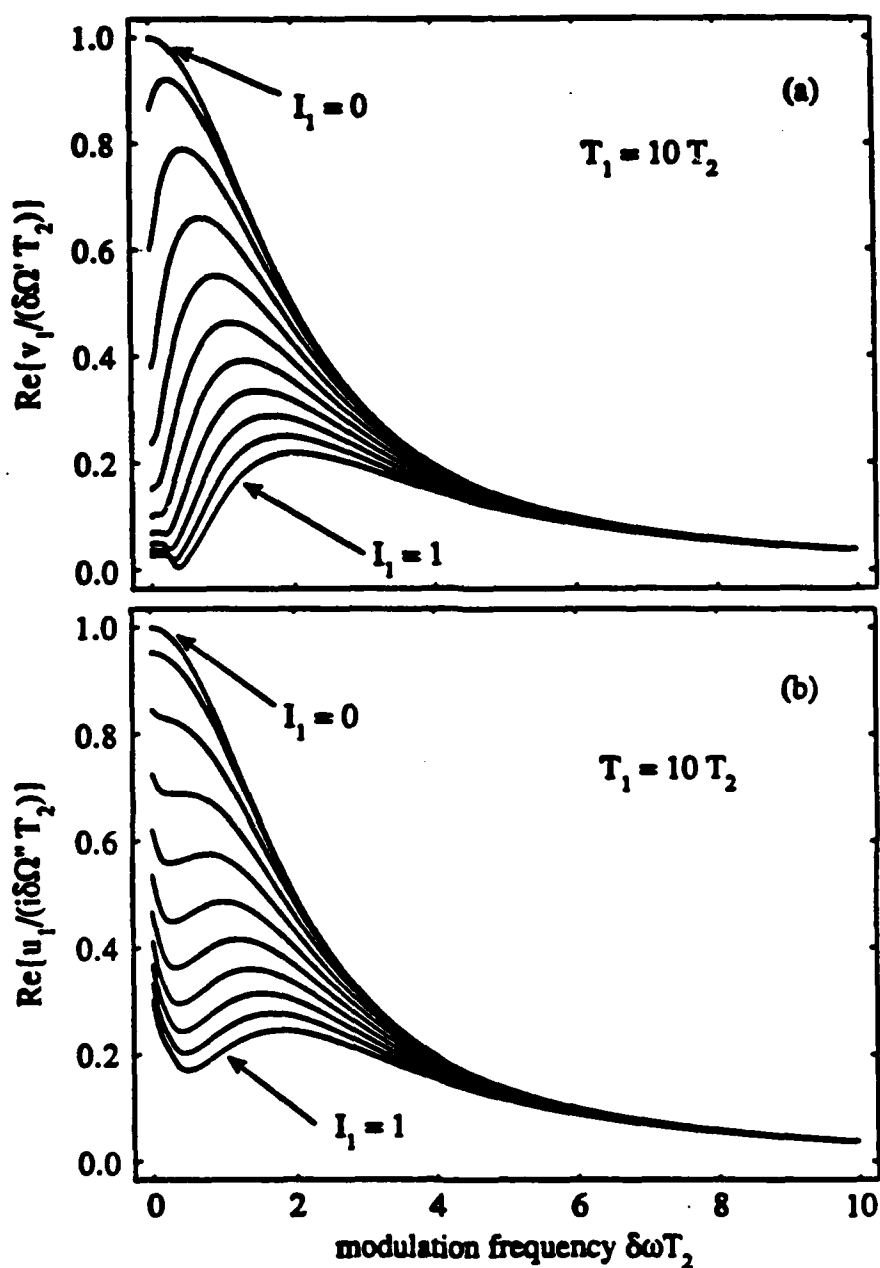


Fig. 2.8 Gain of the  $\frac{1}{2}$ -subharmonic probe field as a function of modulation frequency for a series of strong-field intensities. The gain of the  $\frac{1}{2}$ -subharmonic probe field is plotted as a function of modulation frequency for a series of strong-field amplitudes,  $I_1 = 0, 0.1, 0.2, 0.3, 0.4, 0.5, 0.6, 0.7, 0.8, 0.9, 1$ . The medium is modelled as collisionally broadened with  $T_1 = 10T_2$ . (a) gain of the in-phase component of the field (b) gain of the in-quadrature component of the field.

we plot the in-phase and in-quadrature  $\frac{1}{2}$ -subharmonic probe-field gain along with the strong-field gain for a strong-field amplitude  $\Omega_1 T_2 = 10$  and for a collisionally dephased medium with  $T_1 = 10T_2$ .

The probe field gain exceeds the strong-field gain everywhere except near the absolute maximum of the strong-field gain. If the strong bichromatic field is the field in a laser operating at the maximum gain, the  $\frac{1}{2}$ -subharmonic will not destabilize the bichromatic field. However, if there is a frequency-dependent loss that is larger for larger modulation frequencies, the strong bichromatic field will experience more losses at  $\delta\omega$  than the probe fields will experience at  $\frac{1}{2}\delta\omega$ . The point at which the instability occurs will depend on the severity of the frequency-dependent loss. These conclusions agree with the experiments of Hillman *et al.*,<sup>43</sup> and Stroud *et al.*<sup>44-45</sup> In the experiment of Hillman *et al.*,<sup>43</sup> a highly dispersive flint glass prism was used as a frequency selection element and the strong bichromatic field was observed to become unstable when the two components reached a separation of  $\sim 80 \text{ \AA}$ . Stroud *et al.*,<sup>44-45</sup> used a low-dispersion quartz glass prism and observed that the strong bichromatic field remained stable up to a separation of over  $340 \text{ \AA}$ .

Another subharmonic probe field that is interesting in the stability analysis of the bichromatic field is the  $\frac{1}{3}$ -subharmonic probe field. The beat notes generated by adjacent field components of the bichromatic field and its  $\frac{1}{3}$ -subharmonic are degenerate. This fact reduces the recurrence relation of the inversion to a 7-term recurrence relation. The 3-term matrix recurrence relation is then made up of  $3 \times 3$  matrices; Koch *et al.*,<sup>61</sup> discuss the details of this analysis. The conclusions from the  $\frac{1}{3}$ -subharmonic analysis are identical to the  $\frac{1}{2}$ -subharmonic case. That is, the strong field is stable to the growth of the subharmonic field except

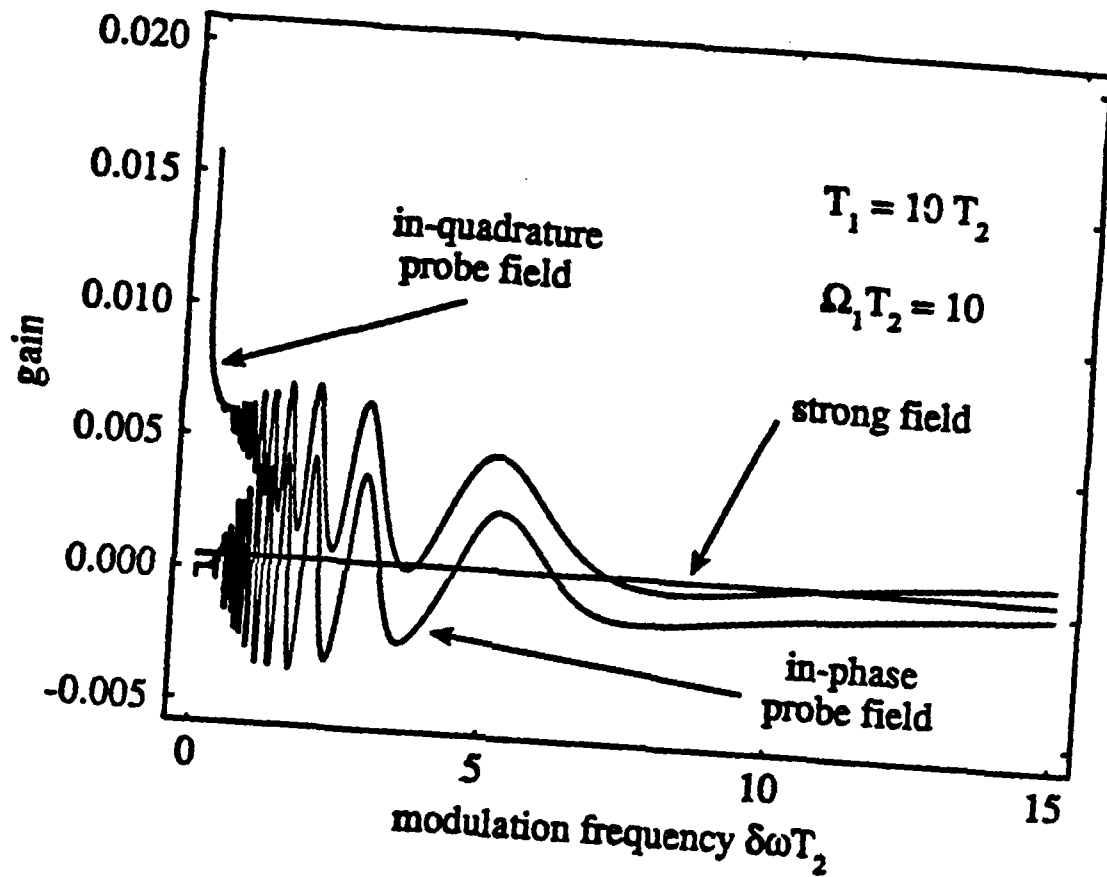


Fig. 2.9 Gain of the in-phase and in-quadrature  $\frac{1}{2}$ -subharmonic probe fields and the gain of the strong bichromatic field as a function of modulation frequency. The gain of the strong field and the two quadratures of the subharmonic probe field are plotted as a function of modulation frequency. The figure illustrates that at the modulation frequency of the global maximum of the strong-field gain — which on this scale appears rather flat — is greater than the gain of either subharmonic probe. The strong field is also stable oscillating at its first subharmonic.

when a frequency-dependent loss is present. The severity of the frequency-dependent loss determines the threshold for instability.

It would be very interesting to compare the gain of a 100% AM probe field of arbitrary modulation frequency with the gain of the strong bichromatic field. However, there are technical details that make this analysis difficult to perform. Namely, the nonlinear response of a two-level atom produces combination tones of the driving field components in the polarization and inversion of the atom; when the frequencies of the driving field are incommensurate, the medium can exhibit a broadband spectral response. The analytic description of such a problem becomes extremely difficult. If the frequencies of the driving field are commensurate, then Floquet's theorem can be employed and one could study the problem in a manner similar to those described in this chapter; however, if the ratio of strong-field modulation frequency to the probe-field modulation frequency is equal to the ratio of two large integers, then the dimension of the matrices in the analysis will also be large. This is related to the fact that an increasing number of frequencies must be taken into account as the modulation frequencies of the probe and the strong fields approach an incommensurate ratio.

## Chapter III

### MODULATION MIXING IN A DYE LASER

#### 1. Introduction

In this Chapter, we review an experiment investigating the dynamic behavior of a dye laser pumped by a modulated argon-ion laser. The study is relevant to lasers with time-dependent pump parameter, chaos and turbulence, nonlinear optics, and chaos in quantum systems.

The motivation for this work came, in part, from a paper by Pomeau *et al.*<sup>62</sup>, a numerical investigation of the response of a two-level atom driven by two fields. The authors' interests include the influence of incommensurate driving fields on quantum systems and the possibility for chaos in a purely quantum mechanical system. The authors find that when the two frequencies are commensurate (i.e. the ratio of the two frequencies is a rational number), the system exhibits a periodic response. In contrast, when the two frequencies are incommensurate (i.e. the ratio of the two frequencies is an irrational number), the system exhibits a more complicated response; the Fourier transform of the time evolution of the inversion is broadband and the wave function's time-

dependent autocorrelation function falls off rapidly. These results suggest that a conservative system driven at two incommensurate frequencies may behave chaotically. The results are somewhat dissatisfying since numerical calculations can only approximate true incommensurate ratios. In an attempt to examine better and better approximations to incommensurate ratios, Eidson and Fox<sup>63</sup> approximate incommensurate ratios by ratios of consecutive numbers of the Fibonacci sequence. The Fibonacci sequence is generated by the recurrence relation  $x_{n+2} = x_n + x_{n+1}$  for  $n \geq 0$  and the initial conditions  $x_0 = x_1 = 1$  (i.e., 1, 1, 2, 3, 5, 8, 13, ...). The ratios of consecutive numbers of the Fibonacci sequence approach the golden mean  $(\sqrt{5}-1)/2$ , the most incommensurate number. Approximating the incommensurate ratio of frequencies by the ratio of initial Fibonacci numbers, gives a spectrum of clearly resolved combination tones of the two frequencies. Approximating the incommensurate ratio of frequencies by the ratio of larger Fibonacci numbers, gives a more complicated spectrum where the time necessary to resolve the combination tones increases. In the limit of a truly incommensurate ratio, the field components can be arbitrarily close to one another and therefore cannot be resolved in a finite amount of time. The reason Pomeau et al.<sup>62</sup>, observed a broadband spectrum could be they simply did not resolve the spectrum's combination tones. They approximated the incommensurate ratio of frequencies by the ratio of integers, 1711/28657 and 4637/13313. The large prime denominators make the time necessary to resolve the combinations tones extremely long. Besides these numerical studies, numerical calculations by Badii and Meier<sup>64</sup> show that a double Poincaré section (recording the points where a four-dimensional trajectory intersects a plane) of the inversion's time series yields a smooth curve indicating that the motion, although quite complicated, is not chaotic, but quasiperiodic. This suggests that

a conservative system driven by two incommensurate frequencies is not chaotic. Additional calculations have been performed by Band et al.<sup>65</sup>, who analyze a nonlinear mixing crystal driven by two multimode lasers with different cavity mode spacings. When the cavity mode spacing frequencies are commensurate, they find the output of the nonlinear mixer is periodic. When the cavity mode spacing frequencies is incommensurate, the output of the nonlinear mixer shows broadband spectral features. They also claim that the output will be chaotic if the phases of the lasers wander independently. The authors use their results to suggest a more efficient scheme for frequency mixing. The experimentally important complication of dissipation in the dynamics of the system has not been addressed in these analyses. Many systems that do not exhibit chaos in a conservative framework, become chaotic when damping mechanisms are added to the dynamics.

In work concerning incommensurate frequencies in dissipative nonlinear systems, Hopf<sup>66</sup> considers the propagation of a quasiperiodic field, modulated in amplitude and phase, through an inhomogeneously broadened amplifier. He finds that embedding techniques classify the output of the amplifier as noise; although, arguments are made to suggest that chaos is not necessarily excluded. However, it is not clear whether the time series analyzed were long enough to resolve the combination tones generated in the field on propagating through the amplifier.

The interaction of multiple-frequency fields is also of interest in considering Landau's proposal<sup>67</sup> for a possible mechanism for the onset of turbulence. Landau proposed that, as a parameter of the system was varied, the spectrum of the system would successively develop incommensurate frequencies, along with combination tones of the existing frequencies, until the system's behavior



becomes quite complicated or turbulent. In contrast to this route to turbulence, Ruelle and Takens<sup>68</sup> and Newhouse *et al.*<sup>69</sup>, predict that multifrequency quasiperiodic motion is unstable to perturbative changes of the system. These perturbative changes in the system convert the quasiperiodic motion to chaotic motion. However, these destabilizing perturbations belong to a small subset of the possible perturbations of the system. A numerical study of three- and four-frequency quasiperiodic maps by Grebogi *et al.*<sup>70-72</sup>, shows that stable three- and four-frequency quasiperiodic orbits do exist. Three-frequency quasiperiodic orbits have been observed experimentally.<sup>73-74</sup> Unlike the work presented in this Chapter, these experimental three-frequency quasiperiodic orbits arose from three Hopf bifurcations in the dynamic response of the system as a parameter of the system was changed; in this experiment we externally drive the system at two or more frequencies.

The nonlinear response of a two-level atom to an applied field is responsible for the broadband spectra that were observed in references 62-66. Nonlinear behavior exists in almost every real system. The output power of a laser is a nonlinear function of the pump power near the threshold for lasing. Other nonlinear effects such as discontinuous intensity jumps, hysteresis, and the effects of critical slowing down, can be observed in the output power of lasers. The high-Q multimode ring dye laser used in previous experiments<sup>43-45</sup> has displayed all these effects. The nonlinear kink at the threshold for lasing, discontinuous intensity jumps, and hysteresis are seen in Fig. (3.1).

The plot shows the dye laser output power as a function of normalized pump power, as the pump power is swept sinusoidally at 2 kHz. The abscissa in Fig. (3.1) is pump power divided by threshold pump power. These nonlinearities provide the system with a mechanism for mixing the driving frequencies. The

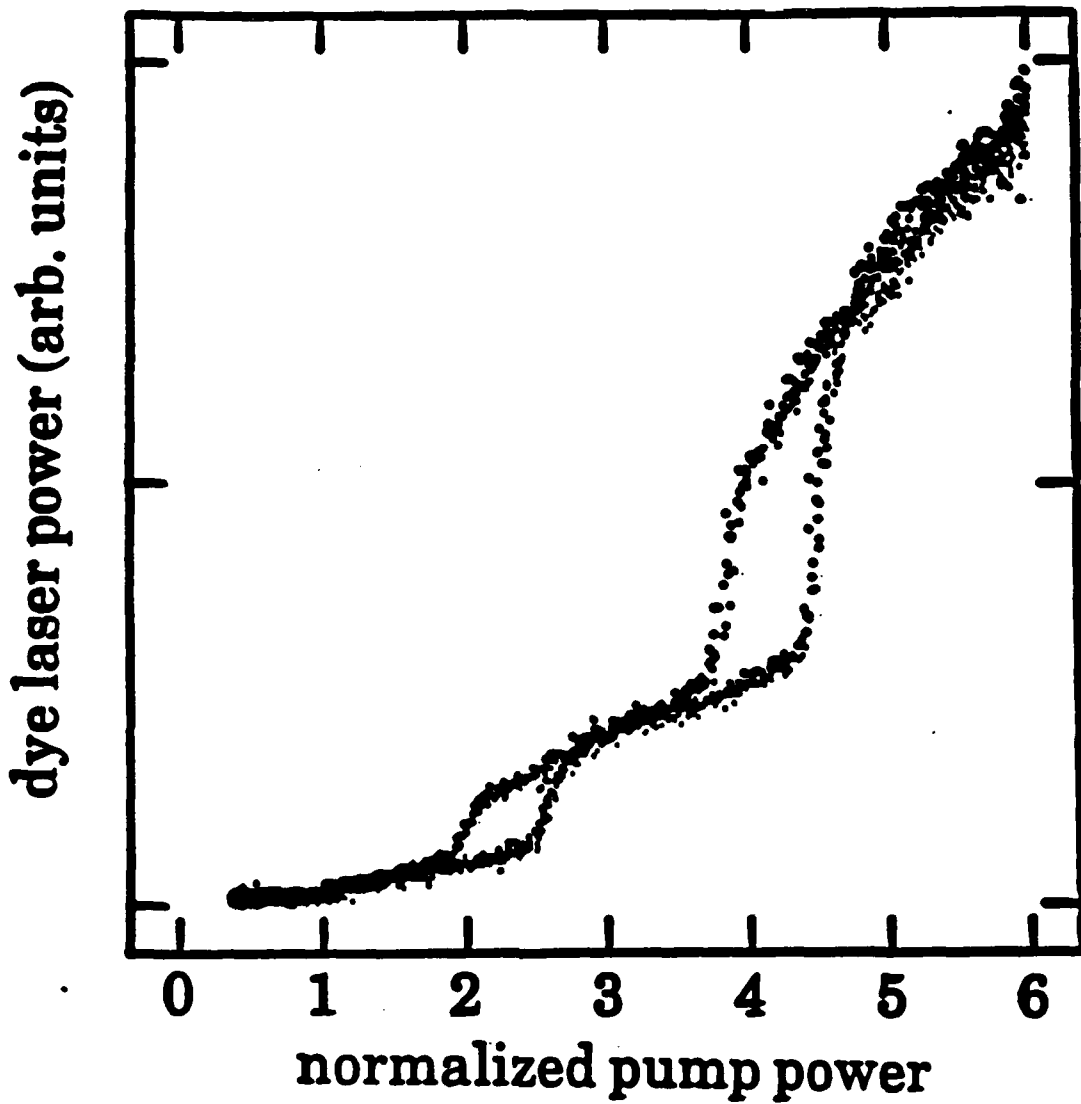


**Fig. 3.1** Dye laser output power versus normalized pump power for a high-Q multimode ring dye laser. The output of a high-Q multimode ring dye laser is measured as the pump laser is modulated at 1 kHz. The figure illustrates the nonlinear relationship that exists between the input pump intensity and the output dye laser intensity. The pump intensity is normalized to threshold.

possibility of generating new frequencies or a chaotic response are also possible.

Lasers are often used as pump sources for other lasers. The different modes of a multimode pump laser or the single modes of many individual pump lasers can beat together to form a modulation of the pump source. In this Chapter we study the effect the modulation has on the output of the laser being pumped. Specifically, we examine a multimode dye laser pumped by an argon-ion laser with adjustable modulation frequencies. The results of this experimental work are relevant not only to the study of nonlinear systems driven by multiple frequencies, but also give information about the behavior of a multimode dye laser with a time-dependent pump parameter.

## 2. Experimental Setup

The experimental setup is sketched in Fig. (3.2). A multimode argon-ion laser (Coherent Innova-20), operating at a single wavelength, 5145 Å, pumps a multimode dye laser. The longitudinal mode spacing of the argon-ion laser is approximately 80 MHz. The rms amplitude of 80 MHz modulation is 0.2% of the total intensity. The rms amplitude of the line frequency and its harmonics is less than 1% of the total intensity. We focus the beam of the argon-ion laser through a traveling-wave acousto-optic modulator (IntraAction Model:ADM-40). We recollimate the zeroth-order output of the modulator before focusing it on the dye jet of the dye laser. We found it necessary to focus and recollimate the argon-ion laser to preserve the TEM<sub>00</sub> beam, and to maximize the bandwidth from the modulator. The bandwidth of this modulation was approximately 4 MHz. The acousto-optic modulator is driven by a 40 MHz radio-frequency source. The sum of a series of oscillators (Wavetek Model:188) modulates the amplitude of the 40 MHz signal. The oscillators operate from 1 kHz to 400 kHz. The contrast ratio [ (maximum - minimum)/(maximum + minimum) ] of the total intensity of

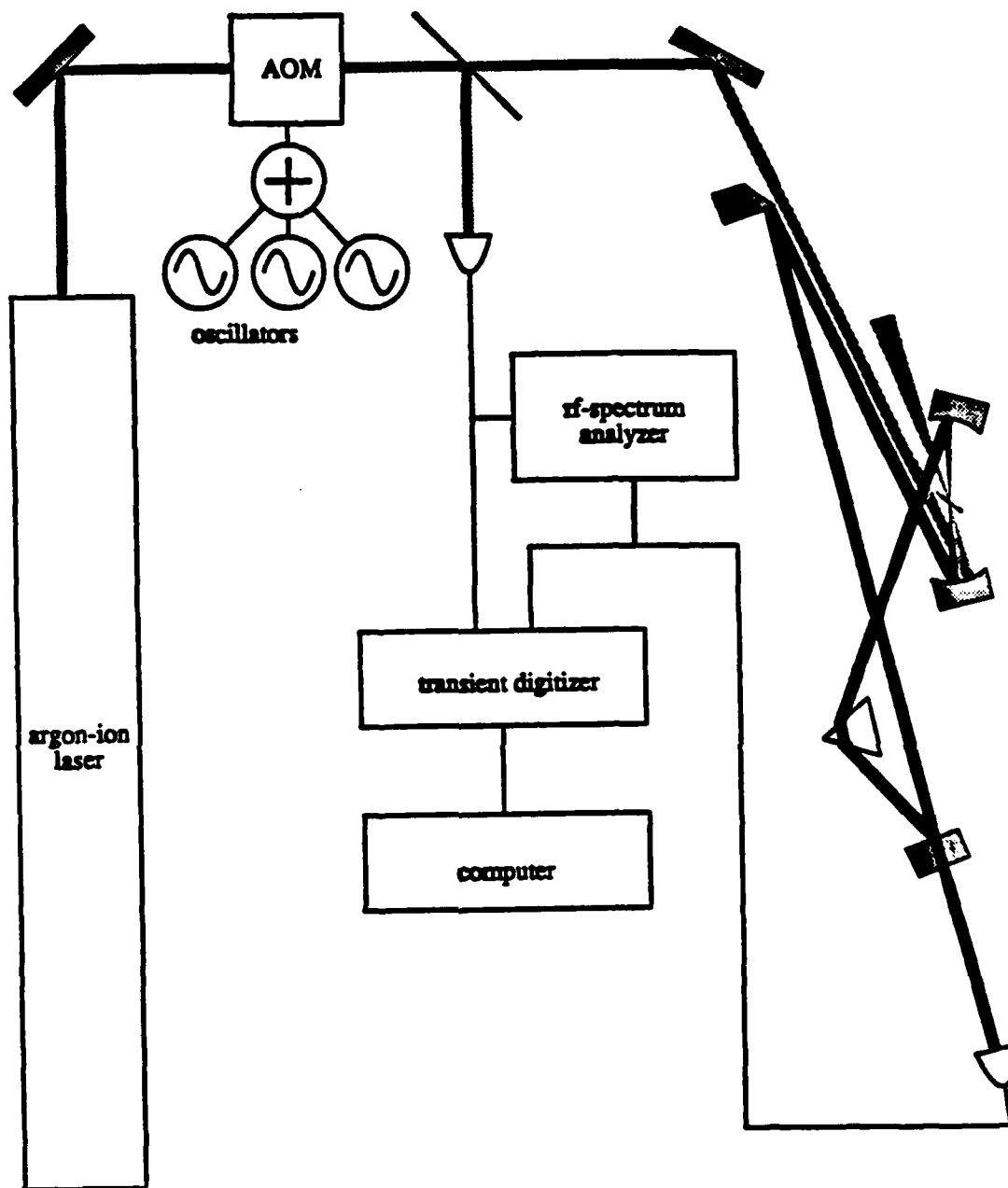


**Fig. 3.2** Experimental setup to observe modulation mixing in a high-Q multimode ring dye laser. An acousto-optic modulator (AOM) is driven by a series of oscillators. The AOM modulates the intensity of a multimode single-wavelength argon-ion laser. The modulated argon-ion laser pumps a multimode ring dye laser. We simultaneously digitize the modulated pump intensity and the output of the dye laser.

the pump laser varies between 0.90 and 0.50 in the experiments. These contrast ratios are sufficient to bring the dye laser below threshold and 5–6 times above threshold. The dye laser is similar to the lasers used in previous experiments. All the mirrors are broadband high reflectors (Virgo Optics BBHR). A Brewster-angle quartz prism is used for frequency selection. The time-averaged linewidth of the dye laser is approximately  $1\text{\AA}$ . A photodiode (Hewlett Packard PIN 4997) monitors the zeroth-order output of the acousto-optic modulator from a beam splitter. The output of the dye laser is also monitored using a photodiode. The photodiodes are biased at 15 Volts. A current-to-voltage converter with a gain of  $2\ \mu\text{V}/\text{mA}$  converts the current from the photodiode to a voltage monitored by the computer. The current-to-voltage converter is fabricated using an operational amplifier (Model:356). The response of the photodiodes drops to one half of the low-frequency response at 8 MHz. We record the signals from the photodiodes using a 10-bit transient digitizer (Sony-Tektronix Model:RTD-710). The transient digitizer simultaneously samples the two photodiodes every 200 nsec. Series of  $2^{15}$  points are transferred to a computer for analysis.

### 3. Experimental Analysis

We use a method developed by Grassberger and Procaccia<sup>75</sup> to analyze our data for the presence of deterministic noise and the generation of new frequency components. The method takes a one-dimensional time series  $x(t_i)$  and forms vectors in an embedding space of dimension  $n$ . The vectors have elements :  $x(t_i), x(t_i + \tau), x(t_i + 2\tau), \dots, x(t_i + (n - 1)\tau)$ . We choose  $\tau$  by calculating the first maxima in the area covered by a plot of  $x(t_i)$  versus  $x(t_i + \tau)$ .<sup>76-77</sup> The delay plot of  $x(t_i)$  is a diagonal line for small  $\tau$ . As  $\tau$  is increased, the correlation between points vanishes and the plot spreads over the plane. As  $\tau$  is increased further, some correlation between the points returns and the plot

collapses, approaching a diagonal line. The maximum amount of information is extracted from the delay plot when the area of the plot is maximized. The next maxima are less relevant as fluctuations and noise begin to affect the data.

The number of  $n$ -dimensional vector pairs whose ends are within a distance  $\epsilon$ ,  $C_n(\epsilon)$ , is determined as a function of  $\epsilon$  and  $n$ . In the limit that  $\epsilon$  approaches zero and  $n$  approaches infinity,  $C_n(\epsilon)$  scales as

$$\lim_{\substack{\epsilon \rightarrow 0 \\ n \rightarrow \infty}} C_n(\epsilon) \propto \epsilon^{D_2} \exp(-nK_2\tau), \quad (3.1)$$

where  $D_2$  is the correlation dimension of the attractor and  $K_2$  is the order-2 Renyi entropy. The order-2 Renyi entropy is a lower bound of the Kolmogorov entropy of the system. It has been shown<sup>75</sup> that  $K_2$  is zero for a periodic system, infinite for a stochastic system, and finite but nonzero for a chaotic system. Taking the logarithm of both sides of Eqn. (3.1) gives

$$\lim_{\substack{\epsilon \rightarrow 0 \\ n \rightarrow \infty}} \ln [C_n(\epsilon)] = D_2 \ln(\epsilon) - nK_2\tau + c, \quad (3.2)$$

where  $c$  is an arbitrary constant. In practice one plots  $\ln [C_n(\epsilon)]$  as a function of  $\ln(\epsilon)$  for a series of embedding dimensions,  $n$ . So, in the limit of large  $n$  and small  $\epsilon$ , the curves approach straight lines with slope  $D_2$ . The distance between the straight lines of successive embedding dimensions gives  $K_2\tau$ . We calculate  $C_n(\epsilon)$  for embedding dimensions of 1 to 20. The magnitude of our data ranges from 0 to 1023. Since the data are strictly integers, there is no information below  $\epsilon = 1$ . If  $\epsilon$  is large enough to contain all the ends of the vectors, we gain no information by making  $\epsilon$  any larger. Therefore, we choose the parameter  $\epsilon$  to run from 1 to 1500. We calculate  $C_n(\epsilon)$  for 400 equally spaced values of  $\ln(\epsilon)$ . We then use a 13-point linear regression analysis to calculate the slopes of the curves as a function of  $\ln(\epsilon)$ . The 13-point linear regression calculates the slope of a best fit

straight line for each group of 13 consecutive points along the  $\ln(\epsilon)$ -axis. Then we plot the calculated slopes as a function of  $\ln(\epsilon)$ . The slopes of the curves converge to  $D_2$ , the correlation dimension of the system, for large embedding dimension. We use the region of  $\epsilon$  where the slopes converge to calculate  $K_2(n)$ . We plot  $D_2(n)$  and  $K_2(n)$  as a function of embedding dimension to extrapolate their large embedding dimension values.

Some simple examples of well-characterized time series were used to test the numerical algorithm of the Grassberger-Procaccia method. The time series of one of the dimensions of the Hénon map<sup>78</sup> with parameters  $a = 1.4$  and  $b = 0.3$  gives a correlation dimension of 1.19 and a  $K_2$  of 0.42 bits/iteration agree with values in the literature.<sup>79</sup> Since the Hénon map is a discrete map, we choose  $\tau$  to be one iteration. If larger values of  $\tau$  are chosen, the points lose all correlation and the resulting time series is completely random. A single-frequency sine wave of 10 kHz, sampled every 1.6  $\mu$ sec with a 10-bit accuracy, has a correlation dimension of 1.0 and a  $K_2$  of less than 0.1 bits/period. Since there is one frequency in the system, the results for the correlation dimension agree with what we expect. The somewhat large value of  $K_2$  is a result of random noise in the digitization of the sine wave and in practice the Grassberger-Procaccia method does not give a  $K_2$  of zero for periodic signals. The sum of two sine waves of incommensurate frequencies, ( $2\pi/\omega_1 = 10$  kHz and  $\omega_2 = \omega_1(1 + \sqrt{5})/2$ ), has a correlation dimension of 2.1 and a  $K_2$  of less than 0.2 bits/period. The correlation dimension has increased with the number of incommensurate frequencies. We then analyzed the square of the sum of two sine waves of incommensurate frequencies,  $\omega_1$  and  $\omega_2$ . The square of the sum generates four frequencies:  $2\omega_1$ ,  $2\omega_2$ ,  $\omega_1 + \omega_2$ , and  $\omega_1 - \omega_2$ . Each pair of frequencies is incommensurate, which might lead one to conclude that there are four incommensurate frequencies; however, the correla-

tion dimension for this time series is equal to 2.0. Therefore, we conclude that the correlation dimension scales with the number of linearly-independent frequencies. This definition has been used in previous studies with multifrequency fields. The value of  $K_2$  for this time series approaches 0.2 bits/period. Consequently, this method of data analysis allows us to distinguish a spectrum of combination tones from a spectrum where new independent frequency components have been created. If the correlation dimension increases, we know new linearly-independent frequency components have been created. Since a change in the value of  $K_2$  signifies a change in the system's information, we also expect a corresponding change in the value of  $D_2$  for the time series with new linearly-independent frequencies. If the correlation dimension and the order-2 Renyi entropy decrease or remain the same, then we conclude that no new linearly-independent frequency components have been created.

#### 4. Experimental Results

We have carried out experiments where the pump modulation consists of one, two, three, or four modulation frequencies.<sup>80</sup> When a single frequency modulates the pump beam, the dye laser responds at the harmonics of the modulation frequency. The results obtained for two- and three-frequency modulations of the pump beam show the dye laser responds at the harmonics and combination tones of the applied modulation frequencies.

In Fig. (3.3a) we plot  $\ln [C_n(\epsilon)]$  as a function of  $\ln(\epsilon)$  for the time series of the pump modulated at three commensurate frequencies. In Fig. (3.3b) we plot  $\ln [C_n(\epsilon)]$  as a function of  $\ln(\epsilon)$  for the time series of the dye laser output.

Figures (3.4a) and (3.4b) show the results of a 13-point linear regression analysis on the curves in Figs. (3.3a) and (3.3b), respectively.

In both cases the slopes of the lines converge in the limit of large embed-



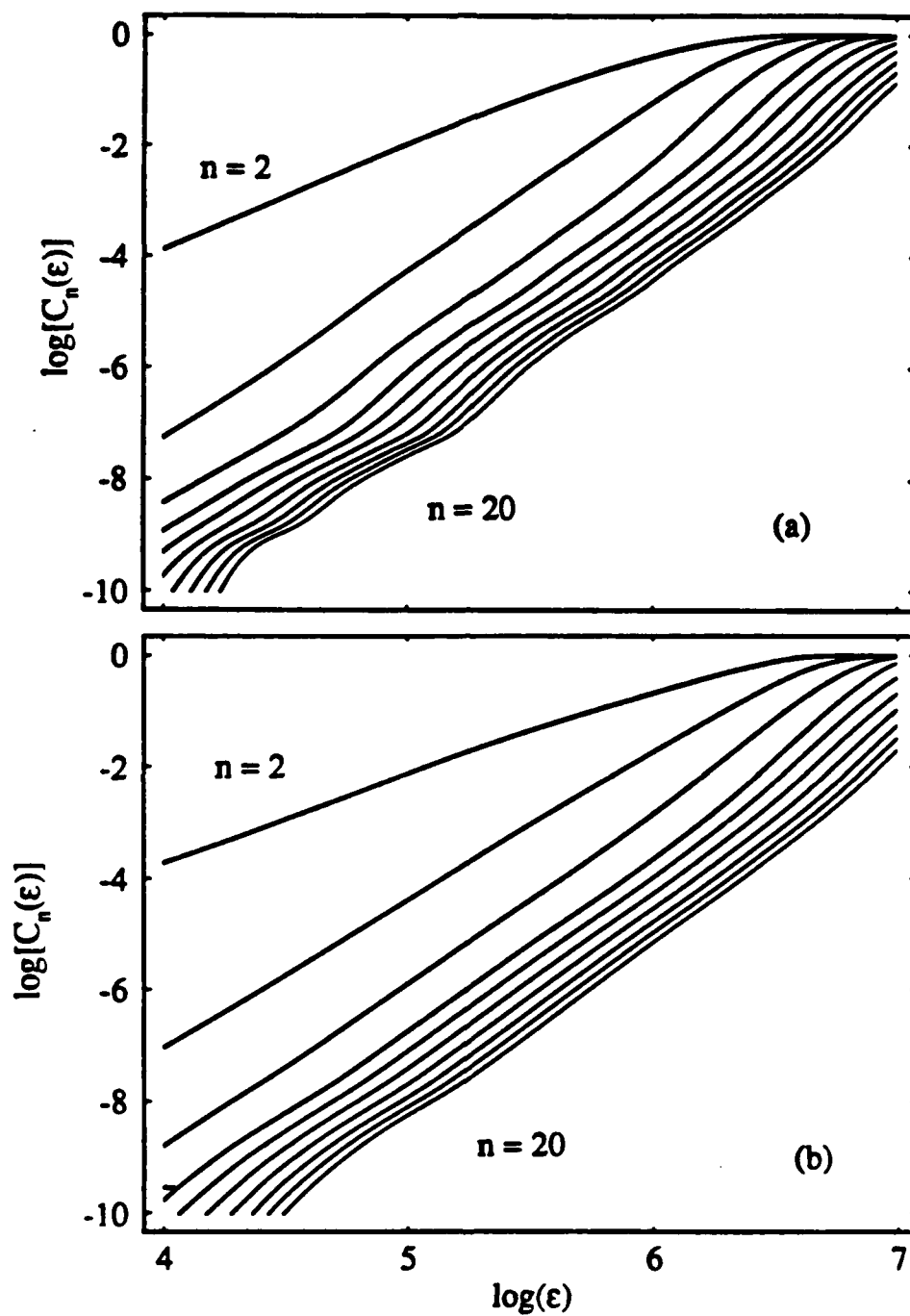


**Fig. 3.3** Logarithm of the correlation sum  $C_n(\epsilon)$  as a function of the logarithm of the hypersphere radius. (a) For the time series of the pump laser modulated at three commensurate frequencies. (b) For the time series of the dye laser driven by the pump laser modulated at three commensurate frequencies. The slopes of the curves converge to a common value over a region of  $\epsilon$ .

ding dimension. We obtain the value for  $D_2(n)$  by averaging the results of the 13-point linear regression over the region of  $\epsilon$  where the slopes converge. In Fig. (3.5a) we plot the correlation dimension  $D_2(n)$  as a function of embedding dimension for the modulated-pump time series (squares) and the dye-laser-output time series (triangles). Figure (3.5b) is a plot of  $K_2(n)$  as a function of embedding dimension for the modulated-pump time series (squares) and the dye-laser-output time series (triangles). We obtain the value for  $K_2(n)$  in the same region of  $\epsilon$  as the correlation dimension in Fig. (3.5a). The Fourier transforms of the modulated-pump time series and the dye-laser-output time series,  $F_{pump}$  and  $F_{dye}$ , are plotted in Figs. (3.6a) and (3.6b), respectively.

Since both signals are made up of well resolved harmonics, the signals are expected to be periodic. We know that the modulated-pump time series is strictly periodic and therefore  $K_2$  approaches zero for the analysis. We can interpret any deviation from zero as an indication of stochastic noise in the detection or an anomaly of the technique we are using to analyze the data. In Fig. (3.5b), any deviation in  $K_2$  for the two time series indicates the dye laser output is not periodic and has developed chaotic or stochastic noise in excess of that on the modulated pump. Figure (3.5b) indicates that for commensurate modulation frequencies the dye laser is still periodic since  $K_2$  is identical for the two time series.

In Figure (3.7a), we plot  $\ln [C_n(\epsilon)]$  as a function of  $\ln(\epsilon)$  for the time series of the pump modulated at three incommensurate frequencies.

The choice of incommensurate frequencies was made while monitoring the spectrum of the dye laser using an rf-spectrum analyzer. One oscillator remained fixed in frequency, while we vary the frequencies of the other oscillators until a broadband spectrum is observed. Figure (3.7b) is a plot of  $\ln [C_n(\epsilon)]$  as a function

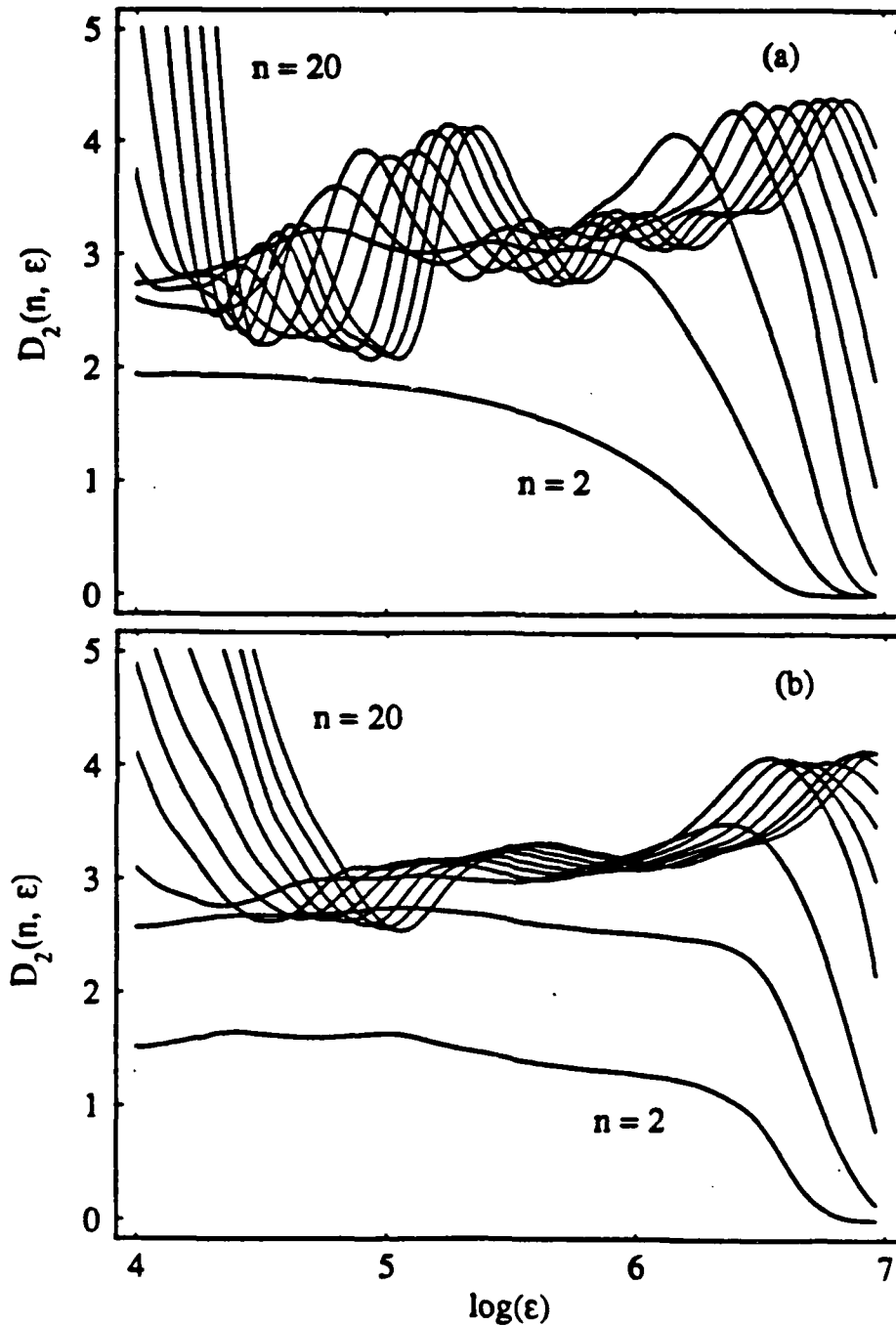


**Fig. 3.4** (a) The slopes of the curves in Fig. (3.3a) derived from a 13-point linear regression analysis. We perform a 13-point linear regression analysis to calculate the slopes of the curves in Fig. (3.3a) as a function of  $\log(\epsilon)$ . The slopes of the curves converge for a region of  $\epsilon$ . (b) The slopes of the curves in Fig. (3.3b) derived from a 13-point linear regression analysis. We perform a 13-point linear regression analysis to calculate the slopes of the curves in Fig. (3.3b) as a function of  $\log(\epsilon)$ . The slopes of the curves converge for a region of  $\epsilon$ .

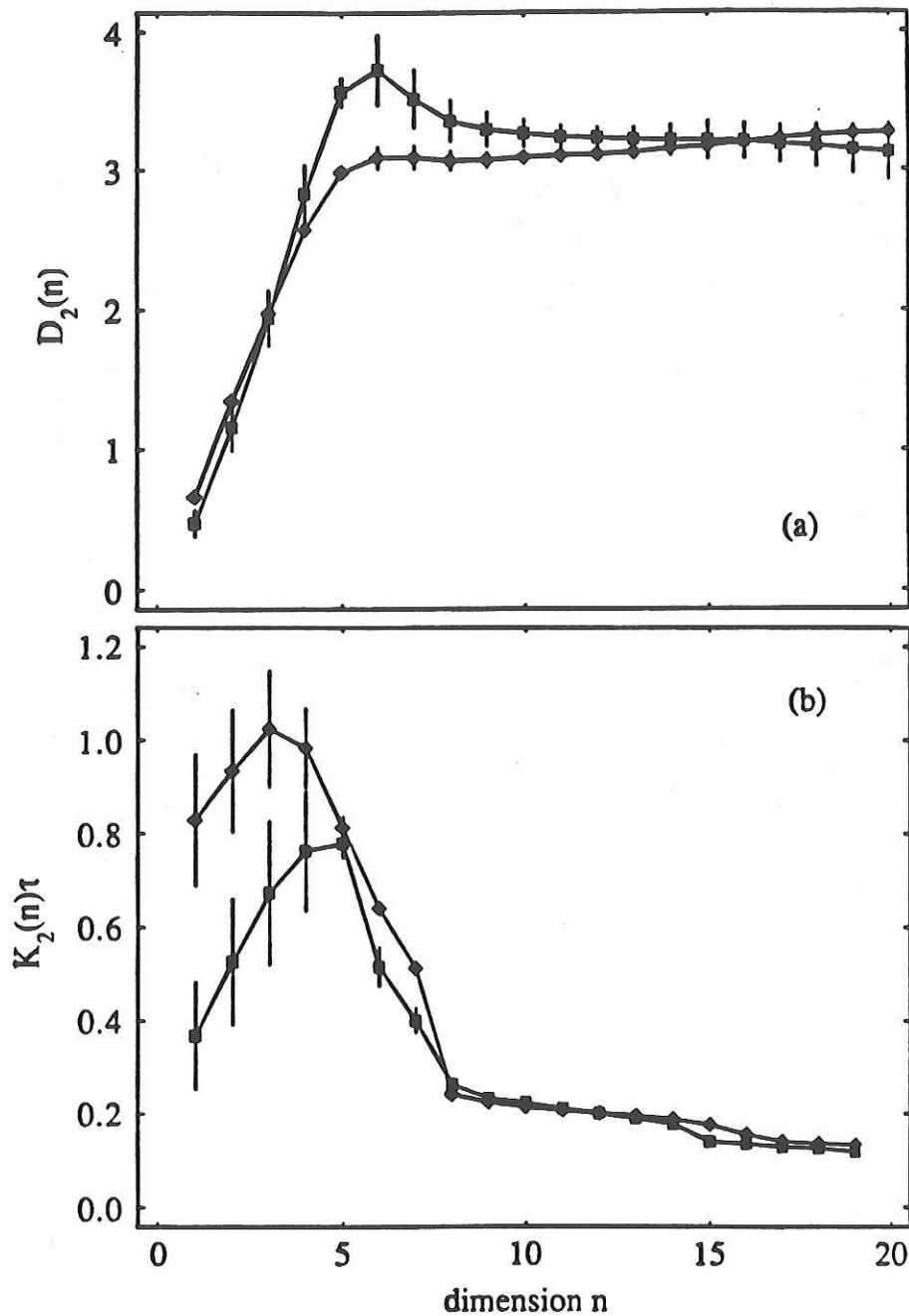
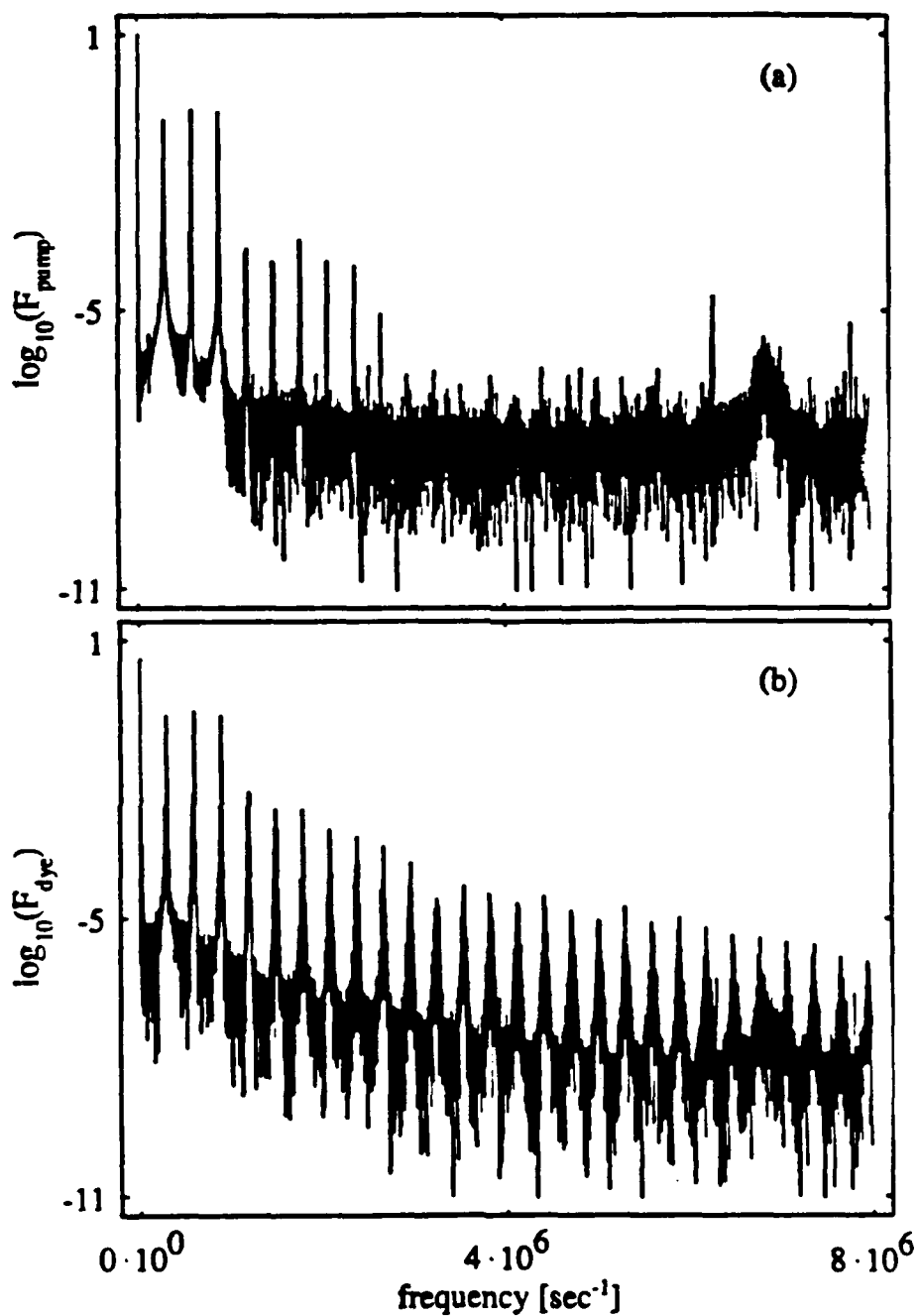


Fig. 3.5 (a) Correlation dimension,  $D_2(n)$ , as a function of the embedding dimension for the case of three commensurate frequencies. (b) Order-2 Renyi entropy,  $K_2(n)$ , as a function of the embedding dimension for the case of three commensurate frequencies. The region of  $\epsilon$  over which the slopes converge is used to calculate the distance between the curves of successive embedding dimension. The squares (triangles) represents the results for the modulated pump (dye laser).



**Fig. 3.6** (a) Fourier transform of the time series for the pump laser modulated at three commensurate frequencies. The Figure demonstrates that the pump laser is made up of three well-defined frequencies. (b) Fourier transform of the time series for the dye laser driven by the pump laser modulated at three commensurate frequencies. The Figure illustrates that the dye laser is made up of harmonics of the fundamental frequency of the argon laser.

of  $\ln(\epsilon)$  for the time series of the dye laser output. The results of a 13-point linear regression on the curves in Figs. (3.7a) and (3.7b) are shown in Figs. (3.8a) and (3.8b), respectively. Again in both cases the slopes converge in the limit of large embedding dimension. In Fig. (3.9a) we plot the correlation dimension,  $D_2(n)$ , as a function of embedding dimension for the modulated-pump time series (squares) and the dye-laser-output time series (triangles). We obtain the values for  $D_2(n)$  in a manner similar to those in Fig. (3.5a). Figure (3.9b) is a plot of  $K_2(n)$  as a function of embedding dimension for the modulated-pump time series (squares) and the dye-laser-output time series (triangles). The Fourier transforms of the modulated-pump time series and the dye-laser-output time series,  $F_{pump}$  and  $F_{dye}$ , are plotted in Figs. (3.10a) and (3.10b), respectively. While the spectrum in Fig. (3.10a) is a finite series of discrete components, the spectrum of Fig. (3.10b) is a broadband spectrum. However, from Figs. (3.9a) and (3.9b) we see the values of  $D_2(n)$  and  $K_2(n)$  that the dye-laser-output time series converges to are identical to those of the modulated-pump time series. We can conclude that since the correlation dimension,  $D_2$ , is identical for both time series that no new independent frequency components have been created and the spectrum of the dye laser output is composed purely of combination tones of the modulated-pump spectrum. This indicates that even though the dye laser output is quite complicated, it is merely quasiperiodic.

Similar experiments were carried out for two-, three- and four-frequency modulations. The frequencies varied over the range of 1 kHz to 400 kHz. The results of these other experiments are similar to the results of the three-frequency modulation discussed above. In all these cases no chaos was detected in the output of the dye laser.

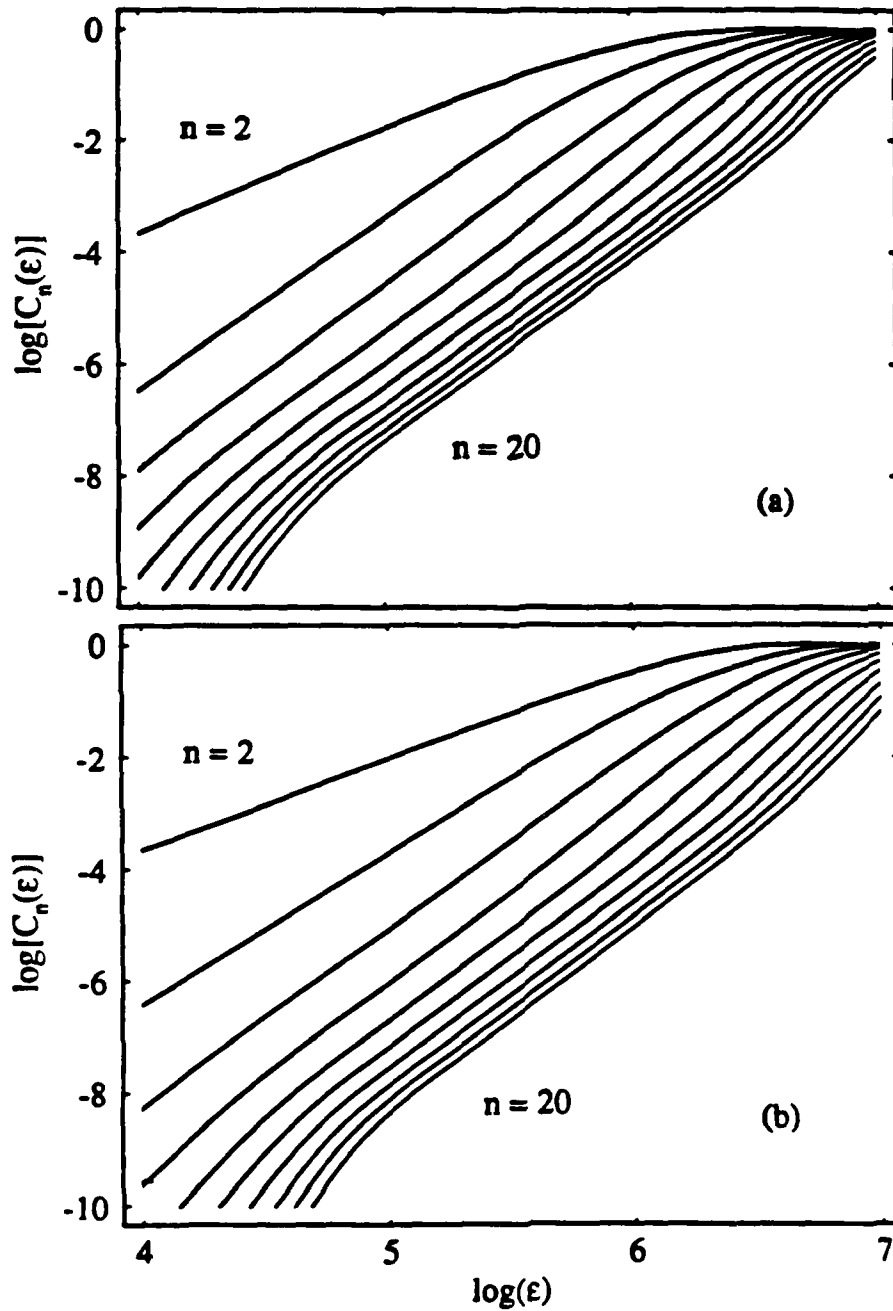


**Fig. 3.7** Logarithm of the correlation sum  $C_n(\epsilon)$  as a function of the logarithm of the hypersphere radius. (a) For the time series of the pump laser modulated at three incommensurate frequencies. (b) For the time series of the dye laser driven by the pump laser modulated at three incommensurate frequencies. The slopes of the curves converge to a common value over a region of  $\epsilon$ .

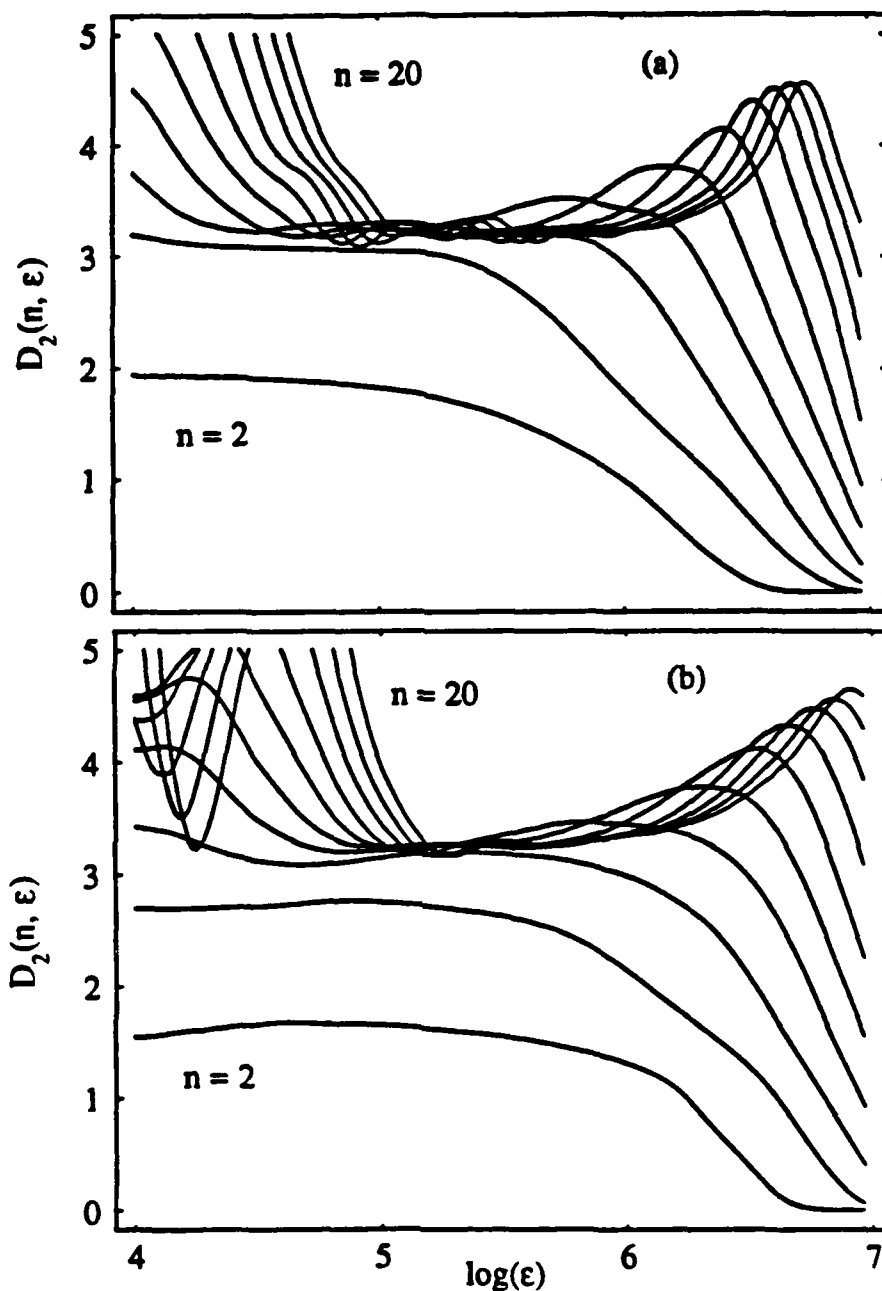


**Fig. 3.8** (a) The slopes of the curves in Fig. (3.7a) derived from a 13-point linear regression analysis. We perform a 13-point linear regression analysis to calculate the slopes of the curves in Fig. (3.3a) as a function of  $\log(\epsilon)$ . (b) The slopes of the curves in Fig. (3.7b) derived from a 13-point linear regression analysis. We perform a 13-point linear regression analysis to calculate the slopes of the curves in Fig. (3.3a) as a function of  $\log(\epsilon)$ . The slopes of the curves converge for a region of  $\epsilon$ .



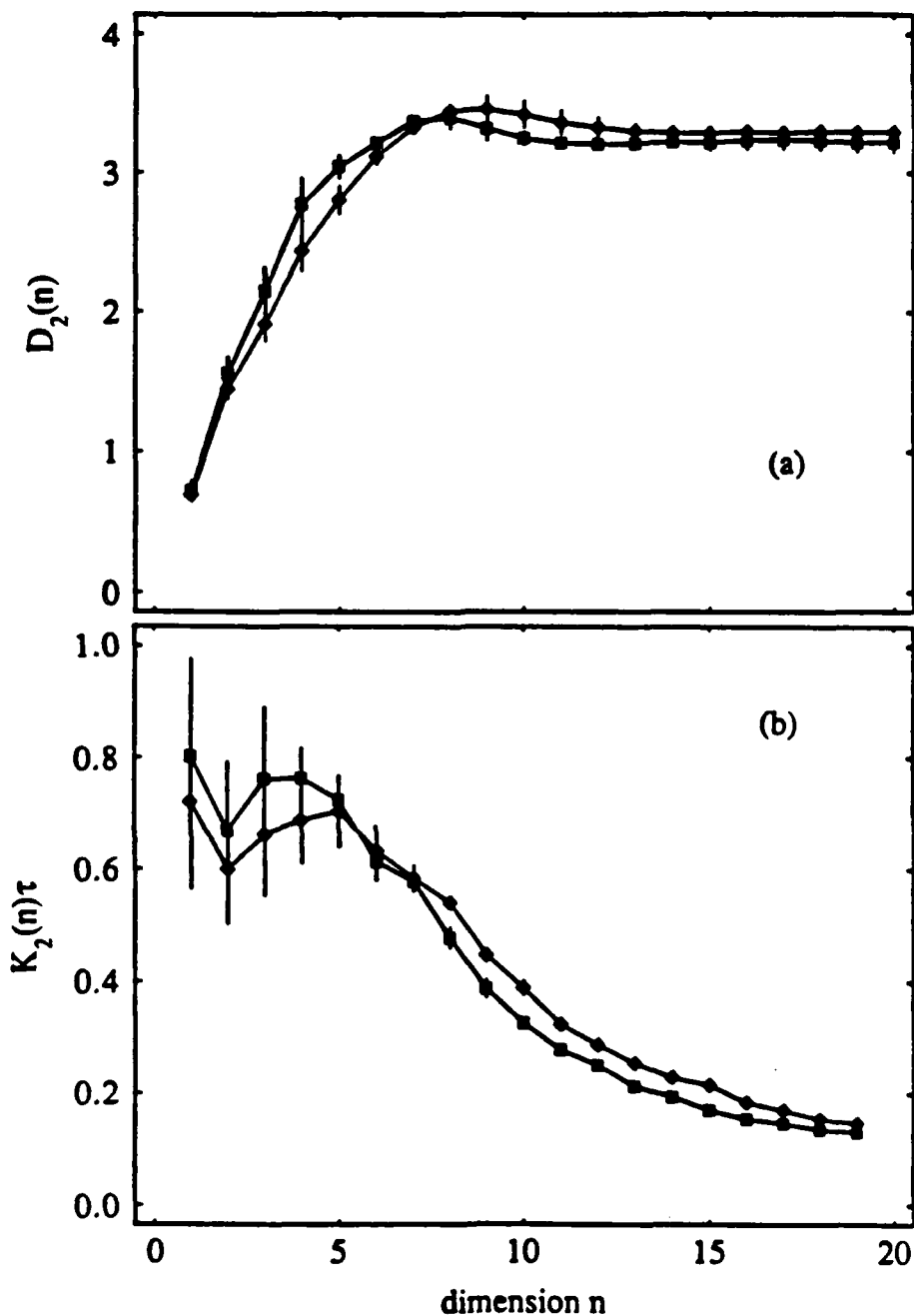
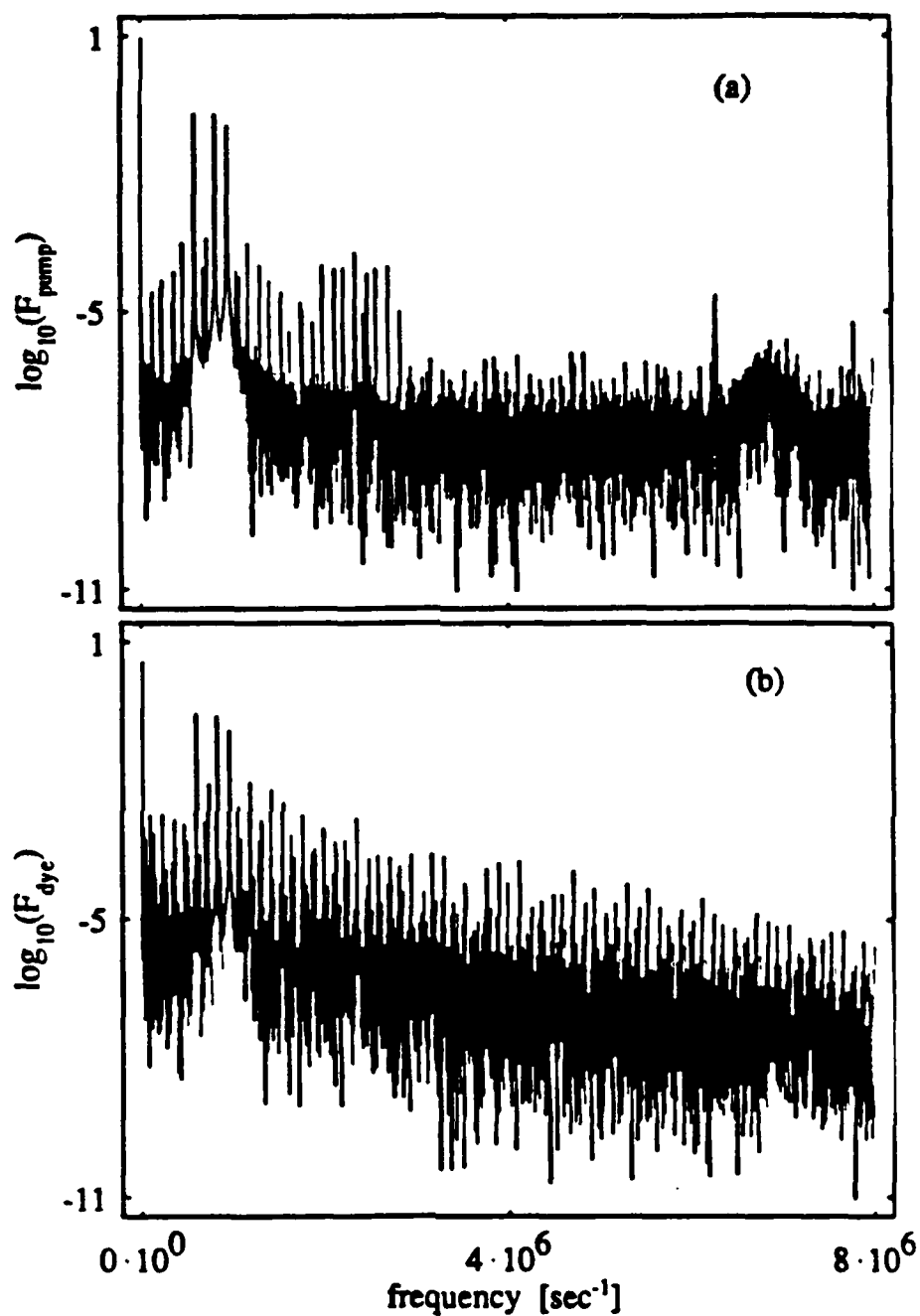


Fig. 3.9 (a) Correlation dimension,  $D_2(n)$ , as a function of the embedding dimension for the case of three incommensurate frequencies. (b) Order-2 Renyi entropy,  $K_2(n)$ , as a function of the embedding dimension for the case of three incommensurate frequencies. The region of  $\epsilon$  over which the slopes converge is used to calculate the distance between the curves of successive embedding dimension. The squares (triangles) represents the results for the modulated pump (dye laser).



**Fig. 3.10** (a) Fourier transform of the time series for the pump laser modulated at three incommensurate frequencies. The figure illustrates that the pump laser is composed predominantly of three frequencies. The harmonics and combination tones appear due to the nonlinear detection scheme of the photodiode. (b) Fourier transform of the time series for the dye laser driven by the pump laser modulated at three incommensurate frequencies. The figure demonstrates that the dye laser is composed of a broad band of frequencies.

## 5. Conclusions

We find that the correlation dimension of a system scales with the number of linearly-independent frequencies. This fact allows us to separate broadband spectra which are truly broadband from broadband spectra which are dense spectra of combination tones. These conclusions were facilitated by careful use of an embedding-space technique developed by Grassberger and Procaccia.<sup>75</sup> It should also be noted that if shorter time series were used in the analysis, the slopes of the curves,  $\ln [C_n(\epsilon)]$  versus  $\ln(\epsilon)$ , do not converge. The embedding-space technique classifies such time series as noise. It is interesting to note that a Fourier transform of the truncated time series would not resolve the combination tones in the dye laser spectrum. The embedding technique, however, is much more convenient than a Fourier transform for distinguishing truly broadband spectra from complicated spectra of combination tones. We show that the output of a multimode dye laser, driven by a modulated pump, exhibits broadband spectral features which are simply combination tones of the pump source modulation frequencies. This indicates the mechanism responsible for the broadband spectrum generates new frequencies from combination tones of the existing frequencies. Phase-matched four-wave mixing is a simple example of how these new frequencies might be generated. The large depth of pump modulation makes it possible for higher-order mixings to become of comparable significance as well.

We also show that the high-Q multimode ring dye laser has stable multifrequency quasiperiodic attractors for two, three, and four incommensurate driving frequencies. These results are similar to the results of Grebogi *et al.*<sup>70-72</sup> The absence of chaos in this system is somewhat surprising given the extreme nonlinearities of the system which are illustrated in Fig. (3.1). A partial answer

to this puzzle is that the hysteresis loops observed in Fig. (3.1) do not remain stable for multifrequency pumping. The transition points of the hysteresis loop do not remain fixed. This is related to critical slowing down that takes place at this second instability threshold. Clearly, further study of this phenomenon will be very important in completely understanding the results of this experiment.

## Chapter IV

### DYE LASER EXPERIMENTS

#### 1. Introduction

In this Chapter we discuss a series of experiments examining the two-frequency instability in a continuous-wave (cw) dye laser. A homogeneously broadened cw ring dye laser is a simple laser system. The theoretical description of such a laser is useful in understanding the self-consistent dynamic interaction of a coherent field with an atomic system. In 1984, Hillman et al.<sup>43</sup>, experimentally demonstrated an instability in a cw rhodamine-6G ring dye laser that, although appealingly simple in its characteristics, resisted quantitative understanding until only recently. In this experiment, the power of the argon-ion pump laser is gradually increased; the dye laser operates in a single mode when the pump power is sufficient to bring the laser above threshold. As the pump power is increased to 1.4 times above the first threshold, the laser passes through a second threshold, at which point the spectrum of the laser discontinuously splits into two components separated by approximately 7 Å. At this same point the output of the laser also changes discontinuously, increasing by

a factor of two. As the pump power is increased even further, the two spectral components spread apart until they reach a separation of  $\sim 80 \text{ \AA}$ . The splitting of the two components scales proportionally to the square root of the output laser intensity or directly proportionally to the Rabi frequency of the laser transition. At a pump power of approximately 2.5 times above the first laser threshold, a third threshold of instability is encountered. The spectrum of the laser collapses to a two-frequency state whose separation is approximately  $10 \text{ \AA}$ . At this third threshold, the dye laser output power discontinuously jumps again by a factor of approximately two. As the pump power was increased above this third instability threshold, the spectral components again show a power dependent separation. At both the second and third instability thresholds, the output power demonstrates hysteresis as the pump power was adjusted up and down through the threshold.

This Chapter addresses the question of whether or not the two-frequency instability is intrinsic to the laser atom interaction or due to some other features of the experiment. We have examined the effects of the pump laser spectrum, cavity dispersion, cavity Q, cavity detuning, unidirectional operation, and age of the dye solution on the two-frequency instability.

## 2. Robustness of the Two-Frequency Instability

The initial experiments were performed with an argon-ion laser operating in a multi-wavelength configuration. The absorption band of the rhodamine-6G dye molecule peaks in the region of  $5145 \text{ \AA}$ , the strongest line of the argon-ion laser. However, there is still considerable cross section for the absorption of the other wavelengths of the argon-ion laser. The energy difference between the pump photons and the subsequently emitted dye laser photons is converted

to thermal energy in the dye molecule. This means that wavelengths shorter than 5145 Å will cause the dye molecule and its solution to heat up more than if the dye laser were pumped solely with the 5145 Å wavelength. We performed experiments with the dye laser pumped by a single wavelength (5145 Å) laser to investigate the effects of the absence of excess heating on the two-frequency instability.

The initial experiments employed a strongly dispersive flint-glass Brewster-angled prism for wavelength selection of the dye laser. The prism provides wavelength discrimination in the large ( $\sim 250$  Å) gain-bandwidth of the dye molecule. Predictions were made, concerning the behavior of the spectral components of the two-frequency state above the instability threshold, that involved the dispersion of the cavity. Using a weakly dispersive quartz-glass Brewster-angled prism we conducted experiments to investigate the effects of the prism's dispersion on the two-frequency instability in the dye laser.

Since the frequency separation of the field components depends on the amplitude of the laser field, the instability has been associated with Rabi oscillations. In order to maximize the field strength of the laser, the initial experiments were performed in a high-Q laser. All the mirrors in the laser cavity were broadband high reflectors. To investigate the effects of cavity Q, we performed experiments on a dye laser with a 5 % output coupler. The increase in the threshold for oscillation was compensated by providing higher pump powers.

The initial experiments were conducted in a bidirectional ring laser. Counterpropagating waves in nonlinear media are known to produce instabilities and chaos.<sup>81</sup> We employ two techniques to force the ring dye laser to operate in a single direction of oscillation and then observe the effects this has on the two-

frequency instability. The first technique for producing unidirectional operation involves retroreflecting one of the directions of oscillation back into the cavity. We monitor the two Fresnel reflections coming from the prism in the laser cavity. One reflection results from one of the laser's directions of propagation; the other reflection results from the other direction of propagation. When the retroreflection of one of the directions is properly aligned, the Fresnel reflection from this direction of oscillation is observed to vanish. The field does not completely extinguish itself, but a ratio of intensities of approximately 80:1 was obtained between the two directions of propagation. The technique is not very effective if the beam to be retroreflected exits the cavity from a mirror with a high reflectivity. The beam is weak and the amount of light that makes it back into the cavity is insufficient to force the laser into unidirectional operation. We retroreflect the output from the 5%-transmission mirror. The intensity in this case is sufficient for the effect to occur.

Figure (4.1) shows the experimental setup to observe the dye laser spectrum as a function of pump intensity. The mirror external to the laser cavity is used to force the laser into unidirectional operation. Its retroreflection can be blocked to allow the ring dye laser to operate bidirectionally. We use a single-wavelength argon-ion laser to pump the dye laser. The current supplied to the argon tube is controlled by a digital-to-analog interface in the computer. The spectrum of the laser is measured using a quarter-meter Jarrell-Ash spectrometer. The image plane of the spectrometer contains an intensified CCD array of 700 exposed elements. An optical multichannel analyzer (OMA) controls the CCD array. The spectrometer and CCD array combination has a resolution of approximately  $2\text{\AA}$ . The computer adjusts the intensity of the pump laser. It waits a set amount of



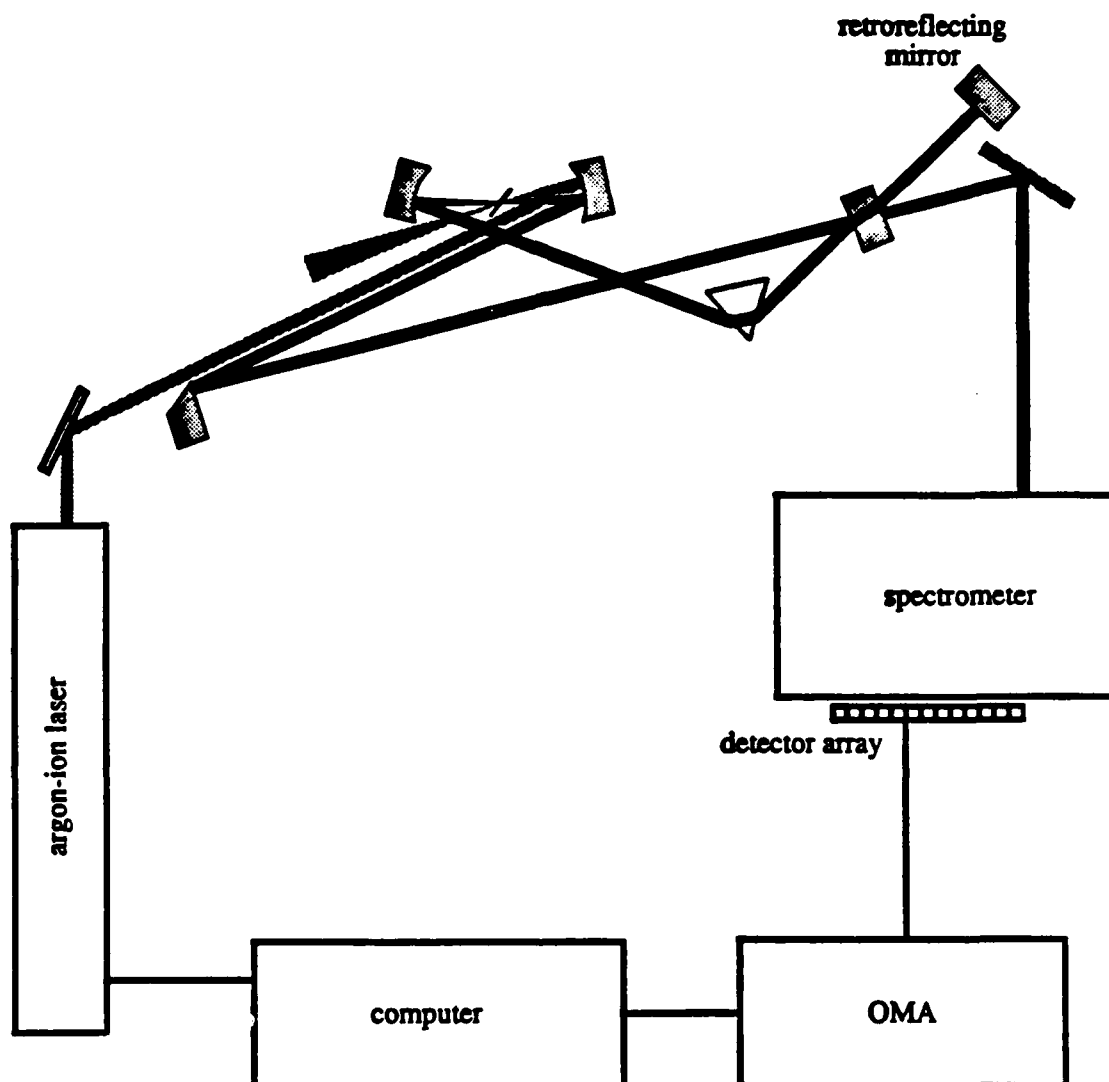


**Fig. 4.1** Schematic diagram of a cw pumped multimode ring dye laser. All the mirrors in the cavity are broadband high reflectors. The computer controls the argon laser power and signals the optical multichannel analyzer (OMA) when the spectra should be taken. The OMA reads  $\sim 700$  pixels from a diode array in the image plane of a quarter-meter spectrum analyzer. A retroreflecting mirror is used to force the laser into unidirectional behavior, or is blocked so the dye laser can oscillate bidirectionally.

time and then sends a trigger pulse to the OMA. On receiving the trigger pulse, the OMA samples the spectrum of the dye laser and stores it in memory. The OMA then sends a trigger pulse to the computer. On receiving the trigger pulse from the OMA, the computer readjusts the pump intensity and the process repeats until the maximum pump laser intensity is reached. Figure (4.2) and (4.3) show the dye laser spectrum as a function of pump power for both unidirectional and bidirectional operation. We can see from the Figures that the instability is still present in the unidirectional case, though some slight modifications take place in the region of the spectrum's bifurcation. The spectral components are seen to split out to approximately  $240\text{\AA}$ . This is three times the splitting observed in the original experiments by Hillman *et al.*<sup>43</sup> While this method of producing unidirectional operation is successful, it modifies the rf-spectrum of the oscillating direction. It was found that the cavity-mode beat notes could be enhanced or diminished depending on the distance of the retroreflecting mirror from the output coupler. This complication, as well as the fact that the counterpropagating direction of oscillation is not completely extinguished, left a certain amount of skepticism<sup>82</sup> as to whether or not a counterpropagating field is necessary for the two-frequency instability. We then attempted to force the laser to oscillate unidirectionally using another method.

The second method of achieving unidirectional operation involved employing a Faraday rotator and a quartz-crystal compensation plate. The Faraday rotator is a samarium-cobalt permanent magnet mounted around a piece of SF-56 flint glass with a large Verdet constant. The polarization of the light is rotated in a clockwise or counter clockwise sense, depending on the direction of propagation with respect to the magnetic field of the permanent magnets.

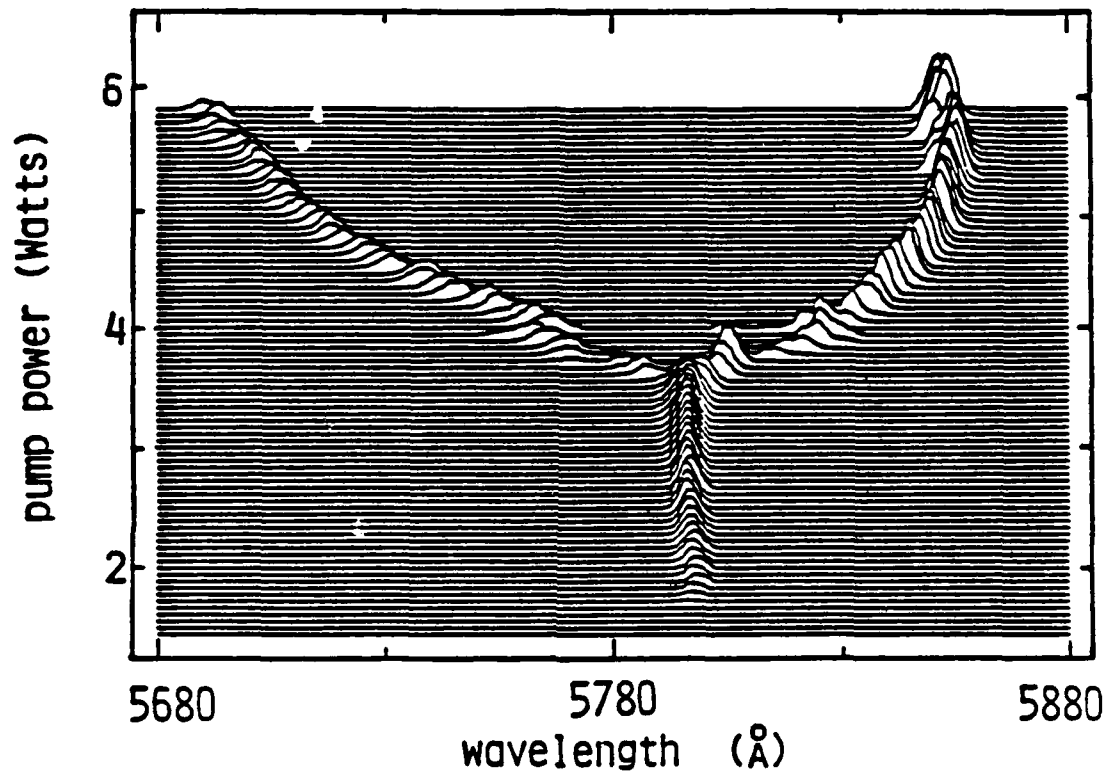


**Fig. 4.2** Optical spectrum of a bidirectional ring dye laser as a function of pump power. The Figure clearly shows the dye laser spectrum bifurcating above a threshold value. The unequal intensities of the two spectral components were caused by a misalignment of the detector array.

The quartz-crystal compensation plate rotates the polarization of the light independent of the direction of propagation. Therefore, with proper adjustment of the quartz-crystal plate, the polarization of one of the directions of propagation will suffer no net rotation on a round trip in the cavity. The other direction of propagation will suffer some net rotation, creating a component of s-polarization. The s-polarization component experiences additional losses at the Brewster-angled surfaces in the cavity. This additional loss is sufficient to force the laser into unidirectional operation with a ratio of intensities of approximately 200:1 between the two directions of propagation. The amount of loss introduced to both directions, however is quite large; the additional losses suffered at the Brewster-angled surfaces of the Faraday rod and the scattering in the Faraday rod increase threshold for oscillation and make it more difficult to achieve the necessary intracavity power for the instability to occur. The experimental setup is shown in Fig. (4.4). The Faraday rotator is constructed in such a way that it is easy to remove the samarium-cobalt magnets from around the rod. When there is no magnetic field present, the Faraday rod does not rotate the polarization, and therefore does not function as a unidirectional device. This enables us to conveniently compare the unidirectional operation of the laser with the bidirectional operation. In Figs. (4.5) and (4.6), we show the dye laser spectrum as a function of pump power for both modes of operation. The mode structure of the spectrum is due to the quartz-crystal compensation plate which acts like an etalon. The structure on the spectrum is the free-spectral range of the compensator plate. The conclusions we reach from the Figures are that the two-frequency instability is not an artifact of the bidirectional ring laser.

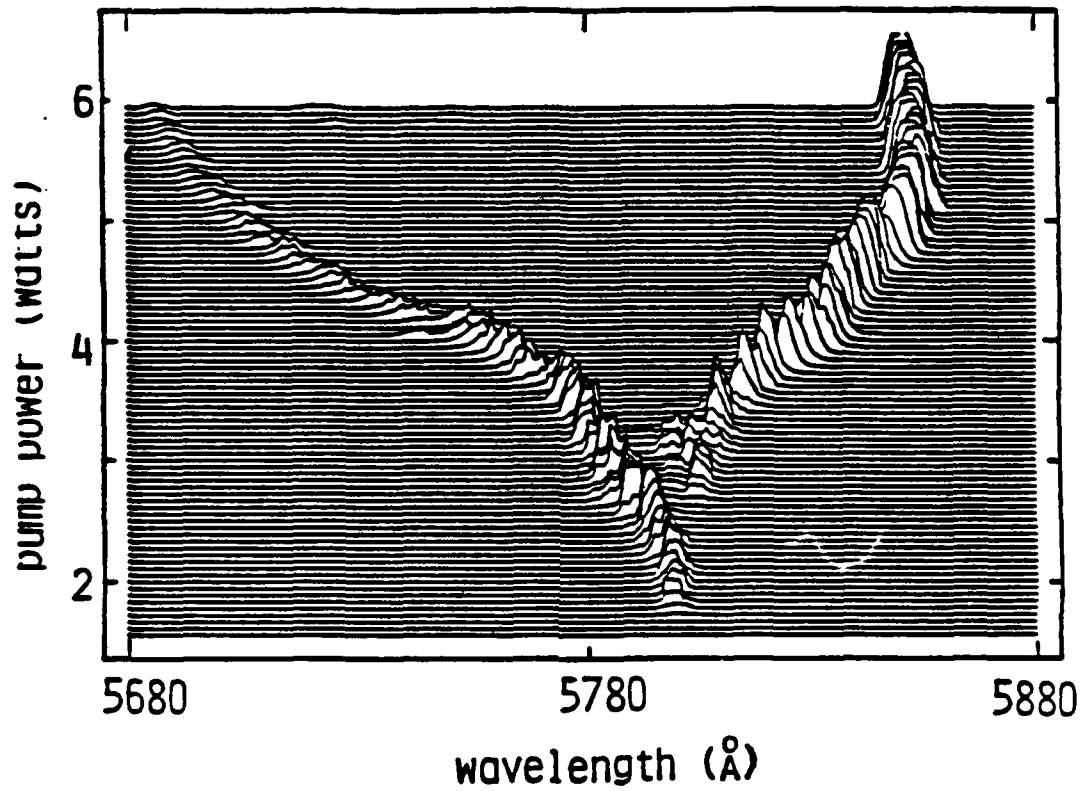


**Fig. 4.3** Optical spectrum of a unidirectional ring dye laser as a function of pump power. This figure demonstrates that even when the dye laser runs unidirectionally, the spectrum still bifurcates. The spectral behavior is somewhat altered near the instability threshold. The unequal intensities of the two spectral components were caused by a misalignment of the detector array.

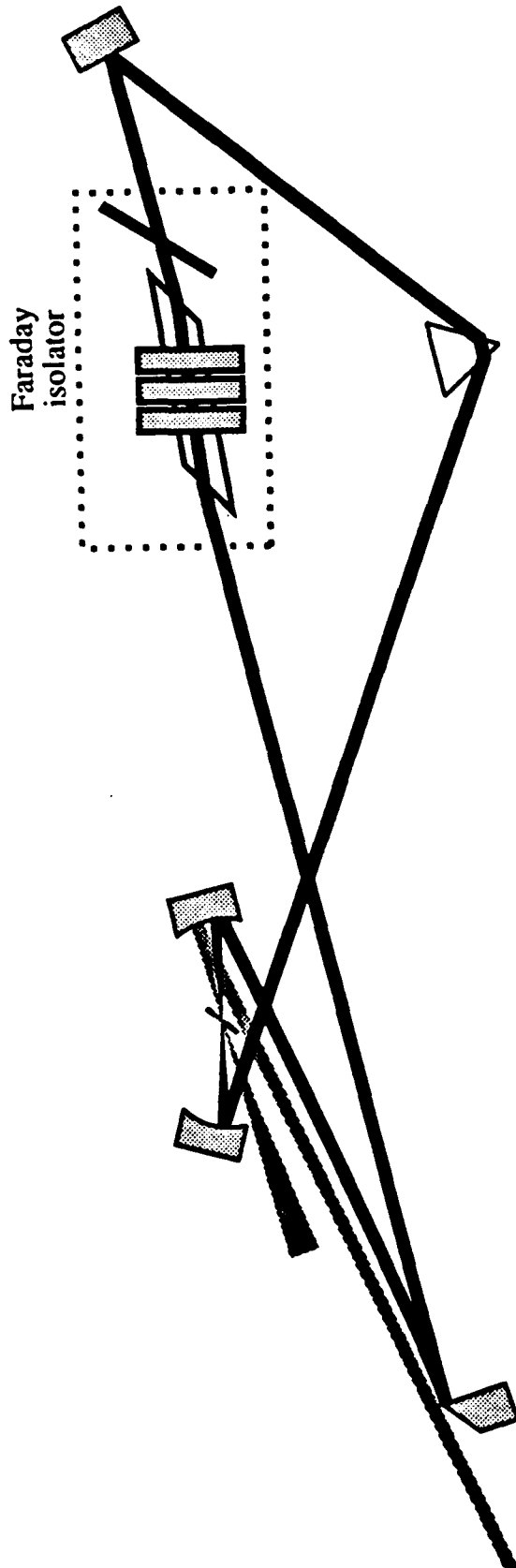


**Fig. 4.4** Schematic diagram of a cw pumped multimode ring dye laser with a Faraday rotator. The Faraday rotator and the quartz-crystal compensation plate compose the unidirectional device. The magnet in the Faraday rotator is easily removed allowing easy comparison between a unidirectional and bidirectional cavity with comparable cavity Q's.

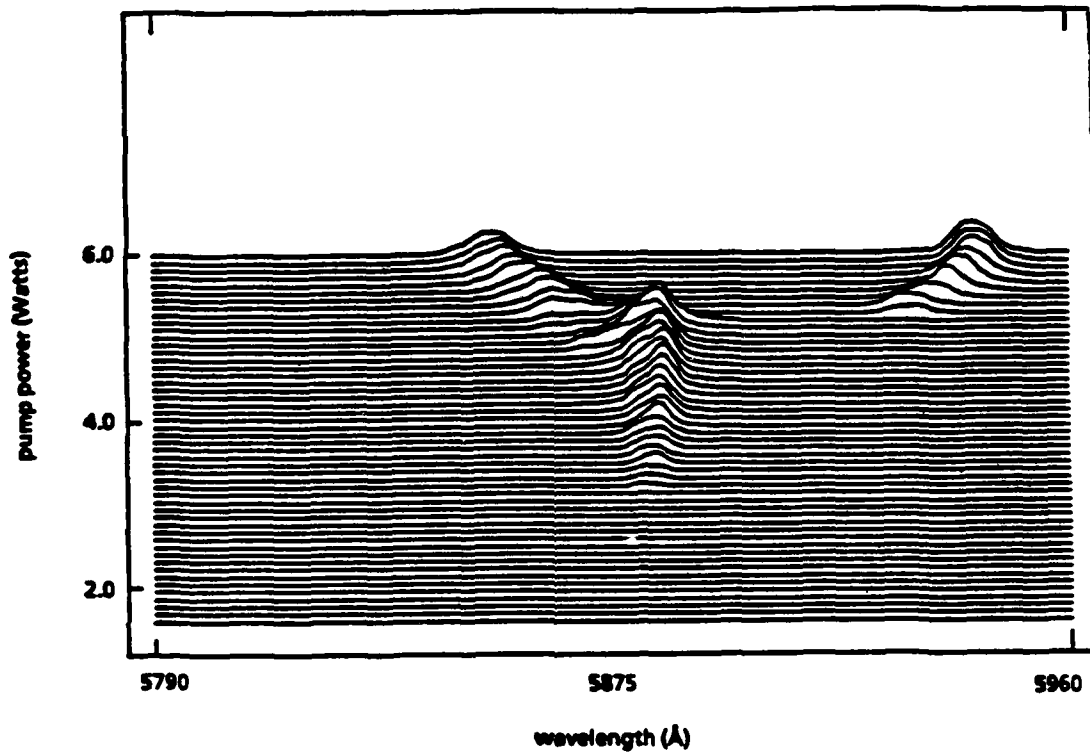


Fig. 4.5 Optical spectrum of a bidirectional ring dye laser as a function of pump power. The magnet was removed from the Faraday rotator and the quartz-crystal compensation plate was removed from the laser cavity. The dye laser operates bidirectionally.

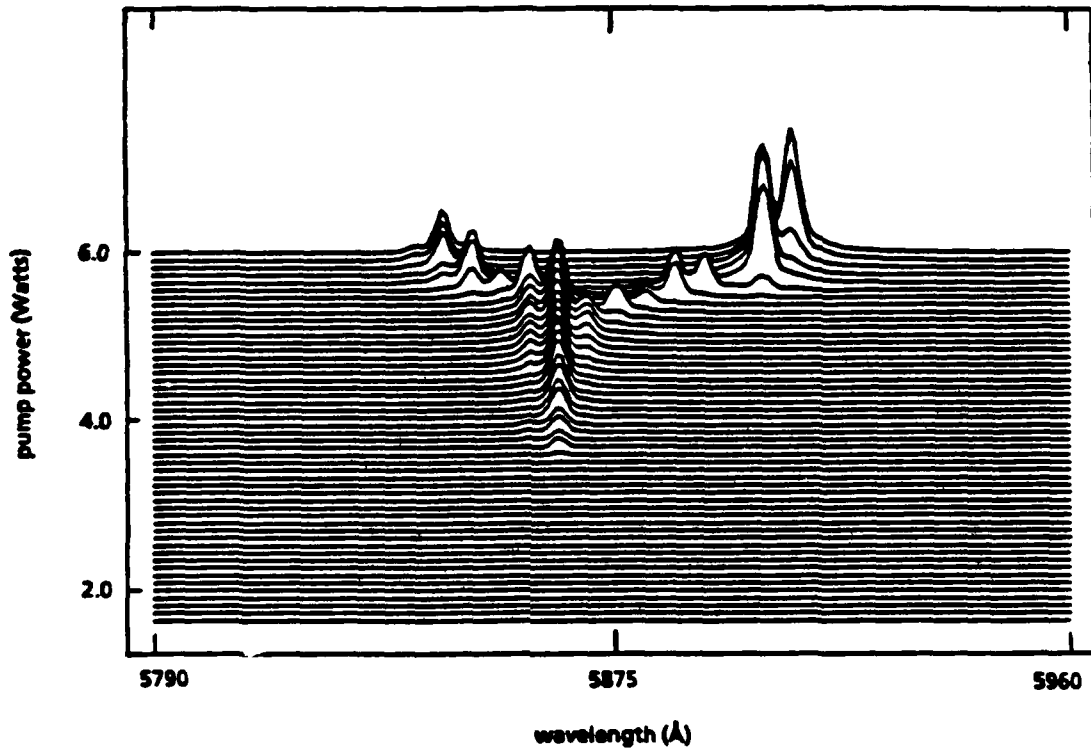


Fig. 4.6 Optical spectrum of a unidirectional ring dye laser as a function of pump power. The magnet and compensator plate are in place and the dye laser operates unidirectionally.



### 3. Effects of Detuning

The instability was also investigated as a function of dye laser detuning.<sup>45</sup> In previous experiments the prism was adjusted so that the laser operated at low pump power at the center of the gain curve. The splitting then is approximately symmetric about the initial lasing frequency. Figure (4.7) shows the results of a series of experiments in which the prism is adjusted to produce operation at various detunings on each side of the center of the gain curve. The detuning from the center of the gain curve is indicated in the upper right corner of each figure. The curves show the spectrum of the output of the dye laser for a series of pump powers from lasing threshold at 1.3 Watts to 6.8 Watts. In each case, the laser operates in a single mode with very little frequency pulling from threshold up to a second threshold in the vicinity of 6 Watts of pump power. The behavior of the laser at the second threshold depends sensitively on the detuning from the center of the gain curve. For the case of  $\Delta\lambda = 0$ , the spectral component at the original lasing frequency vanishes and two symmetrically detuned components appear separated by approximately 75 Å. These two components then separate symmetrically to  $\sim 175$  Å as the pump power is increased. When the prism is tuned so that the laser begins lasing  $\sim 10$  Å off of the gain center ( $\Delta\lambda = 10\text{Å}$ ), the behavior is somewhat different. At the second threshold there is no longer a symmetric splitting, instead a component on the other side of the center of the gain curve splits off discontinuously, while the component on the other side is generated continuously from the original component. In other words, a new spectral component appears discontinuously and the original central component is repelled by it. This behavior is even more dramatically demonstrated in the case where the prism is adjusted so that the laser initially operates  $\sim 25\text{Å}$  off

of the center of the gain curve ( $\Delta\lambda = 25\text{\AA}$ ). In this case, the spectrum of the dye laser above the instability threshold is clearly marked by the appearance of a new spectral component on the other side of the gain curve, followed by a repelling of the two spectral components. The result is that the dye laser spectrum splits assymmetrically at high powers. Also included in Fig. (4.7) are the spectra from two examples where the prism is adjusted so that at low powers the laser operates at frequencies detuned from the center of the gain curve by  $-10\text{\AA}$  and  $-25\text{\AA}$  ( $\Delta\lambda = -10\text{\AA}$  and  $\Delta\lambda = -25\text{\AA}$ ), symmetrically opposite the cases previously discussed. The results are the mirror images of those discussed previously.

The spectral splittings at high power in the various spectra of Fig. (4.7) are as large as  $200\text{\AA}$ . A field made up of two equal-amplitude frequency components separated by  $200\text{\AA}$  corresponds to a wave train of femtosecond pulses. Fork and Valdmanis<sup>63</sup> have observed that in order to produce extremely short femtosecond dye laser pulses — which require a very large bandwidth — it is necessary to use fresh dye solution. Aged dye solution contains optically damaged molecules that absorb in the red end of the spectrum. This degrades the dye molecules performance as an amplifier and a laser active medium. The criteria for producing large splittings would seem to be very similar to producing short pulses. To investigate this point, we prepared a fresh dye solution and repeated the experiments. The results are shown in Fig. (4.8). The results change appreciably when a new dye solution is used. The center of the gain curve has shifted to  $5940\text{\AA}$  and splittings as large as  $340\text{\AA}$  are observed, nearly twice the size of the splittings previously observed. The similarities between the conditions needed for ultrashort pulse production and those needed for large spectral

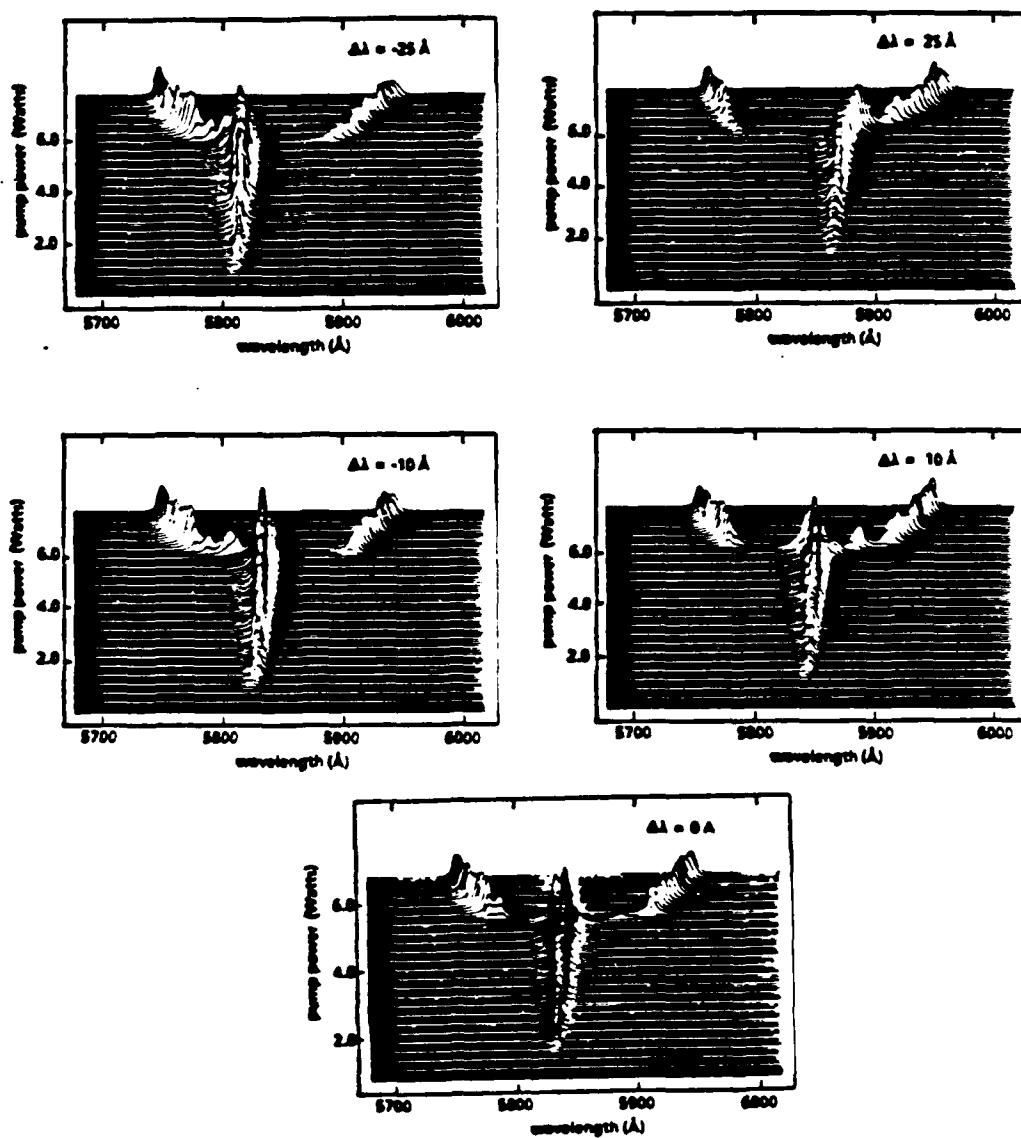


Fig. 4.7 The effects of cavity detuning on the two-frequency instability. This Figure shows how the spectrum of the dye laser is affected by the detuning of the dye laser.

splitting, suggest a close connection between the two-frequency instability and mode locking dye lasers.

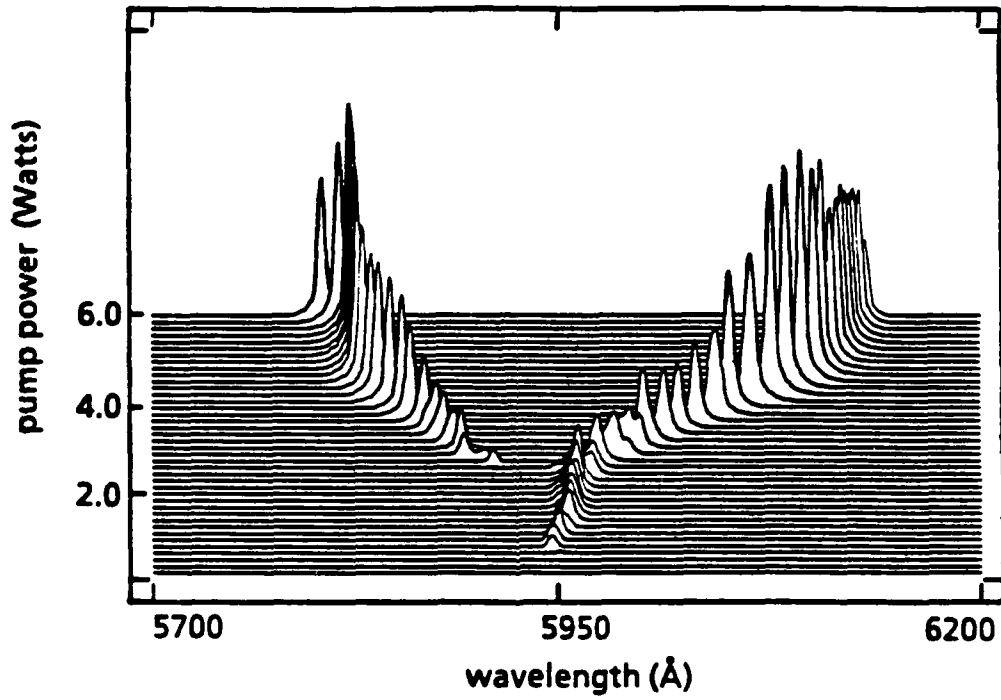


Fig. 4.8 Giant mode splitting in a ring dye laser. A  $340\text{\AA}$  splitting and a shift in the dye laser spectrum were observed when the dye solution was replaced with freshly mixed dye solution.

## Chapter V

### THE BAND MODEL FOR DYE LASERS

#### 1. Introduction

The experiments of Stroud and coworkers<sup>43-45</sup> demonstrated that a continuous-wave dye laser exhibits an instability close to the first laser threshold. The instability is characterized by three main signatures: (1) the threshold for instability of the single frequency solution is much lower than nine times above threshold as predicted by the simple two-level analysis, (2) the output intensity displays discontinuous intensity jumps and associated hysteresis loops around the instability thresholds, and (3) the spectrum of the laser above the second instability threshold is made up of two frequency components whose separation increases as the square root of the laser power. Many attempts were made to explain this behavior theoretically. Some progress has been made in reproducing some of the features of the experiment; however, none of the attempts satisfactorily explained all three of the experimental signatures.

Hillman and Koch<sup>28</sup> introduced a method of integrating the multimode Maxwell-Bloch equations (MMMBE) using a Fourier transform technique. The

method uses Fourier transforms to evaluate the spatial derivative in the field equation. The technique takes advantage of the fact that the Fourier transform of a function's derivative is related to the Fourier transform of the original function. For example, if  $f(z)$  has as its Fourier transform  $F(u)$

$$F(u) = \int_{-\infty}^{\infty} f(z) \exp(2\pi iuz) dz,$$

then the Fourier transform of  $df(z)/dz$  is  $2\pi iuF(u)$

$$2\pi iuF(u) = \int_{-\infty}^{\infty} \frac{df(z)}{dz} \exp(2\pi iuz) dz.$$

At each integration step the spatial distribution of the electric field is Fourier transformed and each spatial-frequency component is multiplied by  $2\pi i$  times its frequency; the resulting function is inverse-Fourier transformed to generate the spatial derivative of the electric field. Using the fast Fourier transform algorithm makes the technique especially efficient. For  $2M$  spatial points of the electric field, there are  $M+1$  spatial modes of the electric field. At each spatial point there are five variables (the two quadratures of the electric field and polarization and the inversion). Therefore, a laser with  $M+1$  modes is represented by  $10M$  variables. Using this technique Hillman and Koch<sup>28</sup> discovered that the multimode Maxwell-Bloch equations have two classes of solution. In one class of solutions, the atomic polarization and electric field are either always positive or always negative. In the second class of solutions, the polarization and electric field oscillate both positive and negative. In this class, the central component of the field spectrum is suppressed, and the field spectrum is predominantly made up of two frequency components. The solution however, does not seem to be stable below nine times above threshold. Numerical calculations by Lugiato *et al.*<sup>29</sup>, also discovered the two classes of solutions. The authors point out that,

in numerical simulations, the single-mode solution destabilizes into the solution where the polarization and electric field are either always positive or always negative. They found that the class of solutions where the polarization and electric field oscillate both positive and negative could be reached only when large perturbations were added to the system. They too could not theoretically reproduce the discontinuous intensity jumps nor the low threshold observed in experiments. Both groups did produce solutions whose spectra were nearly two-frequency and whose frequency separation increased linearly with increasing field strength.

Since the frequency separation of the field components in the experiment and the two-level theory both indicate that the instability is associated with Rabi oscillations, one might not expect a theory that accounts for the structure of the lower level of the dye molecule to predict the instability. For instance, consider a single excited state that decays to a band of lower levels with an energy decay rate  $1/T_1$ . Quantum electrodynamics tells us that

$$\begin{aligned} \frac{1}{T_1} &= \frac{4\omega^3}{3\hbar c^3} \sum_n |\mu_n|^2, \\ &= \frac{4\omega^3 |\mu_0|^2}{3\hbar c^3} \quad \text{where} \quad |\mu_0|^2 = \sum_n |\mu_n|^2, \end{aligned}$$

$\mu_n$  is the dipole moment matrix element between the excited state and the  $n^{\text{th}}$  level in the band, and  $\omega$  is the transition frequency. The sum over  $n$  contains all the levels that are optically connected to the excited state. The second equation illustrates that the effective dipole moment,  $|\mu_0|$  for a transition to a single level is larger than the individual dipole moments of the transitions into the band,  $|\mu_n|$ . The dipole moment between the excited state and an effective lower level cannot be larger than  $|\mu_0|$ .

We have measured 100 Watts of optical power circulating in the dye laser cavity. The radius of the focal spot at the active region of the dye laser is  $10 \mu\text{m}$ .



This produces intensities on the order of 50 MWatts/cm<sup>2</sup>. This corresponds to a Rabi frequency of approximately  $10^{13}$  sec<sup>-1</sup>. The corresponding wavelength separation for this Rabi frequency is approximately 20 Å. Therefore the measured spectral splittings of 340 Å cannot be attributed to the Rabi frequency. However, since the splitting is proportional to the square root of the intensity, the Rabi frequency appears to be a subharmonic of the spectral splitting. Fu and Haken<sup>39-41</sup> and Mashkevich<sup>42</sup> have shown that many of the experimental signatures can be reproduced theoretically by a band model of the dye molecule. The physical mechanism responsible for the instability remains to be discovered, it does not appear to be Rabi oscillations as in the conventional two-level atom.

## 2. The Band Model

Dye molecules have an energy level structure that consists of a ground electronic state and a series of excited electronic states. The excited electronic states are separated into two different parities: singlet states and triplet states. In the singlet states, the excited electron's spin is antialigned with the spin of the vacancy in the ground electronic state. In the triplet state, the excited electron's spin is aligned with the spin of the vacancy, and is therefore forbidden to make an electronic dipole transition. Since the dye molecule is not a rigid structure, it has the ability to vibrate and oscillate in its attempt to come to equilibrium with its environment and itself. This vibrational motion produces a manifold of vibrational and rotational energy levels on each of the electronic states.<sup>64</sup> To a first order of approximation these energy levels can be thought of as simple harmonic oscillator energy levels. There are, however, a number of different modes that the dye molecule can vibrate, and therefore there are a number of harmonic oscillator energy levels superimposed on each other. A

simple example of different vibrational modes of a molecule are the three different modes of a  $\text{CO}_2$  molecule: symmetric stretch, asymmetric stretch, and bend modes.<sup>85</sup> It is not difficult to see that a dye molecule, which is much more complicated than a  $\text{CO}_2$  molecule, has many different modes and is not merely a simple harmonic oscillator. The dye molecules relaxation dynamics in these vibrational manifolds is a topic of current research interest. There are three basic types of relaxation mechanisms in these manifolds. The first mechanism involves the redistribution of the energy throughout the manifold of levels. Statistical mechanics tells us the distribution of energy in the levels should approach a Boltzmann distribution in the steady state. The second relaxation mechanism involves the loss of energy to the solvent molecules that host the dye molecules. One theory<sup>86</sup> models the collision of the dye molecule with the solvent molecule as a short-lived molecule made of a solvent and solute molecule; the energy in the solvent-solute molecule attempts to reach equilibrium, typically this involves vibrational energy in the dye molecule transported to the solvent molecule. When the solvent-solute molecule breaks apart, the solvent molecule retains some of the dye molecule's vibrational energy. The third relaxation mechanism of the dye molecule is associated with the solvent molecules rearranging themselves around the dye molecule when the dye molecule makes an electronic transition. The electronic transitions take place much faster than any other rate in the system. So, as far as the solvent molecules are concerned, during an electronic transition the electronic wave function associated with the ground state changes immediately to the electronic wave function of the excited state. The solvent molecules readjust themselves around the dye molecule in a process called solvation.<sup>84</sup> This process decreases the energy of the molecule.

These relaxation times are much larger than the time an optical transition

takes place. However, they are much smaller than many of the other characteristic times in the system. With these thoughts in mind, we now begin discussion of the band model. A diagram of the energy level structure is illustrated in Fig. (5.1). The model assumes a single upper atomic state is connected to a band of  $2N + 1$  lower levels. The upper state is the metastable level of the vibrational manifold of the excited electronic state. The band of lower levels represents the levels of the vibrational manifold of the ground electronic state.

Another level,  $g$ , is assumed to be the lowest of the ground electronic state's vibrational manifold. We assume that the optical dipole moment between this absolute ground state and the metastable excited state is zero. In reality it is not zero though small due to the fact that the absorption and emission bands of rhodamine-6G do not significantly overlap. We can use Heisenberg's equation of motion to calculate the equations of motion for this system. The Hamiltonian of the system,  $\hat{H}$  \* is given by the sum of the atomic energies plus the interaction Hamiltonian

$$\hat{H} = \hbar\omega_e \hat{\sigma}_{ee} + \sum_{n=-N}^N \hbar\omega_n \hat{\sigma}_{nn} - \hat{\mu}E, \quad (5.1)$$

where  $\hat{\sigma}_{ee}$  is the projection operator for the excited state population,  $\hat{\sigma}_{nn}$  is the projection operator for the  $n^{\text{th}}$  lower-state population,  $\hbar\omega_e$  ( $\hbar\omega_n$ ) is the energy of the excited ( $n^{\text{th}}$  lower) state,  $E = \mathcal{E} \exp(i\omega t) + \mathcal{E}^* \exp(-i\omega t)$  is the amplitude of the laser field, and  $\hat{\mu}$  is the dipole moment operator of the atom. The dipole moment operator can be written in terms of the projection operators,  $\hat{\sigma}_{jj}$

$$\begin{aligned} \hat{\mu} &= \sum_j \sum_k \hat{\sigma}_{jj} \hat{\mu}_{jk} \hat{\sigma}_{kk}, \\ &= \sum_j \sum_k \mu_{jk} \hat{\sigma}_{jk}, \end{aligned}$$

---

\* Quantum mechanical operators are designated by a carat.

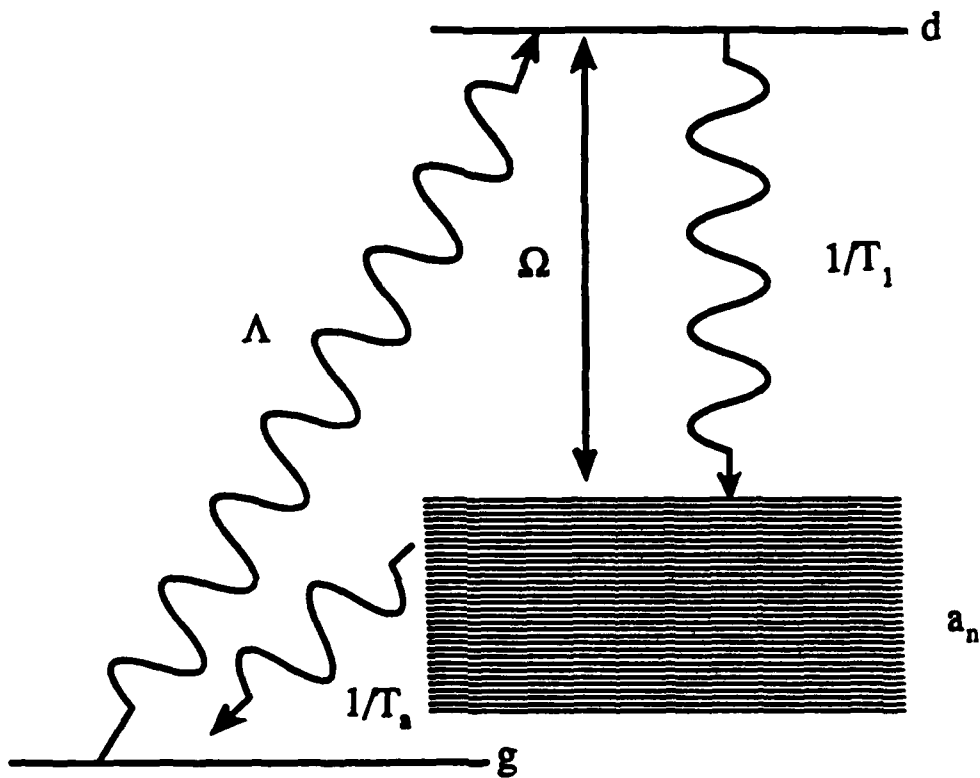


Fig. 5.1 Energy level diagram for the band model atom. The population is incoherently pumped at a rate  $\Lambda$  from the ground level  $g$  to the excited level  $d$ . The population  $d$  spontaneously decays to the band at a rate  $1/T_1$ . The population  $a_n$  in the band decays to the ground level at a rate  $1/T_a$ .

$$= \sum_{n=-N}^N (\mu_n \hat{\sigma}_{en} + \mu_n^* \hat{\sigma}_{ne}), \quad (5.2)$$

where the sums over  $j$  and  $k$  contain all atomic levels and  $\mu_n = \langle n | \hat{\mu} | e \rangle$  is the expectation value of the dipole operator between the excited state and the  $n^{\text{th}}$  level of the band. The Hamiltonian of the band level atom becomes

$$\hat{H} = \hbar\omega_e \hat{\sigma}_{ee} + \sum_{n=-N}^N \hbar\omega_n \hat{\sigma}_{nn} - \sum_{n=-N}^N (\mu_n^* \hat{\sigma}_{ne} + \mu_n \hat{\sigma}_{en}) E. \quad (5.3)$$

The equation of motion for an arbitrary quantum mechanical operator,  $\hat{O}$  is

$$\dot{\hat{O}} = -\frac{i}{\hbar} [\hat{O}, \hat{H}]. \quad (5.4)$$

We generate a closed set of differential equations to describe the band-level atom

$$\dot{\hat{\sigma}}_{ee} = -\frac{i}{\hbar} \sum_{n=-N}^N (\mu_n^* \hat{\sigma}_{ne} - \mu_n \hat{\sigma}_{en}) E, \quad (5.5a)$$

$$\dot{\hat{\sigma}}_{nn} = \frac{i}{\hbar} (\mu_n^* \hat{\sigma}_{ne} - \mu_n \hat{\sigma}_{en}) E, \quad (5.5b)$$

$$\dot{\hat{\sigma}}_{en} = i(\omega_e - \omega_n) \hat{\sigma}_{en} + \frac{i}{\hbar} \mu_n^* (\hat{\sigma}_{ee} - \hat{\sigma}_{nn}) E - \frac{i}{\hbar} \sum_{\substack{m=-N \\ m \neq n}}^N \mu_m^* \hat{\sigma}_{mn} E, \quad (5.5c)$$

$$\dot{\hat{\sigma}}_{ne} = \dot{\hat{\sigma}}_{en}^\dagger, \quad (5.5d)$$

$$\dot{\hat{\sigma}}_{mn} = i(\omega_m - \omega_n) \hat{\sigma}_{mn} - \frac{i}{\hbar} (\mu_m \hat{\sigma}_{en} - \mu_n^* \hat{\sigma}_{me}) E, \quad (5.5e)$$

where  $\dagger$  denotes the Hermitian conjugate.

The operators representing the populations,  $\hat{\sigma}_{nn}$  and  $\hat{\sigma}_{ee}$  are slowly varying quantities; in the absence of an applied field, the operators representing the dipole moments,  $\hat{\sigma}_{ne}$  and  $\hat{\sigma}_{en}$ , oscillate at the optical transition frequency ( $\omega_e - \omega_n$ ). We use this information to define a slowly varying operator

$$\hat{s}_n \equiv \hat{\sigma}_{en} \exp(-i\omega t) \quad (5.6)$$

Using this definition and applying the rotating-wave approximation we obtain

$$\dot{\hat{\sigma}}_{ee} = -\frac{i}{\hbar} \sum_{n=-N}^N (\mu_n^* \hat{s}_n^\dagger \mathcal{E} - \mu_n \hat{s}_n \mathcal{E}^*), \quad (5.7a)$$

$$\dot{\hat{\sigma}}_{nn} = \frac{i}{\hbar} (\mu_n^* \hat{s}_n^\dagger \mathcal{E} - \mu_n \hat{s}_n \mathcal{E}^*), \quad (5.7b)$$

$$\dot{\hat{s}}_n = -i\Delta_n \hat{s}_n + \frac{i}{\hbar} \mu_n^* (\hat{\sigma}_{ee} - \hat{\sigma}_{nn}) \mathcal{E} - \frac{i}{\hbar} \sum_{\substack{m=-N \\ m \neq n}}^N \mu_m^* \hat{\sigma}_{mn} \mathcal{E}, \quad (5.7c)$$

$$\dot{\hat{\sigma}}_{mn} = i(\omega_m - \omega_n) \hat{\sigma}_{mn} - \frac{i}{\hbar} (\mu_m \hat{s}_n \mathcal{E}^* - \mu_n^* \hat{s}_m^\dagger \mathcal{E}). \quad (5.7d)$$

These equations represent the coherent interaction of the single upper level and a band of lower levels with a semiclassical electric field.

We are now interested in using the operator equations, Eqns. (5.7) to generate equations of motion for the average values of a homogeneous sample of atoms. The first step in the averaging process involves taking the quantum mechanical average of the operators. After this point we deal strictly with complex numbers (c-numbers) representing the atomic variables of the system

$$p_n = \frac{\mu_n}{\mu_0} \langle \hat{s}_n \rangle, \quad (5.8a)$$

$$a_n = \langle \hat{\sigma}_{nn} \rangle, \quad (5.8b)$$

$$c_{mn} = \frac{\mu_n \mu_m^*}{|\mu_0|^2} \langle \hat{\sigma}_{mn} \rangle, \quad (5.8c)$$

$$d = \langle \hat{\sigma}_{ee} \rangle, \quad (5.8d)$$

$$\Omega = i\mu_0^* \mathcal{E} / \hbar. \quad (5.8e)$$

where  $|\mu_n|^2 = f_n |\mu_0|^2$  and  $f_n$  is the oscillator strength of the transition between the excited state and the  $n^{\text{th}}$  level of the lower band. In addition to the quantum mechanical average, we also wish to account for the incoherent processes such as spontaneous emission, dipole dephasing collisions, and incoherent pump processes. We account for these processes by phenomenologically adding rates

to the differential equations describing the c-number quantities. Figure (5.1) shows the incoherent transition rates as wavy lines. These give us the set of differential equations

$$\dot{p}_n = - \left( i\Delta_n + \frac{1}{T_2} \right) p_n + f_n(d - a_n)\Omega - \sum_{\substack{m=-N \\ m \neq n}}^N c_{mn}\Omega, \quad (5.9a)$$

$$\dot{a}_n = -a_n/T_a + f_n d/T_1 + (p_n^* \Omega + p_n \Omega^*), \quad (5.9b)$$

$$\dot{c}_{mn} = - \left[ \frac{1}{T_c} - i(\omega_m - \omega_n) \right] c_{mn} + (f_m p_n \Omega^* + f_n p_m^* \Omega), \quad (5.9c)$$

$$\dot{d} = - \sum_{n=-N}^N (p_n^* \Omega + p_n \Omega^*) - d/T_1 + \Lambda \left( 1 - d - \sum_{n=-N}^N a_n \right), \quad (5.9d)$$

where  $T_2$  is the decay time of the polarization,  $T_c$  is the decay time of the elements  $c_{mn}$ ,  $T_1$  is the energy decay time of the excited state population,  $T_a$  is the energy decay time of the levels of the band (assumed to be the same over the entire band),  $\Lambda$  is the rate population is pumped from the ground level to the excited state, and  $f_n$  is the oscillator strength for the transition from the excited state to the  $n^{\text{th}}$  level of the band. The decay rate from the excited state into the  $n^{\text{th}}$  level of the band is proportional to the oscillator strength  $f_n$ . The oscillator strengths are subject to the normalization condition

$$\sum_{n=-N}^N f_n = 1. \quad (5.10)$$

This model does not account for the fact that the lower levels of the rhodamine-6G molecule will be coupled to one another and that they may decay at different rates. The assumption that they decay directly to the ground level at the same rate and are not coupled to one another is a first-order approximation. More detailed analysis of the rhodamine-6G dye molecule structure can be found in reference 84.

The dye molecule is a complicated organic molecule whose molecular weight is between 480 and 560, depending on the salt attached to it. This large molecule has an enormous density of states available for its intra-atomic relaxation. As a consequence of this large density of states, the decay rate of the lower-state variables can be much faster than any other rate in the system. We assume the elements  $c_{mn}$  decay sufficiently faster than any other rate in the system, so that we can set  $c_{mn}$  to zero. This assumption leaves us with the atomic equations of motion for the band model

$$\dot{p}_n = - \left( i\Delta_n + \frac{1}{T_2} \right) p_n + f_n(d - a_n)\Omega, \quad (5.11a)$$

$$\dot{a}_n = -a_n/T_a + f_n d/T_1 + (p_n^* \Omega + p_n \Omega^*), \quad (5.11b)$$

$$\dot{d} = - \sum_{n=-N}^N (p_n^* \Omega + p_n \Omega^*) - d/T_1 + \Lambda \left( 1 - d - \sum_{n=-N}^N a_n \right), \quad (5.11c)$$

The field equation is similar to the field equation of the MMMBE. The macroscopic polarization,  $P$  that drives the wave equation is

$$P = \mathcal{N} \langle \hat{\mu} \rangle = \mathcal{N} \sum_{n=-N}^N [\mu_0 p_n \exp(i\omega t) + \mu_0^* p_n^* \exp(-i\omega t)],$$

which gives us the field equation

$$\dot{\Omega} = \frac{1}{2\tau_c} \left[ g \sum_{n=-N}^N p_n - \Omega \right] - c \frac{\partial}{\partial z} \Omega, \quad (5.12)$$

where  $g = \frac{4\pi\mathcal{N}|\mu_0|^2\omega\tau_c}{\hbar}$  and  $\mathcal{N}$  is the atomic number density of the gain medium.

### 3. Single-Frequency Steady State Solutions

We define the steady state solutions to band model equations as

$$\lim_{t \rightarrow \infty} \begin{bmatrix} p_n \\ a_n \\ d \\ \Omega \end{bmatrix} = \begin{bmatrix} p_n(0) \\ a_n(0) \\ d(0) \\ \Omega(0) \end{bmatrix}.$$



The polarization equation, Eqn. (5.11a) tells us the steady state polarization is proportional to the steady state field strength and the inversion between the excited state and the  $n^{\text{th}}$  lower level

$$p_n(0) = \frac{f_n [d(0) - a_n(0)] \Omega(0) T_2}{1 + i\Delta_n T_2}. \quad (5.13)$$

We use this in the equation for the lower-state population, Eqn. (5.11b) to obtain

$$a_n(0) = f_n \frac{T_a}{T_1} \left[ d(0) + \frac{2[d(0) - a_n(0)] |\Omega(0)|^2 T_2 T_1}{1 + (\Delta_n T_2)^2} \right],$$

or solving for  $a_n(0)$  explicitly

$$a_n(0) = r_a f_n \frac{1 + (\Delta_n T_2)^2 + I(0)}{1 + (\Delta_n T_2)^2 + r_a f_n I(0)} d(0), \quad (5.14)$$

where we introduce the dimensionless intensity, (similar to the two-level atom dimensionless intensity),  $I(0) = 2|\Omega(0)|^2 T_1 T_2$  and the ratio  $r_a = T_a/T_1$ . Using this we can write the steady state inversion between the excited state and the  $n^{\text{th}}$  lower level as

$$d(0) - a_n(0) = \frac{[1 - r_a f_n] [1 + (\Delta_n T_2)^2]}{1 + (\Delta_n T_2)^2 + r_a f_n I(0)} d(0). \quad (5.15)$$

Using this expression for the inversion, Eqn. (5.15), we can rewrite the steady state polarization, Eqn. (5.13), as

$$p_n(0) = \frac{f_n (1 - r_a f_n) (1 - i\Delta_n T_2)}{1 + (\Delta_n T_2)^2 + r_a f_n I(0)} d(0) \Omega(0) T_2. \quad (5.16)$$

The field equation, Eqn. (5.12), tells us that the steady state field amplitude is directly proportional to the sum of the steady state polarizations

$$\Omega(0) = g \sum_{n=-N}^N p_n(0) \quad (5.17)$$

Using the expression for the steady state polarization, Eqn. (5.16), in the expression for the steady state field strength, Eqn. (5.17), we obtain

$$d(0) g \sum_{n=-N}^N \frac{f_n(1 - r_a f_n) T_2 (1 - i \Delta_n T_2)}{1 + (\Delta_n T_2)^2 + r_a f_n I(0)} = 1. \quad (5.18)$$

Equating the real parts of this expression gives us

$$d(0) = \left[ g \sum_{n=-N}^N \frac{f_n(1 - r_a f_n) T_2}{1 + (\Delta_n T_2)^2 + r_a f_n I(0)} \right]^{-1}. \quad (5.19)$$

This equation gives the relationship between the steady state excited state population and the steady state intensity. If we sum the steady state equation for the lower level population and use Eqn. (5.17) for the sum of the polarizations, we obtain the total population in the lower band

$$\sum_{n=-N}^N a_n = r_a \left[ d(0) + \frac{I(0)}{g T_2} \right]. \quad (5.20)$$

We can see from Eqn. (5.19) and Eqn. (5.20), that neither the inversion between the excited state and the  $n^{\text{th}}$  lower level nor the inversion between the excited state and the total population of the lower band is a constant of the motion, as is the case in the simple two-level laser theory. That is, inversion clamping is not predicted by the band model theory. This prediction is tested in an experiment discussed later in Chapter VI. Finally, using the equation for the excited state population, Eqn. (5.11c) in steady state we obtain

$$\Lambda T_1 = \left[ d(0) + \frac{I(0)}{g T_2} \right] \left[ 1 - d(0) - \sum_{n=-N}^N a_n(0) \right]^{-1}. \quad (5.21)$$

The pump parameter,  $\Lambda$ , is the independent variable of the system. It controls all the other variables. Normally, one chooses  $\Lambda$  and determines the remaining variables of the system. However, attempting to solve for the steady state solutions of the band model in this way, results in transcendental equations for

the system variables. To obtain the steady state solutions of the band model it is much more convenient to choose a field strength, then using Eqn. (5.19), determine the corresponding excited state population. Finally, using these values for the excited state population and the field strength, determine the necessary pump parameter using Eqn. (5.20). Using this method, we can determine the steady state system response for a number of pump intensities.

#### 4. Continuum Limit

Since the fluorescence and gain of the dye molecule show no structure due to the lower state of the dye molecule, we will treat the band as a continuum. This is accomplished by letting  $N$ , the number of levels in the analysis, approach infinity. We assume the levels are equally spaced in the band. In the discrete case the detuning takes the form

$$\Delta_n = n \frac{\zeta}{N} \quad \text{where} \quad -N \leq n \leq N,$$

and  $2\zeta$  is the width of the band. In the continuum limit, the discrete sums are converted to integrals

$$\lim_{N \rightarrow \infty} \sum_{n=-N}^N \rightarrow \int_{-\zeta}^{\zeta} \rho(x) dx,$$

where  $\rho(x)$  is the density of states in the band, which we will take to be uniformly distributed over the band (i.e.,  $\rho(x) = \frac{1}{2\zeta}$ ). The detuning in the continuum limit becomes

$$\lim_{N \rightarrow \infty} \Delta_n \rightarrow x,$$

and the oscillator strength becomes a function of  $x$

$$\lim_{N \rightarrow \infty} f_n \rightarrow f(x).$$

We consider two forms for the oscillator strength: a Lorentzian distribution,  $f(x) = \frac{A}{1 + (xT_f)^2}$  and a flat oscillator strength  $f_n = 1$ . The width of the Lorentzian profile of the oscillator strength is given by  $1/T_f$ . We determine the parameter  $A$  using the normalization condition for the oscillator strength, Eqn. (5.10)

$$\begin{aligned} \frac{1}{2\zeta} \int_{-\zeta}^{\zeta} f(x) dx &= \frac{1}{2\zeta} \int_{-\zeta}^{\zeta} \frac{A}{1 + (xT_f)^2} dx = 1, \\ \Rightarrow A &= \frac{\zeta T_f}{\tan^{-1}(\zeta T_f)} \end{aligned} \quad (5.22)$$

Equation (5.19), which relates the steady state excited state population to the steady state field strength, becomes

$$d(0) = \left[ \frac{g}{2\zeta} \int_{-\zeta}^{\zeta} \frac{f(x)[1 - r_a f(x)] T_2}{1 + (xT_2)^2 + r_a f(x) I(0)} dx \right]^{-1}, \quad (5.23)$$

and the pump parameter, Eqn. (5.20) becomes

$$\Lambda T_1 = \left[ d(0) + \frac{I(0)}{g T_2} \right] \left[ 1 - d(0) - \int_{-\zeta}^{\zeta} a(x) dx \right]^{-1}. \quad (5.24)$$

## 5. Lorentzian and Flat Oscillator Strength

For the flat oscillator strength we can evaluate Eqn. (5.23)

$$d(0) = \left\{ \frac{g}{\zeta} \frac{1 - r_a}{\sqrt{1 + r_a I(0)}} \tan^{-1} \left[ \frac{\zeta T_2}{\sqrt{1 + r_a I(0)}} \right] \right\}^{-1}. \quad (5.26)$$

Since  $d(0)$  represents the population in the excited state, it must be a non-negative number. From Eqn. (55), we can see this implies that  $r_a \leq 1$  for a valid steady state solution to exist in the continuum limit with a flat oscillator strength. That is, the population decay time of the band must be shorter than the population decay time of the excited state,  $T_a \leq T_1$ . This relation also

emerges from a simple four-level analysis of a laser. We plot  $d(0)$  and  $\Omega(0)$  as a function of the pump parameter  $\Lambda$  for various values of the ratio  $r_a$  and for  $\zeta T_2 = 1$ , and  $gT_2 = 10^3$ . We also plot the total inversion as a function the pump parameter to demonstrate that the inversion does not clamp in a band model laser. Figure (5.2) shows the excited state population of the band model as a function of the pump parameter,  $\Lambda$ . Figure (5.3) shows the nearly linear dependence of the dimensionless intensity of the dye laser as a function of the pump parameter. Figure (5.4) shows the total inversion of the band molecule,  $d(0) - \sum_{n=-N}^N a_n(0)$  as a function of the pump parameter. This figure illustrates the fact that the inversion in the band model does not clamp at threshold as is predicted in two- and three-level laser theory.

For the case of the Lorentzian profile of the oscillator strength, we find that the inverse of the excited state population in the continuum limit is

$$\begin{aligned}
 d(0)^{-1} = & \frac{gA}{\zeta} \left[ \frac{1}{(z_- - z_+)} + \frac{r_a A (1 - r_f^2 z_-)}{r_f^2 \mathcal{D}} \right] \left[ \frac{1}{\sqrt{z_+}} \tan^{-1} \left( \frac{\zeta T_2}{\sqrt{z_+}} \right) \right] \\
 & - \left[ \frac{1}{(z_- - z_+)} + \frac{r_a A (1 - r_f^2 z_+)}{r_f^2 \mathcal{D}} \right] \left[ \frac{1}{\sqrt{z_-}} \tan^{-1} \left( \frac{\zeta T_2}{\sqrt{z_-}} \right) \right] \\
 & - \frac{r_a A}{r_f \mathcal{D}} (z_+ - z_-) \tan^{-1}(\zeta T_2 r_f), \tag{5.26}
 \end{aligned}$$

where  $r_f = T_f/T_2$ ,

$$z_{\pm} = \frac{1 + r_f^2 \pm \sqrt{(1 - r_f^2)^2 - 4r_f^2 r_a A I(0)}}{2r_f^2}, \tag{5.27}$$

and

$$\mathcal{D} = (z_+ - z_-)z_+z_- + \left( \frac{1}{r_f^2} - z_- \right) \frac{z_-}{r_f^2} + \left( \frac{1}{r_f^2} - z_+ \right) \frac{z_+}{r_f^2}. \tag{5.28}$$

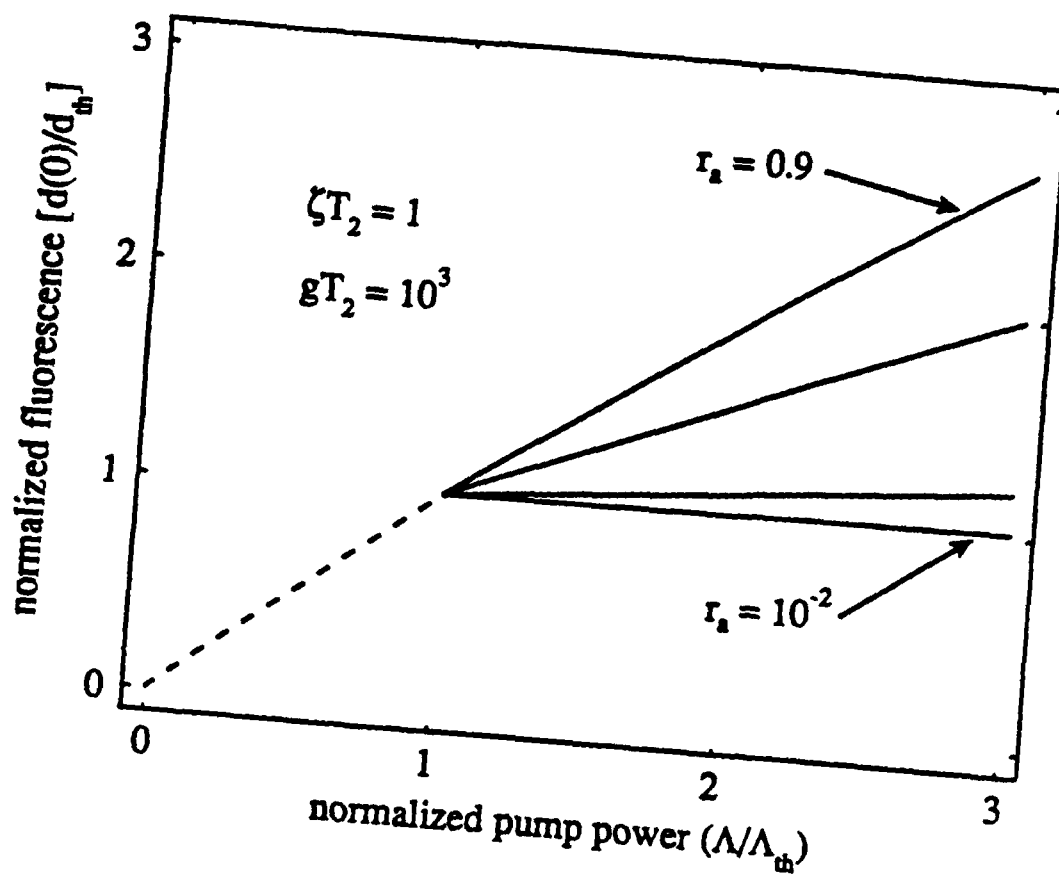


Fig. 5.2 Excited state population as a function of pump parameter in the continuum limit of the band model for the flat-oscillator-strength approximation. The dotted line is to indicate that below threshold the fluorescence starts at zero for zero pump energy.  $r_a = 10^{-2}$ , 0.1, 0.5, and 0.9.

### 6. Two-Frequency Stationary State Solution

We know from the experiments that two-frequency solutions to the laser equations exist for a dye laser. We attempt to verify their existence theoretically by writing a multi-frequency solution to the band-level equations. We assume the self-consistent solution can be written in a form

$$p_n = \sum_{k=-\infty}^{\infty} p_n(2k+1) \exp [i(2k+1)\delta\omega(t-z/c)], \quad (5.29a)$$

$$a_n = \sum_{k=-\infty}^{\infty} a_n(2k) \exp [i2k\delta\omega(t-z/c)], \quad (5.29b)$$

$$d = \sum_{k=-\infty}^{\infty} d(2k) \exp [i2k\delta\omega(t-z/c)], \quad (5.29c)$$

$$\Omega = \sum_{k=-\infty}^{\infty} \Omega(2k+1) \exp [i(2k+1)\delta\omega(t-z/c)]. \quad (5.29d)$$

In the experiments, the frequency separation of the field components,  $\delta\omega \approx 10^{14} \text{ sec}^{-1}$ . We therefore neglect terms proportional to  $\delta\omega T_a$  and  $\delta\omega T_1$ . This allows us to find a self-consistent solution while truncating the series in Eqns. (5.29)

$$p_n = p_n(1) \exp [i\delta\omega(t-z/c)] + p_n(-1) \exp [-i\delta\omega(t-z/c)], \quad (5.30a)$$

$$a_n = a_n(0), \quad (5.30b)$$

$$d = d(0), \quad (5.30c)$$

$$\Omega = \Omega(1) \exp [i\delta\omega(t-z/c)] + \Omega(-1) \exp [-i\delta\omega(t-z/c)]. \quad (5.30d)$$

Substituting Eqns. (5.30) into Eqns. (5.11) and Eqn. (5.12) we can obtain a closed set of equations for the amplitudes  $p_n(\pm 1)$ ,  $a_n(0)$ ,  $d(0)$ , and  $\Omega(\pm 1)$ , and the frequency  $\delta\omega$ . From the polarization equation, Eqn. (5.11a) we obtain

$$p_n(\pm 1) = \frac{f_n [d(0) - a_n(0)] \Omega(\pm 1) T_2}{1 + i(\Delta_n \pm \delta\omega) T_2}. \quad (5.31)$$

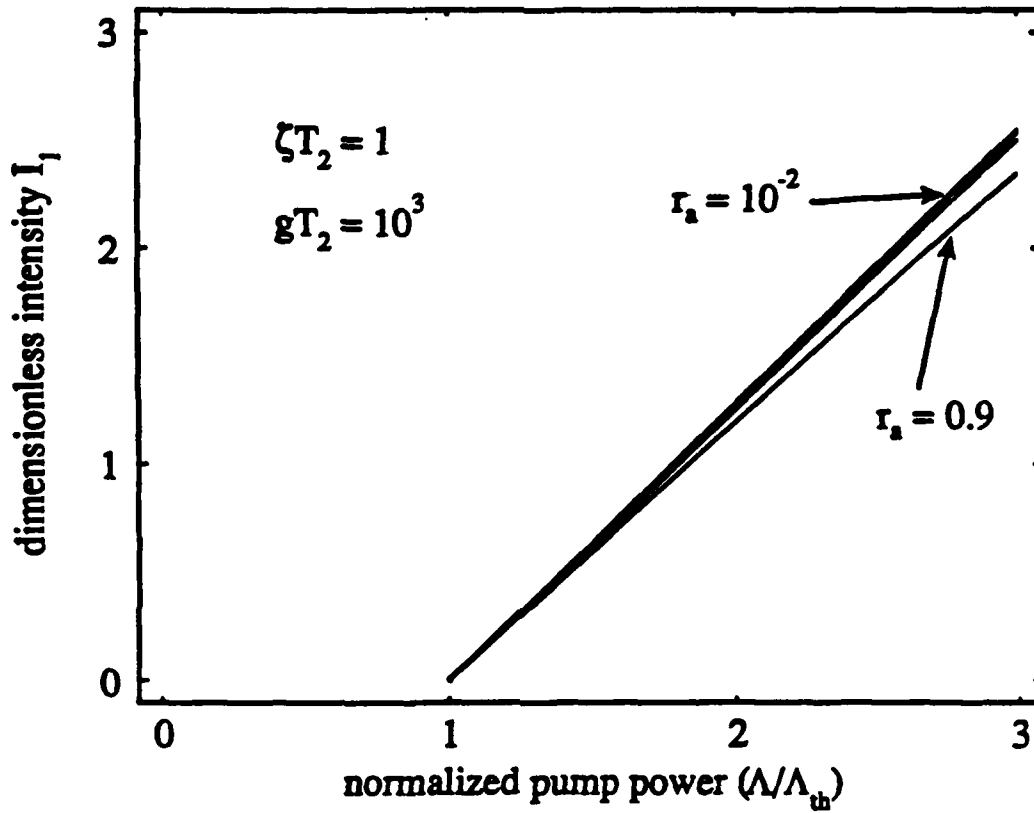


Fig. 5.3 Dimensionless laser intensity as a function of pump parameter in the continuum limit of the band model for the flat-oscillator-strength approximation.  $r_s = 10^{-2}$ , 0.1, 0.5, and 0.9.



From the lower-level-population equation, Eqn. (5.12b), we obtain

$$a_n(0) = r_a f_n \frac{1 + \frac{I(1)}{1 + (\Delta_n + \delta\omega)^2 T_2^2} + \frac{I(-1)}{1 + (\Delta_n - \delta\omega)^2 T_2^2}}{1 + r_a f_n \frac{I(1)}{1 + (\Delta_n + \delta\omega)^2 T_2^2} + r_a f_n \frac{I(-1)}{1 + (\Delta_n - \delta\omega)^2 T_2^2}} d(0), \quad (5.32)$$

where  $I(\pm 1) = 2|\Omega(\pm 1)|^2 T_1 T_2$ . This expression for  $a_n(0)$  allows us to write the inversion between the excited state and the  $n^{\text{th}}$  lower level as

$$d(0) - a_n(0) = \frac{1 - r_a f_n}{1 + r_a f_n \frac{I(1)}{1 + (\Delta_n + \delta\omega)^2 T_2^2} + r_a f_n \frac{I(-1)}{1 + (\Delta_n - \delta\omega)^2 T_2^2}} d(0) \quad (5.33)$$

The field equation, Eqn. (5.12) gives us

$$\Omega(\pm 1) = g \sum_{n=-N}^N p_n(\pm 1). \quad (5.34)$$

Finally, the equation for the excited-state population, Eqn. (5.11c) gives

$$\Delta T_1 = \left[ d(0) + \frac{(I(1) + I(-1))}{g T_2} \right] \left[ 1 - d(0) - \sum_{n=-N}^N a_n(0) \right]^{-1}. \quad (5.35)$$

Since the equations for the field components,  $I(\pm 1)$  are symmetric, (due to the symmetry of the problem as we have constructed it), the two field components can be shown to be equal,  $I(1) = I(-1)$ . Using the expression for the inversion, Eqn. (5.33), in the polarization equation, Eqn. (5.31), we can rewrite the polarization as

$$p_n(\pm 1) = \frac{f_n(1 - r_a f_n)}{\left[ 1 + r_a f_n I(1) \left( \frac{1}{1 + (\Delta_n + \delta\omega)^2 T_2^2} + \frac{1}{1 + (\Delta_n - \delta\omega)^2 T_2^2} \right) \right]} \frac{d(0)\Omega(\pm 1)T_2}{[1 + i(\Delta_n \pm \delta\omega)T_2]}. \quad (5.36)$$

We use this expression in Eqn. (61) and obtain two equations by equating the real and imaginary parts of the resulting expression

$$g \sum_{n=-N}^N \frac{f_n(1 - r_a f_n)[1 + (\delta\omega T_2)^2 - 2\delta\omega T_2 \Delta_n T_2 + (\Delta_n T_2)^2]}{(\Delta_n T_2)^4 + 2(\Delta_n^2 T_2)(1 + r_a f_n I(1) - (\delta\omega T_2)^2) + [1 + (\delta\omega T_2)^2][1 + 2r_a f_n I(1) + (\delta\omega T_2)^2]} d(0) = 1, \quad (5.37a)$$

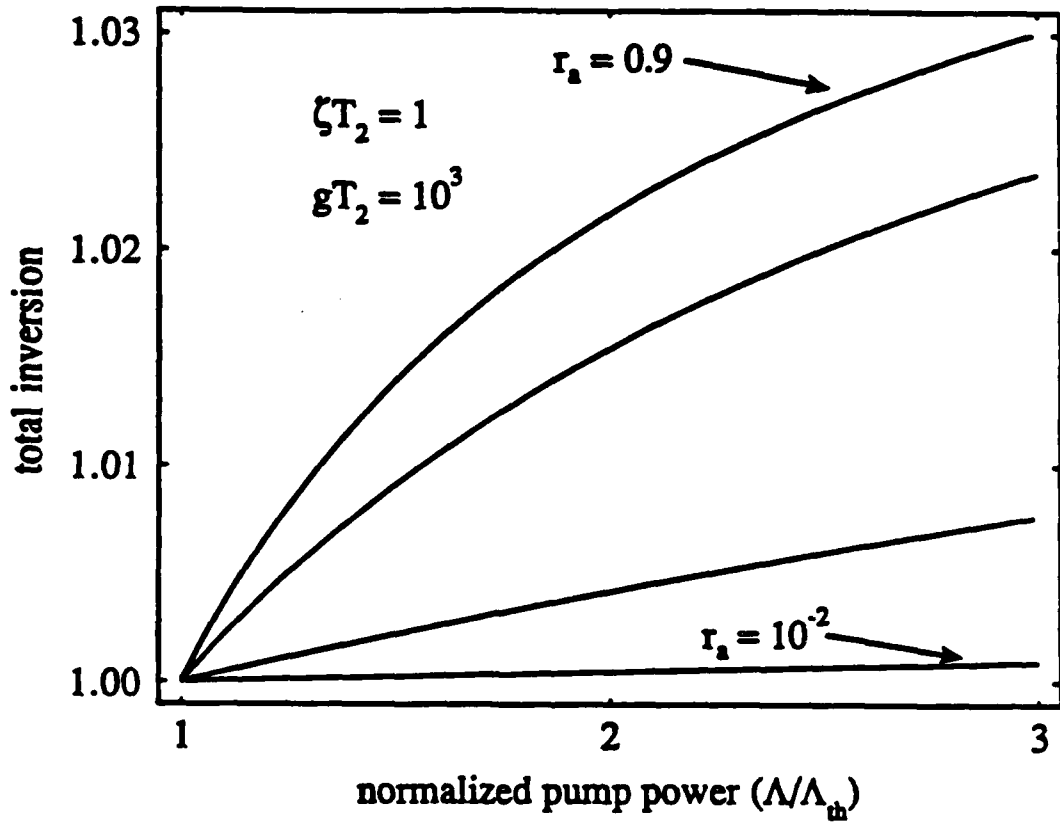


Fig. 5.4 Total inversion as a function of pump parameter in the continuum limit of the band model for the flat-oscillator-strength approximation. This Figure illustrates that the total inversion in the band model does not clamp. the total inversion is defined as the difference between the excited state population  $d$  and the total population of the band  $\int a(x)dx$ .  $r_a = 10^{-2}$ , 0.1, 0.5, and 0.9.

and

$$\sum_{n=-N}^N \frac{f_n(1-r_a f_n)[(\Delta_n T_2)^3 - (\Delta_n T_2)^2(\delta\omega T_2) + \Delta_n T_2(1 - (\delta\omega T_2)^2) + \delta\omega T_2(1 + (\delta\omega T_2)^2)]T_2}{(\Delta_n T_2)^4 + 2(\Delta_n^2 T_2)(1 + r_a f_n I(1) - (\delta\omega T_2)^2) + [1 + (\delta\omega T_2)^2][1 + 2r_a f_n I(1) + (\delta\omega T_2)^2]} = 0. \quad (5.37b)$$

These equations are solved by a method similar to the single frequency steady state solutions. We choose the frequency separation,  $\delta\omega$ , and then solve the transcendental equation, Eqn. (5.37b), for the intensity of the laser  $I(1)$ . The value of the excited state population is then determined using Eqn. (5.37a). Finally, the value of the pump parameter is determined from Eqn. (5.35).

## 7. Lorentzian and Flat Oscillator Strength

In the case where the oscillator strength is constant over the band, and we consider the equations in the continuum limit, we can evaluate the expressions for the excited state population

$$d(0) = \left\{ \frac{g(1-r_a)}{\zeta(y_- - y_+)} \left[ \frac{1 + (\delta\omega T_2)^2 - y_+}{\sqrt{y_+}} \tan^{-1} \left( \frac{\zeta T_2}{\sqrt{y_+}} \right) - \frac{1 + (\delta\omega T_2)^2 - y_-}{\sqrt{y_-}} \tan^{-1} \left( \frac{\zeta T_2}{\sqrt{y_-}} \right) \right] \right\}^{-1}, \quad (5.38)$$

where

$$y_{\pm} = 1 + r_a I(1) - (\delta\omega T_2)^2 \pm \sqrt{r_a^2 I(1)^2 - 4(\delta\omega T_2)^2(1 + r_a I(1))}.$$

and the total population in the band

$$\frac{1}{2\zeta} \int_{-\zeta}^{\zeta} a(x) dx = r_a \left( d(0) + \frac{2I(1)}{gT_2} \right). \quad (5.39)$$

The expression that gives the relationship between the frequency separation of the field components and the intensity of the field can also be evaluated to obtain

$$\frac{1 + (\delta\omega T_2)^2 + y_+}{\sqrt{y_+}} \tan^{-1} \left( \frac{\zeta T_2}{\sqrt{y_+}} \right) - \frac{1 + (\delta\omega T_2)^2 + y_-}{\sqrt{y_-}} \tan^{-1} \left( \frac{\zeta T_2}{\sqrt{y_-}} \right) = 0. \quad (5.40)$$

The expressions for the excited state population and the field strength for the case of a Lorentzian-shaped oscillator strength are complicated. It is easier to evaluate the expressions in integral form on the computer.

Fu and Haken<sup>39-41</sup> have carried out calculations similar to those presented here. However, the theory of Fu and Haken<sup>39-41</sup> does not account for the saturation of the ground-state population. In the experiments discussed earlier, the pump intensity can be many times the saturation intensity of the dye molecule. The differences between neglecting or including ground-state saturation in the dynamics is similar to the differences between two-level and four-level laser theory. When ground-state saturation is included, the threshold for instability occurs for higher pump powers than when ground-state saturation is neglected. In addition, the theory of Fu and Haken<sup>39-41</sup> assumes that the excited-state population does not decay into the band, but instead assumes that the excited state decays out of the atomic system. Considering that the quantum efficiencies of most dye molecules used in lasers are of the order of unity, this is not a very realistic assumption. However, the theory has reproduced a number of unexplained experimental signatures. So, while the model does not seem to represent a dye molecule in some aspects, it has been very successful at modeling other aspects of the dye molecule.

One of the predictions that the theory of Fu and Haken<sup>40</sup> makes, involves the fact that discontinuous intensity jumps and hysteresis loops were observed at the thresholds of the dye laser instability. Their theory does not predict discontinuous jumps unless the energy decay time of the lower band is slower than the energy decay time of the excited state. Since the energy decay time of the excited state is known to be 5 nsec, the theory of Fu and Haken<sup>40</sup> predicts there may be long-lived states in the lower band of the rhodamine 6G dye molecule.

We test this hypothesis experimentally using modulation spectroscopy. Modulation spectroscopy can measure "hidden" decay rates (i.e., nonradiative decay rates) since it measures the total population cycling rate of a system. Modulation spectroscopy has been used to measure decay rates in ruby, alexandrite, and fluorescein-doped boric-acid glass. In those studies, the absorption or amplification of modulation sidebands was measured as a function of the modulation frequency. In the limit of large modulation frequency, the sideband absorption/amplification approaches the absorption/amplification of the carrier. Therefore the disadvantage of this technique is that it is not a signal-limited detection scheme. An alternative method would be to measure the fluorescence at the modulation frequency. In the limit of large modulation frequency, the fluorescence at the modulation frequency goes to zero. This signal-limited detection scheme is used to investigate the existence of long-lived states in the lower band of the rhodamine 6G dye molecule. These experiments are discussed in the next Chapter.

## Chapter VI

### BAND MODEL EXPERIMENTS

#### 1. Introduction

In this chapter we discuss two experiments that we performed to investigate the predictions of the band model,<sup>39-41</sup> discussed in the previous Chapter. The first experiment examines the population inversion of the dye molecules in the dye laser. We measure the fluorescence from the dye molecules as a function of the pump power. We then compare the results of the experiment with the predictions of simple three-level laser theory and the predictions of the band model. The second experiment examines the lower-level energy-decay time of the dye molecule. We use modulation spectroscopy, in a new signal-limited fashion, to infer an upper bound of the lower-level energy-decay time. The results of this experiment have direct implications to conclusions of the band model.

The phenomenon of inversion clamping occurs in two-, three-, and four-level laser systems; the inversion of the atomic system remains at a constant value once the laser reaches threshold. Any additional pump energy beyond

the threshold pump energy does not increase the inversion of the system. The inversion is proportional to the gain in the steady state. If the gain of the laser increases, the laser field will grow until the gain saturates to the loss. If the gain of the laser decreases, the intensity of the field decreases until the gain reaches the loss. Therefore, the gain of the laser clamps to the loss. In the steady state the gain of the laser is proportional to the inversion, therefore the inversion of the laser also clamps. Inversion clamping has been observed experimentally in GaAs injection diode lasers<sup>87</sup>. The band model differs drastically from two-, three-, and four-level laser theory in that it does not predict inversion clamping. This is due to the fact that the gain is not directly proportional to the inversion of the laser transition. We monitor the excited state population by measuring the fluorescence from the active region of a dye laser as a function of pump power.

The experimental setup is sketched in Fig. (6.1). We pass an argon-ion laser beam (Coherent Innova-20) through an acousto-optic modulator (AOM) (IntraAction Model ADM40) to conveniently modulate the pump power delivered to the dye laser. The rf amplitude delivered to the AOM is modulated by a triangle wave at frequencies between 1 Hz and 1 kHz. This modulates the intensity transmitted through the AOM. The pump intensity is monitored using a beam splitter and photodiode. The fluorescence from the active region of the dye jet is collected with a 10 mm focal length lens. To insure that we are looking at the center of the pump focus, the image of the active region is spatially filtered with a pinhole. The filtered image is monitored by a second photodiode. A third photodiode measures the intensity of the dye laser output. The signals from the photodiodes are simultaneously digitized by two transient digitizers (Sony/Tektronix RTD-710), triggered by the same source. Triggering

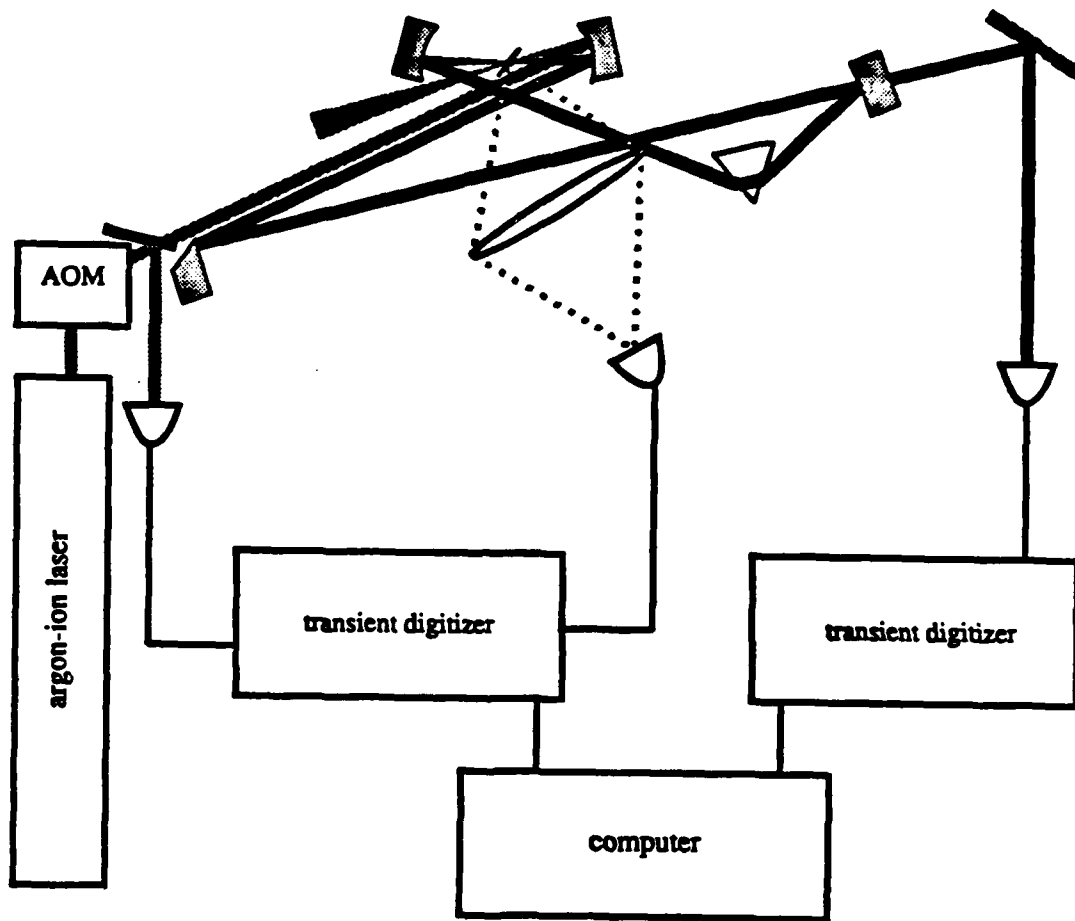


**Fig. 6.1** Experimental setup to observe the absence of inversion clamping in a cw pumped multimode dye laser. Two transient digitizers simultaneously collect the signals from the photodiodes measuring the intensity of the dye laser, the fluorescent intensity, and the pump intensity. The acousto-optic modulator (AOM) modulates the power of the pump laser delivered to the dye laser.



the two digitizers with the same source allows us to acquire all three samples simultaneously. The data is then transferred to a computer for further analysis.

We observe that the fluorescence from the active region of the dye laser continues to increase above threshold. To insure that we are monitoring molecules interacting with both the dye laser and the pump, we scan the image of the active region over the pinhole spatial filter. We observe no significant change in the slope of the curve above the laser threshold as the image of the active region is scanned across the spatial filter. We spectrally filter the fluorescence with a resolution of approximately 10 Å and find that the slope of the fluorescence versus pump power is independent of the wavelength of the fluorescence. The slope of the fluorescence is also independent of polarization. Since the dye molecules spend approximately 1 μsec in the active region and the dye molecules are reorienting themselves in a few nanoseconds, this result is not unexpected. The slope of the fluorescence as a function of pump power does change as the dye laser is tuned in wavelength.

## 2. Analysis and Results of Inversion Clamping

For the simple three-level system illustrated in Fig. (6.2) the equations of motion for a laser operating on resonance with the atomic system are

$$\dot{v} = -v/T_2 + \Omega w, \quad (6.1a)$$

$$\dot{w} = -\Omega v - \left( \Lambda + \frac{1}{T_1} - \frac{1}{2T_a} \right) w - \left( \frac{1}{T_1} + \frac{1}{2T_a} \right) w + \Lambda, \quad (6.1b)$$

$$\dot{n} = \frac{1}{2T_a} w - \left( \Lambda + \frac{1}{2T_a} \right) n + \Lambda, \quad (6.1c)$$

$$\dot{\Omega} = \frac{\alpha c}{2T_2} v - \frac{1}{2\tau_c} \Omega - c \frac{\partial}{\partial z} \Omega, \quad (6.1d)$$

where  $v$  is the in-quadrature part of the dipole moment,  $w$  is the inversion between the lasing levels, that is  $w = d - a$ , where  $d$  is the excited state population

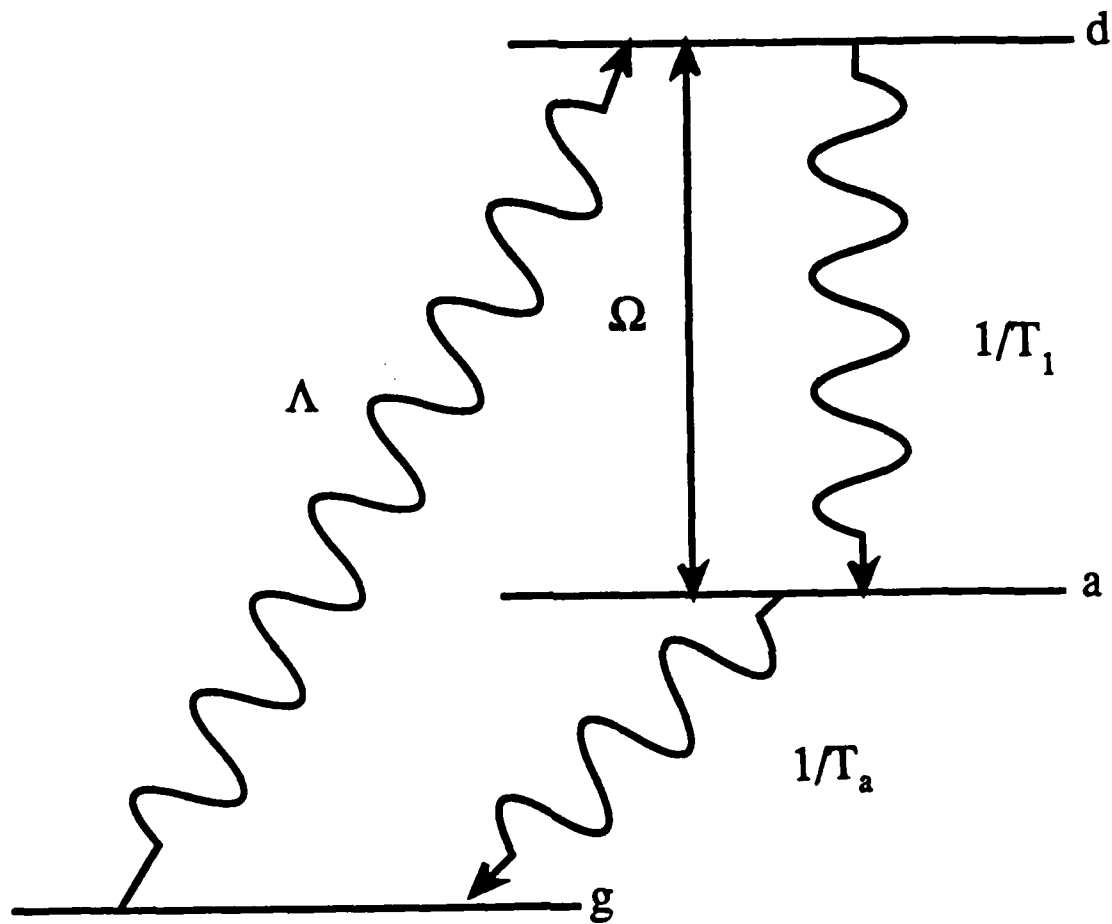


**Fig. 6.2** Energy level diagram for a three-level laser medium. The population in the ground level  $g$  is incoherently pumped at a rate  $\Lambda$  to the excited level. The population in the excited level  $d$  spontaneously decays to the lower level. The population in the lower level  $a$  decays to the ground level at a rate  $1/T_a$ .

and  $a$  is the lower state population. The total population in the laser active levels is  $n = d + a$ . All the other variables are as defined in previous Chapters. We define the steady state variables

$$\lim_{t \rightarrow \infty} \begin{bmatrix} v \\ w \\ n \\ \Omega \end{bmatrix} = \begin{bmatrix} v_0 \\ w_0 \\ n_0 \\ \Omega_0 \end{bmatrix}. \quad (6.2)$$

We find the steady state solutions

$$v_0 = \Omega_0 T_2 w_0, \quad (6.3a)$$

$$w_0 = (\alpha \tau_c)^{-1}, \quad (6.3b)$$

$$n_0 = \frac{2r_a \Lambda T_1 + w_0}{2r_a \Lambda T_1 + 1}, \quad (6.3c)$$

$$d_0 = \frac{1}{2}(n_0 + w_0) = \frac{r_a \Lambda T_1 + (1 + r_a \Lambda T_1)w_0}{2r_a \Lambda T_1 + 1}, \quad (6.3d)$$

$$a_0 = \frac{1}{2}(n_0 - w_0) = r_a \Lambda T_1 \frac{1 - w_0}{2r_a \Lambda T_1 + 1}, \quad (6.3e)$$

$$\frac{1}{2} \Omega_0^2 T_1 T_2 = \frac{\Lambda T_1 [(\alpha \tau_c - 1) - r_a (\alpha \tau_c + 1)] - 1}{2r_a \Lambda T_1 + 1}. \quad (6.3f)$$

The threshold pump power can be determined by setting the intensity to zero in Eqn. (6.3f). The threshold pump power is

$$\Lambda_{th} T_1 = [(\alpha \tau_c - 1) - r_a (\alpha \tau_c + 1)]^{-1}. \quad (6.4)$$

The threshold pump power must be a positive quantity, this puts a constraint on the size of the ratio of decay times

$$r_a < \frac{\alpha \tau_c - 1}{\alpha \tau_c + 1}. \quad (6.5)$$

The right-hand side of Eqn. (6.5) is obviously less than one, therefore we must have  $r_a < 1$ ; the lowest upper bound of  $r_a$  is given by Eqn. (6.5). The quantity

$\alpha c \tau_c$  is much greater than one for typical dye lasers, therefore the lowest upper bound is very close to unity. The threshold excited state population is

$$d_{th} = \frac{1}{2}(n_{th} - w_{th}) = \frac{w_0}{1 - r_a}. \quad (6.6)$$

We see from this equation that when  $r_a \ll 1$  (i.e.,  $T_a \ll T_1$ ), the excited state population is equal to the inversion. Therefore, if the dye laser can be well-approximated by a three-level atom whose lower level decays much faster than the excited state, the excited state population will clamp at threshold. Since the fluorescence is proportional to the excited state population, the fluorescence will also clamp at threshold.

We compare the fluorescence versus pump power from the experiment with the theoretical predictions of this simple three-level analysis. The fluorescence is normalized by the fluorescence at threshold and the pump power is normalized to the pump power at threshold. Since the fluorescence is directly proportional to the excited state population, the fluorescence normalized by the threshold fluorescence will be equal to the normalized excited state population (the excited state population divided by the threshold excited state population). After a bit of algebra we find the normalized fluorescence,  $\bar{d} = d(0)/d_{th}$  as a function of the normalized pump power,  $\bar{\Lambda} = \Lambda/\Lambda_{th}$ ,

$$\bar{d} = (1 - r_a) \frac{r_a(\bar{\Lambda} - 1)(w_0 + 1) - w_0 + 1}{2r_a w_0 \bar{\Lambda} - r_a(w_0 + 1) - w_0 + 1}. \quad (6.7)$$

We use a simulated-annealing technique to minimize the square of the difference between the theory and data. The technique attempts to minimize the quantity

$$\chi^2 = \sum_i \left[ \bar{d}_i - (1 - r_a) \frac{r_a(\bar{\Lambda}_i - 1)(w_0 + 1) - w_0 + 1}{2r_a w_0 \bar{\Lambda}_i - r_a(w_0 + 1) - w_0 + 1} \right]^2, \quad (6.8)$$

by choosing the parameters  $w_0$  and  $r_a$  from a selected range of values. The sum over  $i$  represents a sum over the experimental points,  $\bar{\Lambda}_i$  and  $\bar{d}_i$ . In Figs. (6.3)

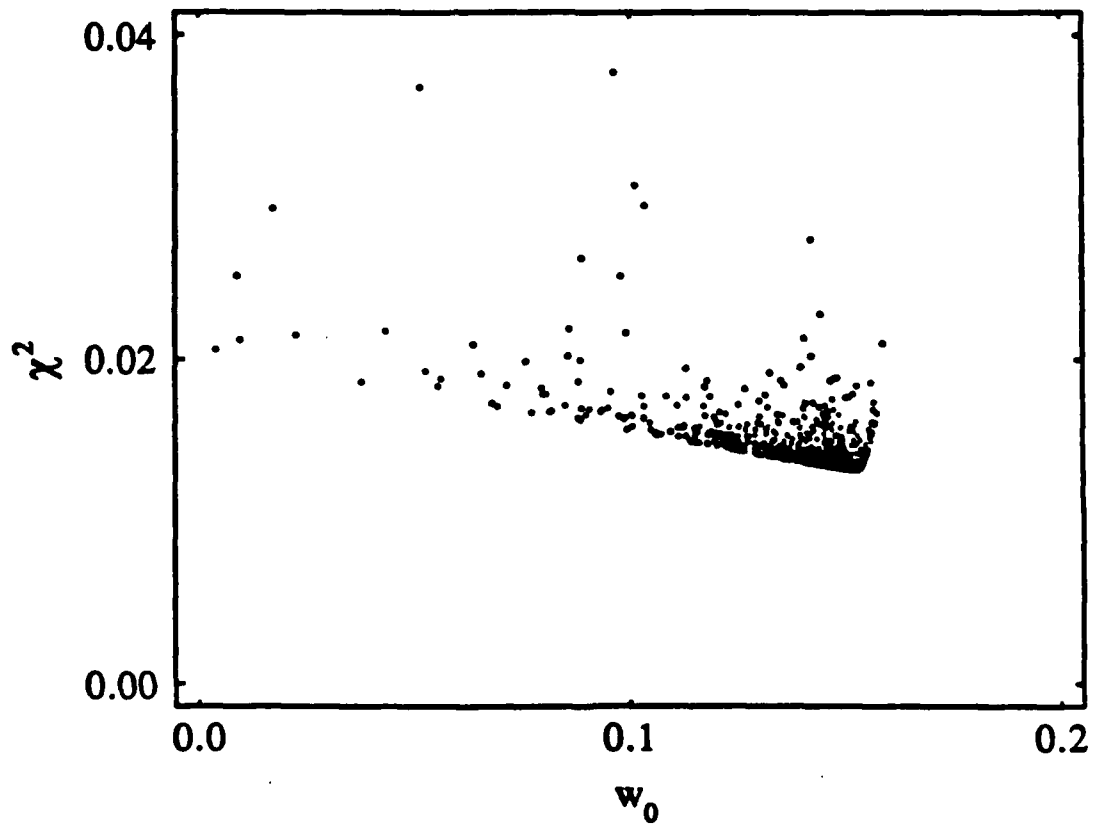


Fig. 6.3  $\chi^2$  for the experimental data versus the parameter  $w_0$  for the best fits to  $w_0$  and  $r_a$  to three-level laser theory. This Figure illustrates that there is a well-defined  $w_0$  value to minimize  $\chi^2$ .

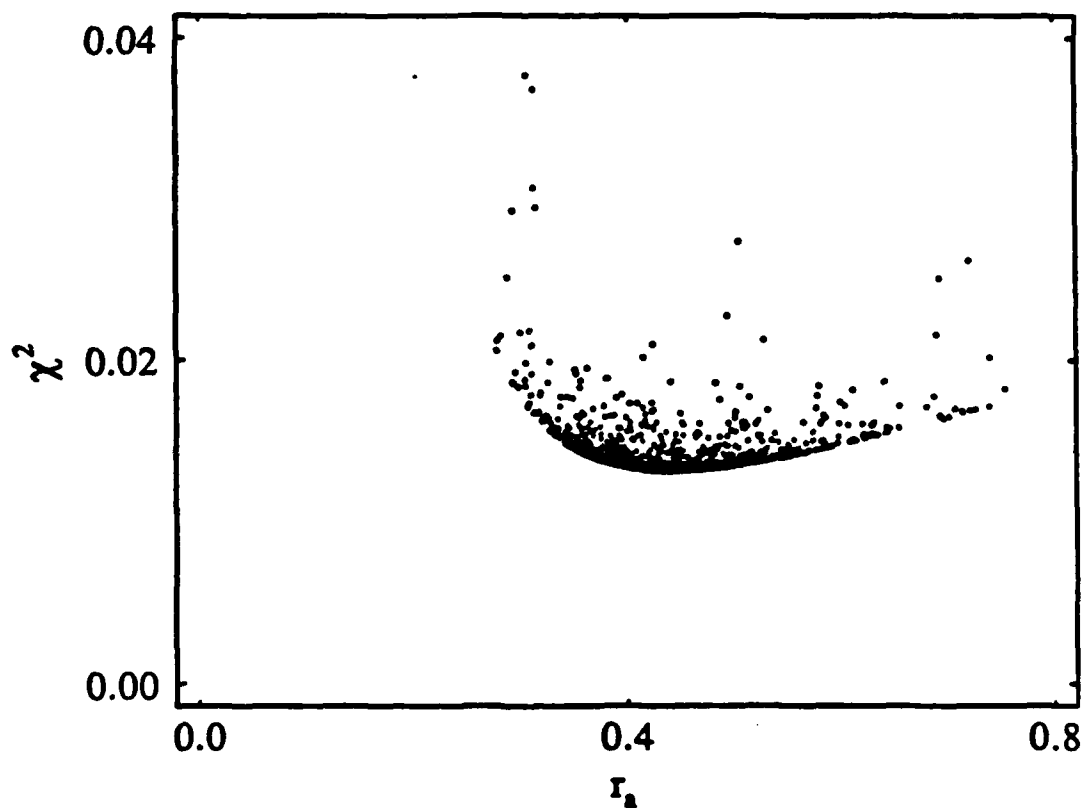
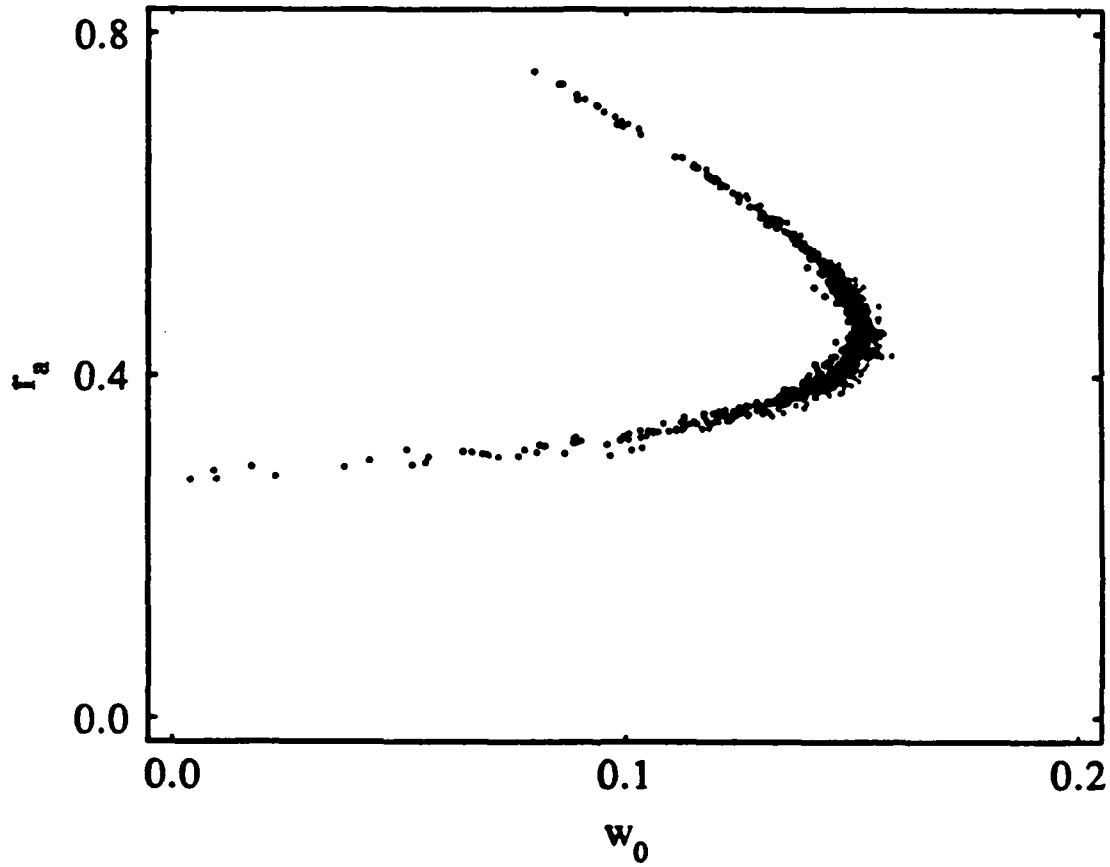


Fig. 6.4  $\chi^2$  for the experimental data versus the parameter  $\tau_a$  for the best fits to  $w_0$  and  $\tau_a$  to three-level laser theory. This Figure illustrates that there is a well-defined  $\tau_a$  value to minimize  $\chi^2$ .



**Fig. 6.5** Best fits of  $w_0$  versus  $r_a$  for the experimental data fit to three-level laser theory. This Figure illustrates that  $r_a$  lies between 0.3 and 0.7.

and (6.4) the value of  $\chi^2$  is plotted against  $w_0$  and  $r_a$  for a series of the best-fit parameters. Both plots have a well-defined minimum; this tells us that the data is a sensitive measure of the parameters of the theoretical fit. Figure (6.5) shows a plot of the best-fit parameters,  $w_0$  versus  $r_a$ . The best fits indicate  $r_a$  lies between 0.2 and 0.5; since the excited state decay time is known to be 5 nsec, three-level theory predicts the lower-level decay time is between 1 and 2.5 nsec. The best fit inversion,  $w_0$  for the three-level theory is between 0 and 0.15.

We generate the theoretical fit for the band model using Eqn. (5.26) divided by the threshold value of the excited state population,  $\bar{d} = d(0)/d_{th}$

$$\bar{d} = \frac{\sqrt{1 + r_a I(0)} \tan^{-1}(\zeta T_2)}{\tan^{-1} \left[ \frac{\zeta T_2}{\sqrt{1 + r_a I(0)}} \right]} \quad (6.9)$$

The data is fit using two parameters:  $\zeta T_2$ , and the product of  $r_a$  and the scaling factor between the intensity measured with the photodiode and the theoretical dimensionless intensity,  $I(0)$ ,  $\alpha$ . It should be noted that the ratio of decay times,  $r_a$  and the scaling factor between the intensity measured with the photodiode and the dimensionless intensity,  $I(0)$ ,  $\alpha$  appear as a product in the formula, Eqn. (6.9). Since we could arbitrarily increase  $r_a$  and correspondingly decrease the intensity scaling factor by the same amount, we see that there are only two independent parameters in Eqn. (6.9). Unfortunately, neither of these two parameters gives us  $r_a$ .

In order to obtain information about  $r_a$  we attempt to fit Eqn. (5.24) from Chapter VI. If we normalize the pump power by the threshold pump power and the the fluorescence to the threshold fluorescence we obtain

$$\bar{\Lambda} = \frac{(\bar{d} + \beta I)(1/d_{th} - r_a - 1)}{1/d_{th} + (r_a + 1)\bar{d} - r_a \beta I} \quad (6.10)$$



where  $\beta$  is the scaling factor (between the measured dye laser intensity and the dimensionless intensity) divided by  $gT_2d_{th}$ . When we fit the data to this expression, we find that the fit is extremely insensitive to the value of the ratio,  $\tau_a$ . Figure (6.6) shows a plot of  $\tau_a$  versus  $d_{th}$  for some of the best fits of the data. The best-fit values of  $\tau_a$  cover the entire physical range of the parameter; this indicates that these experimental results are not a good measure of  $\tau_a$  in this limit of the band model. In order to determine  $\tau_a$  for the band model and to examine the lower-level lifetime predicted from the simple three-level theory we conduct another experiment.

### 3. Modulation Spectroscopy of Lower Levels

We now discuss a second experiment that examines the lower-level decay time using modulation spectroscopy in a signal-limited fashion. Modulation spectroscopy has previously been used to measure the decay constants and dynamics in ruby, alexandrite, and fluorescein-doped boric-acid glass. In those experiments, a laser is weakly modulated to produce AM sidebands. The absorption or amplification of the sidebands is measured as a function of intensity and modulation frequency. In the limit of large modulation frequency, the absorption or amplification of the sidebands approaches that of the carrier. Modulation spectroscopy measures the population cycling rate of the system; that is the rate that population cycles around the energy levels of the system. This allows us to measure non-radiative decay rates in a system. Since the signal from the probe field rides on a DC bias, a large background has to be subtracted to obtain the actual signal. If we measure the fluorescence oscillating at the modulation frequency, the signal does not ride on a DC bias. This makes the measurement process signal-limited.

We use modulation spectroscopy in this new signal-limited fashion to mea-

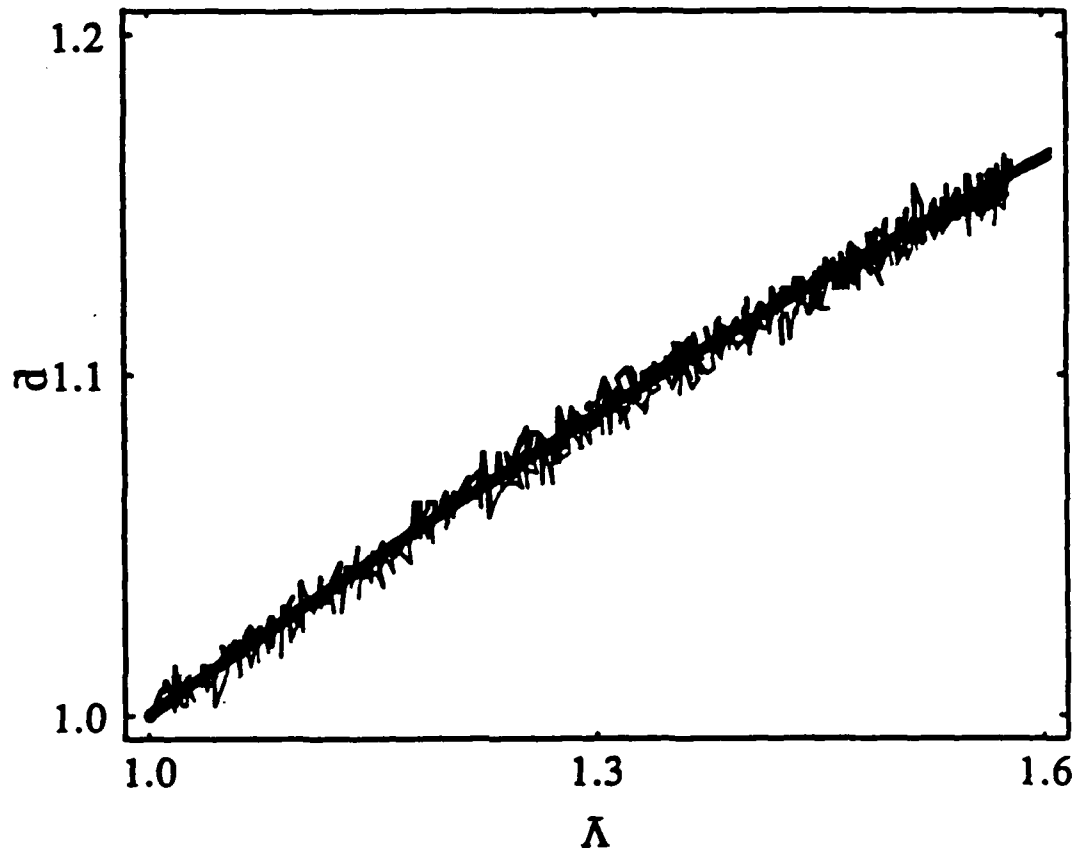
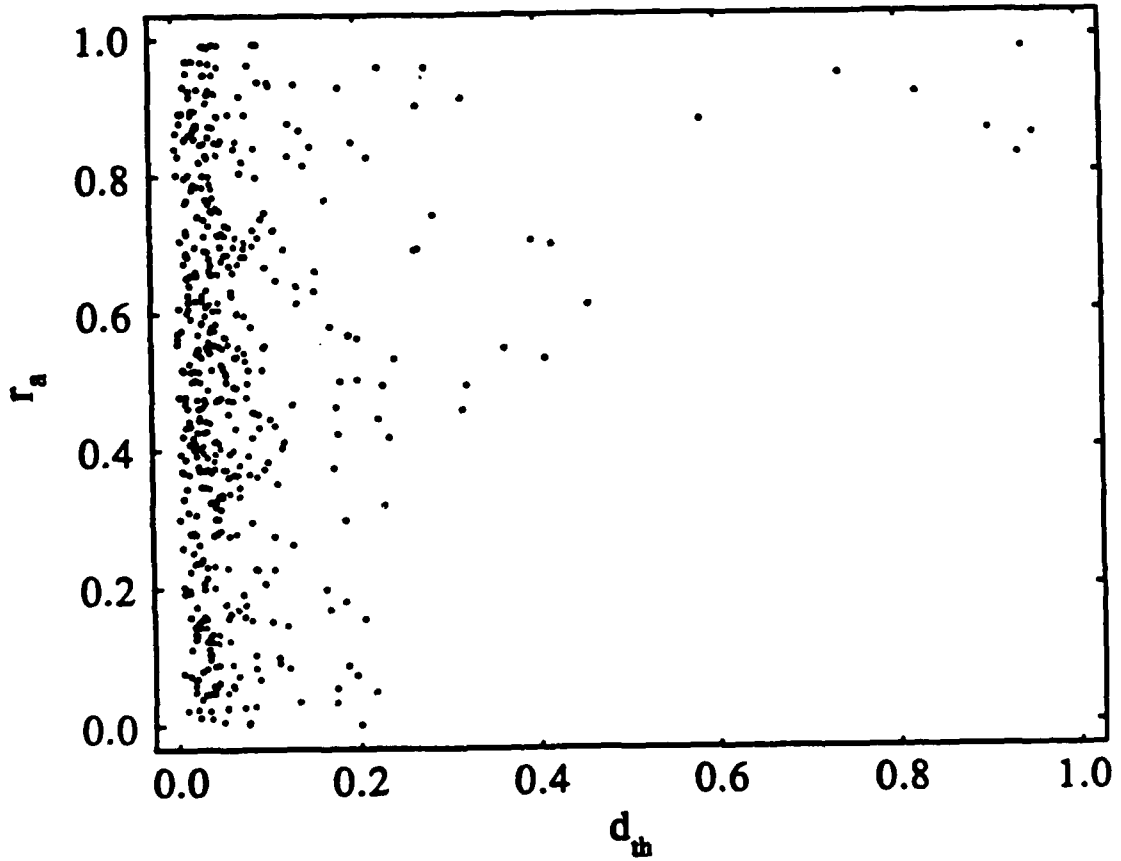


Fig. 6.6 Fluorescence versus pump power from a cw pumped multimode dye laser. The straight line represents the theoretical expression in Eqn. (6.7) with  $\tau_s = 0.44$  and  $w_0 = 0.15$ . The jagged line is the data taken in the experiment.

sure the lower-level decay rate of the rhodamine-6G dye molecule. The fluorescent intensity oscillating at the modulation frequency is measured as a function of intensity and modulation frequency. In the limit of large modulation frequency, the fluorescent intensity oscillating at the modulation frequency goes to zero. This feature makes this method of modulation spectroscopy signal-limited.

The experimental setup is sketched in Fig. (6.7). We weakly modulate a single-mode argon-ion laser (Coherent Innova 20 with single-mode etalon) with a Pockels cell (Inrad Model 212-090),  $\lambda/4$ -waveplate, and linear polarizer. We adjust the orientation of the fast axis of the  $\lambda/4$ -plate to maximize the intensity of the carrier frequency while still maintaining detectable sidebands. The Pockels cell is driven by the amplified signal from a voltage-controlled oscillator (Wavetek Model 1062). The rf-amplifier (Mini-Circuits Model ZHL-1-2W) driving the Pockels cell has a bandwidth of 500 MHz. The Pockels cell and amplifier radiate a large signal at the modulation frequency. We compensate for this by shielding the Pockels cell and amplifier in a 0.25 inch wire mesh cage. The cage allows us to easily get the laser through the modulator and also supplies the necessary air circulation for the amplifier to cool. The fluorescence is collected from the dye jet with a 10 mm focal length lens. The fluorescence is spatially filtered, to insure we are only looking at the center of the argon-ion-laser spot, and therefore a uniform intensity. We use a fast photodiode (EG&G FND-100 biased at 90 Volts DC) whose signal is amplified by a low noise 30 dB-gain amplifier (Trontech W500EF). The photodiode has a bandwidth in excess of 400 MHz. The amplifier has a flat response out to 500 MHz. The amplification of three orders of magnitude turns the photodiode and the cables connected to it into a reasonably good antenna. That is, radio stations and other electromagnetic sources are picked up by the photodiode and its cables and amplified by



**Fig. 6.7** Best fits of  $r_a$  versus  $d_{th}$  for the experimental data fit to band model laser theory. This Figure illustrates that the experimental measurements are not a good measure of the parameter  $r_a$ .

the 30 dB-gain amplifier to a significant level. In order to avoid this unwanted noise, the photodiode is also enclosed in a wire mesh cage. The amplified signal from the photodiode is sent to an rf-spectrum analyzer (Hewlett-Packard Model 8590A). The spectrum analyzer and the voltage-controlled oscillator are connected to a computer with analog-to-digital and digital-to-analog capabilities. The computer sweeps the frequency of the oscillator and then retrieves the spectrum from the rf-spectrum analyzer. We measure the system response by measuring the amplitude of the sidebands on the argon-ion laser as a function of modulation frequency using the photodiode and spectrum analyzer. All the data collected are normalized by the system response.

#### 4. Analysis and Results

In the absence of a coherent driving field the band model equations reduce to the equations describing a simple three-level system. The population of the lower band only appears as a sum over the entire band. We define the variable  $\mathcal{A} = \sum_{n=-N}^N a_n$ . We use this simple three-level model to fit the data of the fluorescence from the atoms driven by the modulated pump. Figure (6.2) shows the level structure and the associated decay times. The equations of the three-level system are

$$\dot{d} = -\frac{d}{T_1} + \Lambda(t)[1 - d - \mathcal{A}], \quad (6.11a)$$

$$\dot{\mathcal{A}} = \frac{d}{T_1} - \frac{\mathcal{A}}{T_a}, \quad (6.11b)$$

where  $\Lambda(t) = \Lambda_0 + 2\delta\Lambda \cos(\delta\omega t)$ . We can use Floquet's theorem and expand the variables in Fourier series of the modulation frequency. Since  $\delta\Lambda \ll \Lambda_0$  we can truncate the Fourier series to first order in the modulation amplitude  $\delta\Lambda$ . This is equivalent to truncating the Fourier series to the first harmonic component. The rf-spectrum analyzer measures the amplitude of the signal at the modulation

frequency. The amplitude of the fluorescence at the modulation frequency is directly proportional to the magnitude of the first harmonic component of the excited state population,  $|d_1|$

$$|d_1| = \frac{\delta\Lambda T_1 [1 - d_0(1 - r_a)]}{\sqrt{[1 + \Lambda_0 T_1(1 + L_a)]^2 + (\delta\omega T_1)^2 [1 - \Lambda_0 T_1 r_a L_a]^2}}, \quad (6.12)$$

where  $d_0 = \Lambda_0/[1 + \Lambda_0 T_1(1 + r_a)]$  is the time-averaged value of the excited state population and the Lorentzian function  $L_a = \frac{r_a}{1 + (\delta\omega T_a)^2}$ . It is interesting to consider some simple limits of Eqn. (6.12). In the limit that the time-averaged component of the pump intensity goes to zero,  $|d_1|$  becomes

$$\lim_{\Lambda_0 \rightarrow 0} |d_1| = \frac{\delta\Lambda T_1}{\sqrt{1 + (\delta\omega T_1)^2}}. \quad (6.13)$$

In this limit  $|d_1|$  is a square root of a Lorentzian (SRL) and is independent of the lower level decay time. The characteristic width of the curve is  $1/T_1$ . Another limit of interest is the limit where the lower level decays extremely fast

$$\lim_{T_a \rightarrow 0} |d_1| = \frac{\delta\Lambda T_1(1 - d_0)}{\sqrt{(1 + \Lambda_0 T_1)^2 + (\delta\omega T_1)^2}}. \quad (6.14)$$

In this limit  $|d_1|$  is just a SRL whose width increases linearly with the time-averaged value of the pump intensity. In cases where these limits are not valid we get more intuition from analyzing the plots of  $|d_1|$  as a function of modulation frequency,  $\delta\omega$ . If Fig. (6.8) we plot  $|d_1|$  for  $\Lambda_0 T_1 = 5$  and three different values of the ratio,  $r_a$ . We see from the plots that the spectra do not resemble SRLs. Therefore, for  $r_a \neq 0$ , we expect the spectra we measure to resemble SRLs at low pump intensity then deviate from this form as the pump intensity is increased. The point at which the spectra distinguish themselves from SRLs depends on the size of  $r_a$ . If  $r_a \gg 1$  (i.e.,  $T_a \gg T_1$ ), the spectra will deviate from SRLs for low pump intensity, while if  $r_a \ll 1$  (i.e.,  $T_a \ll T_1$ ), the spectra will not deviate from SRLs until  $\Lambda_0 T_1 \gg 1$ .

The data are fit to a SRL. The amplitudes of the curves are fit by minimizing the square of the difference between the theoretical curve and the experimental data, that is we minimize

$$\chi^2 = \sum_i \left[ f_i - \frac{a}{\sqrt{\gamma_L^2 + (2\pi\nu_i)^2}} \right]^2, \quad (6.15)$$

where the sum over  $i$  contains all the experimental points,  $\nu_i$  are the measured frequencies (in Hertz),  $f_i$  are the measured fluorescent intensities, and  $a$  is determined from

$$a = \left[ \sum_i \frac{f_i}{\sqrt{\gamma_L^2 + (2\pi\nu_i)^2}} \right] \left[ \sum_i \frac{1}{\gamma_L^2 + (2\pi\nu_i)^2} \right]^{-1}. \quad (6.16)$$

The results of the best-fit-theoretical plots are shown in Fig. (6.9). The data are well-described by SRLs. For the range of intensities used in the experiment, we calculate the largest value of  $\tau_a$  that still fits the data. The theoretical predictions begin to deviate from a SRL when  $\tau_a$  is on the order of 0.02 for 5 saturation intensities in the pump. This indicates that the decay time,  $T_a$  could be no larger than 100 ps. This decay time is insufficient to explain the increase in slope observed and is insufficient to account for the discontinuous jumps and hysteresis as explained by the theory of Fu and Haken.

## 5. Conclusions

In this Chapter we have described two experiments and their results. The first measured the fluorescence from a laser active medium. The experiment showed that the fluorescence, from a continuous-wave dye-jet laser, continues to increase above the laser threshold. Three-level laser theory predicts that the lower-level decay time must be between 0.3 and 0.7 times the decay time of the excited state for the observed rate of increase. This experiment was not a good measure of the parameters of the band model. We found the data could be fit

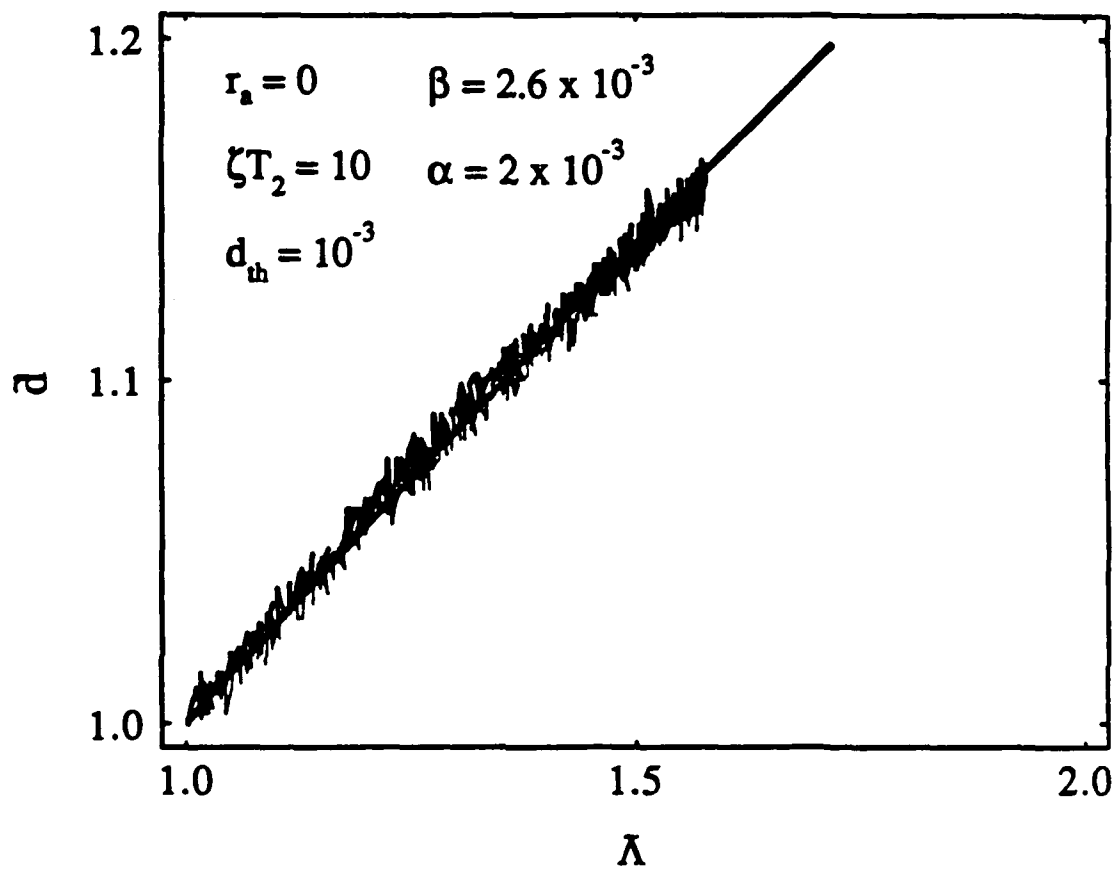
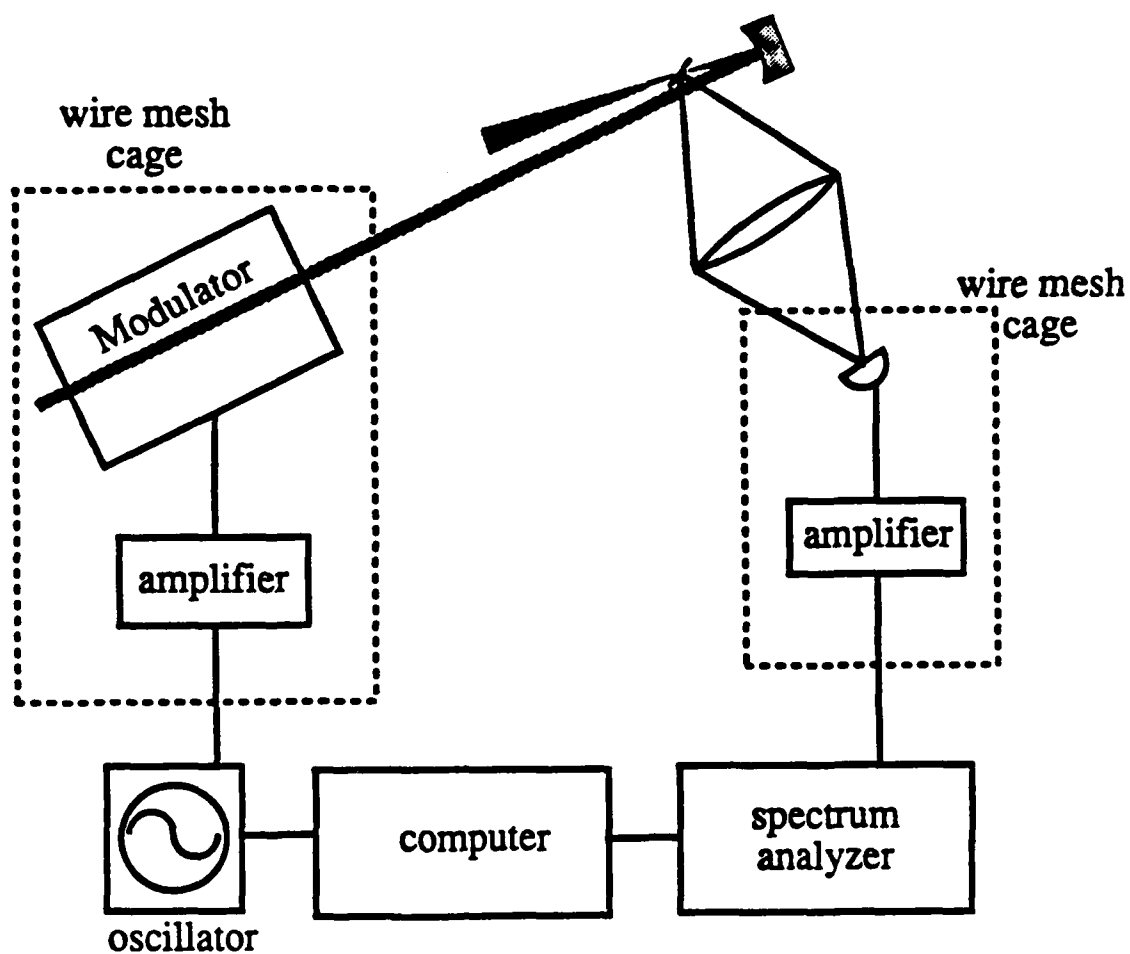


Fig. 6.8 Fluorescence versus pump power from a cw pumped multimode dye laser. This Figure demonstrates that the band model theory can fit the data quite well. We use Eqns. (6.9) and (6.10) for the theory with the listed parameters.





**Fig. 6.9** Experimental setup for fluorescence modulation spectroscopy experiment. A computer controls the oscillator driving the electro-optic modulator. The modulator modulates the argon-ion laser. The fluorescence from the dye jet is collected with a lens and the detected with a fast photodiode. The signal from the photodiode is amplified and sent to a spectrum analyzer. The spectrum analyzer then transfers the spectrum to the computer.

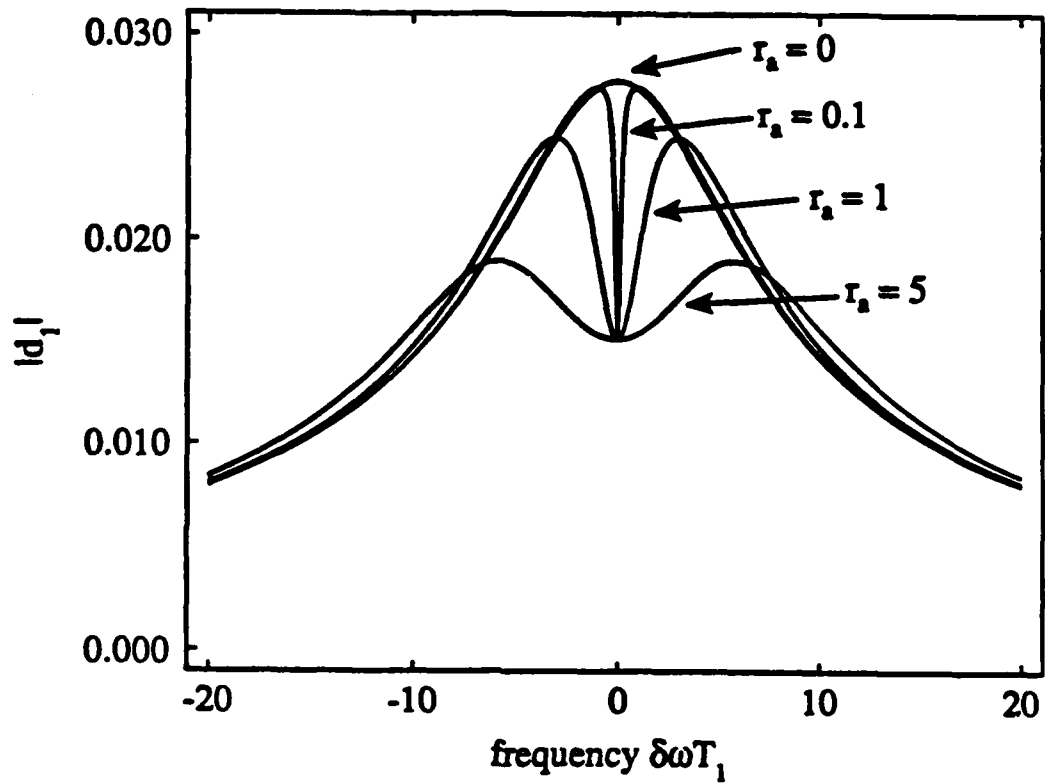
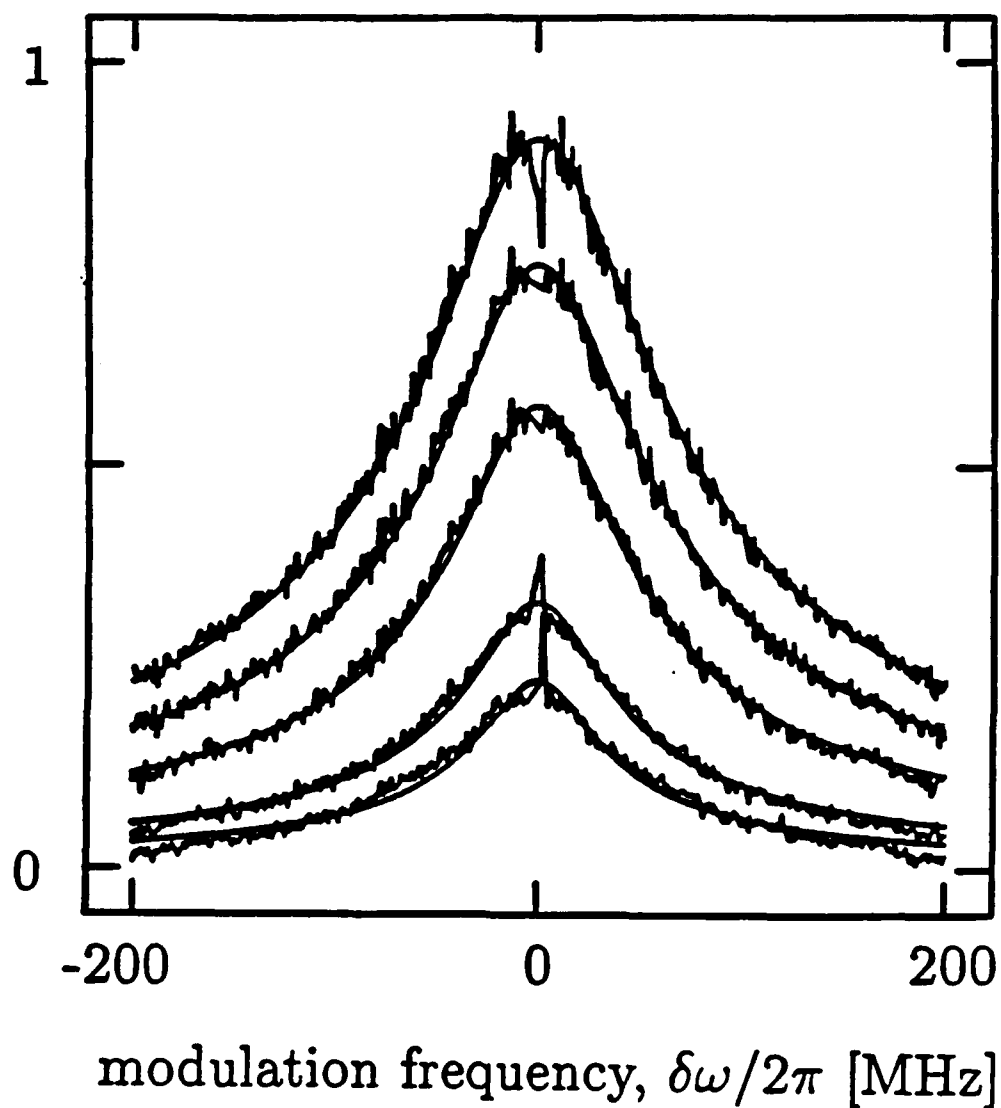


Fig. 6.10 Magnitude of the first harmonic component of the excited state population driven by a weakly modulated pump for series of  $r_a$ -values. The expression in Eqn. (6.12) is plotted for a series of  $r_a = 0, 0.1, 1, \text{ and } 5$ .



**Fig. 6.11** Magnitude of the first harmonic component of the fluorescence from dye molecules driven by a weakly modulated single-mode argon-ion laser. The fluorescence at the modulation frequency is plotted as a function of modulation frequency. The solid line is a best-fit square root of a Lorentzian function. The jagged line is the data for pump intensities equal to 0.7, 0.9, 1.75 and 2.75 Watts.

for the entire physical range of the parameter  $\tau_a$ . The second experiment used modulation spectroscopy in a new signal-limited fashion to measure an upper bound for the lower-level decay time. We found in this experiment that the lower-level decay time could be no longer than 100 psec. This is in direct contradiction to the three-level theoretical predictions of the first experiment. The resolution of the contradiction is that the dye laser cannot be accurately described using simple three-level laser theory. The results of the two experiments are in agreement with the predictions of the band model laser theory.

## SUMMARY

This thesis has described theoretical and experimental studies that deal with the two-frequency instability in a multimode cw ring rhodamine-6G-dye laser. The response of a two-level atom to a two-frequency field was calculated. The atom exhibits resonances when the field modulation frequency is equal to the Rabi frequency or one of its subharmonics. The maximum gain occurs when the modulation frequency is equal to the Rabi frequency. This result would explain why the separation of the two-frequency field in the dye laser increases quadratically with increasing laser power, if the Rabi frequency was responsible for the instability.

The gain of a subharmonic probe field in the presence of a strong 100% AM field was calculated. The calculations show that the strong two-frequency field is stable to the growth of a subharmonic probe field, except in the case of a frequency-dependent loss. The frequency-dependent loss allows the subharmonic probe field to destabilize the strong field. This thesis presents experiments where the frequency-dependent loss was changed to illustrate this point.

Chapter IV of this thesis extensively examines the two-frequency instability in the dye laser. The two-frequency instability is shown to exist in dye lasers with high cavity-Q and dye lasers with output couplers. The effects of heating

due to pumping with a multiline argon laser are shown to be insignificant as far as the two-frequency instability is concerned. The instability is also shown to occur in both bidirectional and unidirectional ring lasers.

The nonlinearity of the two-frequency instability was used to examine chaos in a nonlinear system, a subject of current research interest. The experiment demonstrated that when the dye laser is driven with commensurate modulation frequencies, the response is periodic; when the dye laser is driven by incommensurate modulation frequencies, the response is quasiperiodic. No chaos was detected in the dye laser response. The absence of chaos in such a nonlinear system is intriguing and suggests that new insights to the dynamics of the two-frequency instability can be found by analyzing the time-dependent behavior of the two-frequency state.

In Chapter V, the thesis examined the band model of a dye laser. The model successfully predicts a number of the experimental signatures of the two-frequency instability, most notably the low threshold for instability, a self-consistent two-frequency field, and quadratic dependence of the frequency separation of the two field components with increasing power. The theory also predicts three-, four-, five-, ... and  $n$ -frequency operation. The theory has not shown that these fields are stable to perturbations, only that they are self-consistent solutions to the equations. Future research in this area may explain why only two- and four-frequency operation were observed in the dye laser.

Finally, in Chapter VI, the thesis examines predictions of the band model to see if it is a feasible model for a dye molecule. The experiments demonstrate that a simple three-level atomic model of the dye molecule is inadequate to explain the experimental results. While the band model of the molecule is capable

of explaining the experimental results, the parameters of the model are not simply determined. Raman scattering from the ground state and photon echo experiments of rhodamine 6G will be useful in determining these parameters.

The two-frequency instability observed in the dye laser is not the instability predicted by Risken and Nummedal<sup>9-10</sup> and Graham and Haken<sup>11</sup>, which is associated with the sideband gain due to Rabi oscillations. The quadratic increase of the field separation of the two-frequency field in the dye laser does indicate that the Rabi frequency plays some part in the instability. The measured intensities and spectral splittings however, indicate that it is not a direct relationship, but that the spectral splitting is a harmonic of the Rabi frequency.

## Appendix A

In this Appendix we perform a linear stability analysis for the single-mode solution to the multimode rate equations and the multimode Maxwell-Bloch equations (MMMBE). The MMMBE describe the self-consistent interaction of a coherent field with a collection of homogeneously broadened two-level atoms. The gain and losses of the cavity are assumed to be uniformly distributed throughout the cavity. Since in a real laser, the gain and losses are typically localized at an active region, Brewster-angled surfaces, output couplers, etc., this approximation is valid for such lasers only if the amount of gain or loss in one round trip is small. Small in the sense that the intracavity intensity does not change significantly in one round trip, (i.e., it takes many round trips for the cavity to decay). If this is the case, then the gain and losses can be well-approximated as being uniformly distributed in the cavity. The slowly varying envelope and rotating-wave approximations are also made. These imply the field amplitude varies much slower than an optical period and that the Rabi frequency associated with the field amplitude is much smaller than the transition frequency of the atom. We also assume the field that drives the two-level atom is a semiclassical field. Dye molecules are typically modeled as ideal four-level



systems, however, the coherent interaction takes place between only two of the levels. The MMMBE for a field  $E = \mathcal{E} \exp(i\omega t) + \mathcal{E}^* \exp(-i\omega t)$  are

$$\dot{p} = (i\Delta - 1/T_2)p + \Omega w, \quad (\text{A.1a})$$

$$\dot{w} = -w/T_1 - (1/2)[p^*\Omega + p\Omega^*] + w_{eq}/T_1, \quad (\text{A.1b})$$

$$\dot{\Omega} = -c \frac{\partial}{\partial z} \Omega + \frac{\alpha_0 c}{2T_2} p - \frac{\Omega}{2\tau_c}. \quad (\text{A.1c})$$

Where  $p = v - iu$  is the complex polarization of the atom and  $u$  and  $v$  are defined in Chapter 2,  $w$  is the inversion,  $\Omega = 2d\mathcal{E}/\hbar$  is the normalized complex field amplitude,  $T_1$  ( $T_2$ ) is the inversion (polarization) relaxation time,  $\tau_c$  is the cavity decay time for the intensity,  $\Delta$  is the detuning between the laser carrier frequency,  $\omega$  and the atomic transition frequency  $\omega_0$ ,  $\Delta = \omega - \omega_0$ ,  $w_{eq}$  is the value the inversion decays to in the absence of a coherent driving field and represents the pump parameter of the laser, and  $\alpha_0 = 4\pi\mathcal{N}d^2\omega T_2/\hbar c$  is the inverse Beer's absorption length, where  $\mathcal{N}$  is the atomic number density,  $d$  is the dipole moment between the two levels,  $\hbar$  is Planck's constant divided by  $2\pi$ , and  $c$  is the speed of light. The variables  $\Omega$  and  $p$  in Eqns. (A.1) are complex variables. The real (imaginary) part represents the component of the complex variable in-phase (in-quadrature) to the rotating frame. The polar form of these equations, derived later in this appendix, illustrates that the equations are independent of the phase angle between the rotating frame and the complex variables.

An atom radiating in free space has a definite relationship between  $T_1$  and  $T_2$  ( $T_2 = 2T_1$ ). However, often times atoms are subjected to phase disrupting collisions that do not effect the atomic population. These phase disruptions cause the average polarization of the atoms to decay more rapidly than an atom

in free space. When the collisions are sufficiently frequent, the relaxation rate of the polarization can be the fastest rate in the system. If the relaxation rate of the polarization is much faster than any other rate in the system, the dynamics of the polarization are well-described by its steady state solution written in terms of the inversion and the electric field. That is, the polarization adiabatically follows the inversion and electric field. We can see this more clearly by formally integrating Eqn. (A.1a)

$$p(t) = p(0) \exp[(i\Delta - 1/T_2)t] + \int_0^t \Omega w \exp[(i\Delta - 1/T_2)(t - t')] dt'$$

$$p(t) = p(0) \exp[(i\Delta - 1/T_2)t] - \frac{\Omega T_2 w}{1 - i\Delta T_2} (1 - \exp[(i\Delta - 1/T_2)t]) \\ + \int_0^t \frac{d}{dt} (\Omega T_2 w) \frac{\exp[(i\Delta - 1/T_2)(t - t')]}{1 - i\Delta T_2} dt'$$

In the limit where  $T_2$  is the shortest time scale in the system (i.e.,  $|\dot{\Omega}/\Omega| \ll 1/T_2$ ,  $|\dot{w}/w| \ll 1/T_2$ ), the integrand in the equation is small compared to the other terms. Therefore, for times long compared to  $T_2$  (i.e.,  $t \gg T_2$ ), the polarization is given by

$$p(t) = -\frac{\Omega T_2 w}{1 - i\Delta T_2}.$$

This procedure is known as adiabatic elimination or the slaving principle. This limit is especially applicable to the dye laser where  $T_2$  is on the order of femtoseconds and  $T_1$  is on the order of nanoseconds, six orders of magnitude longer than  $T_2$ . This Appendix demonstrates that the MMMBE become unstable far above threshold in the limit where  $T_2 \ll T_1$ . The rate equations, however, fail to predict the instability.

## 2. Multimode Rate Equation Stability Analysis

The equations for the inversion and electric field that result from the elimination of the polarization are the rate equations

$$\dot{w} = -\frac{1}{T_1} [(1 + I)w - w_{eq}], \quad (A.2a)$$

$$\dot{I} = \left( \frac{\alpha_0 c}{1 + (\Delta T_2)^2} w - \frac{1}{\tau_c} \right) I - c \frac{\partial}{\partial z} I, \quad (A.2b)$$

where  $I = |\Omega|^2 T_1 T_2 / [1 + (\Delta T_2)^2]$ . The steady state values of these equations have two regions of solution. The first solution we analyze is the off-solution

$$w_{off} = w_{eq}, \quad (A.3a)$$

$$I_{off} = 0. \quad (A.3b)$$

We assume  $w = w_{off} + \delta w$  and  $I = I_{off} + \delta I$ . If we linearize the rate equations about the steady state solution, we obtain a set of equations describing the dynamics of small perturbations about the steady state

$$\frac{d}{dt} \begin{bmatrix} \delta w \\ \delta I \end{bmatrix} = \begin{bmatrix} -1/T_1 & w_{eq} \\ 0 & \frac{\alpha_0 c w_{eq}}{1 + (\Delta T_2)^2} - \frac{1}{\tau_c} \end{bmatrix} \begin{bmatrix} \delta w \\ \delta I \end{bmatrix} - c \frac{\partial}{\partial z} \begin{bmatrix} 0 \\ \delta I \end{bmatrix}. \quad (A.4)$$

The solution for the intensity perturbation,  $\delta I$  is of the form

$$\delta I(t) = \delta I_1 \exp(i\zeta z/c + \beta t) + \delta I_1^* \exp(-i\zeta z/c + \beta^* t). \quad (A.5)$$

Plugging this solution into Eqn. (A.4) gives us two equations involving the real and imaginary parts of  $\beta = \beta' + i\beta''$ , where  $\beta'$  and  $\beta''$  are both purely real quantities

$$\beta'' + \zeta = 0, \quad (A.6a)$$

$$\beta' - \frac{\alpha_0 c w_{eq}}{1 + (\Delta T_2)^2} + \frac{1}{\tau_c} = 0. \quad (A.6b)$$

The equation for  $\beta'$ , Eqn. (A.6b) describes the stability of the off-solution. When  $\beta'$  is negative, the perturbation will exponentially decay to zero; when  $\beta'$  is positive, the perturbation will exponentially grow. Therefore, when  $w_{eq} < \frac{1 + (\Delta T_2)^2}{\alpha_0 c \tau_c}$ , the off-solution will be stable. However, when  $w_{eq} > \frac{1 + (\Delta T_2)^2}{\alpha_0 c \tau_c}$ , the off-solution becomes unstable. Therefore, the rate equations predict a laser threshold when the pump parameter exceeds a definite value,  $w_{eq}(\text{threshold}) = \frac{1 + (\Delta T_2)^2}{\alpha_0 c \tau_c}$ . The corresponding solution for the inversion also becomes unstable for the same pump parameter.

We now examine the second region of solution for the rate equations, the on-solution

$$w_{on} = \frac{1 + (\Delta T_2)^2}{\alpha_0 c \tau_c}, \quad (A.7a)$$

$$I_{on} = (\bar{w}_{eq} - 1) = \left[ \frac{w_{eq} \alpha_0 c \tau_c}{1 + (\Delta T_2)^2} - 1 \right]. \quad (A.7b)$$

where  $\bar{w}_{eq} = w_{eq}/w_{on}$ . The first equation says the inversion is a constant for the on-solution. This phenomena is known as inversion clamping. The laser-atom interaction holds the population inversion to a constant value and all the additional pump energy is converted to laser energy. The second equation tells us that the on-solution is unphysical for  $w_{eq} < \frac{1 + (\Delta T_2)^2}{\alpha_0 c \tau_c}$  (i.e., the on-solution is unphysical where the off-solution is stable). If we linearize the rate equations about this steady state solution, we obtain the following equations that describe the dynamics of small perturbations about the on-solution

$$\frac{d}{dt} \begin{bmatrix} \delta w \\ \delta I \end{bmatrix} = \begin{bmatrix} -\frac{\bar{w}_{eq}}{T_1} & -\frac{w_0}{T_1} \\ \frac{\alpha_0 c I_0}{1 + (\Delta T_2)^2} & 0 \end{bmatrix} \begin{bmatrix} \delta w \\ \delta I \end{bmatrix} - c \frac{\partial}{\partial z} \begin{bmatrix} 0 \\ \delta I \end{bmatrix}. \quad (A.8)$$

The solution to this equation has the form

$$\begin{bmatrix} \delta w(t) \\ \delta I(t) \end{bmatrix} = \begin{bmatrix} \delta w_1 \\ \delta I_1 \end{bmatrix} \exp(i\zeta z/c + \beta t) + \begin{bmatrix} \delta w_1^* \\ \delta I_1^* \end{bmatrix} \exp(-i\zeta z/c + \beta^* t), \quad (A.9)$$

where  $\beta = \beta' + i\beta''$  and  $\beta'$  and  $\beta''$  are both real numbers. Plugging this solution into Eqn. (A.8) we reduce the problem to two linear equations and two unknowns

$$\begin{bmatrix} -\frac{\bar{w}_{eq}}{T_1} - \beta & -\frac{w_0}{T_1} \\ \frac{\alpha_0 c I_0}{1 + (\Delta T_2)^2} & -i\zeta - \beta \end{bmatrix} \begin{bmatrix} \delta w_1 \\ \delta I_1 \end{bmatrix} = \begin{bmatrix} 0 \\ 0 \end{bmatrix}. \quad (\text{A.10})$$

If the solution to this equation is to be something other than the trivial solution, the determinant of the matrix in Eqn. (A.10) must vanish. Using this we obtain an equation for  $\beta$

$$\beta^2 + \beta \left( \frac{\bar{w}_{eq}}{T_1} + i\zeta \right) + i\zeta \frac{\bar{w}_{eq}}{T_1} + I_0 / (T_1 \tau_c) = 0. \quad (\text{A.11})$$

The boundary between stability and instability occurs when the real part of  $\beta$  goes to zero. We can determine this boundary in terms of  $I_0$ ,  $\zeta$ ,  $\beta''$  and the parameters of the laser, by setting  $\beta = i\beta''$ . When we insert this for  $\beta$  in Eqn. (A.11) we obtain two equations from the real and imaginary parts of the expression

$$\beta'' + \zeta = 0, \quad (\text{A.12})$$

$$\beta''^2 + \beta'' \zeta - I_0 / (T_1 \tau_c) = 0. \quad (\text{A.13})$$

Together these equations imply that the boundary of instability occurs when

$$I_0 / (T_1 \tau_c) = 0. \quad (\text{A.14})$$

For  $I_0 \neq 0$ , there is no instability boundary. Since for  $\zeta = 0$  we can solve for  $\beta$  explicitly

$$\beta = -\frac{1}{2T_1} \bar{w}_{eq} \pm \frac{1}{2} \sqrt{\frac{1}{T_1^2} \bar{w}_{eq}^2 - \frac{4I_0}{T_1 \tau_c}}, \quad (\text{A.15})$$

we see that  $\beta'(\zeta = 0) < 0$ . Therefore since  $\beta'$  is negative for  $\zeta = 0$  and  $\beta'$  never goes through zero,  $\beta' < 0$  is for all values of  $\zeta$  and  $I_0$ , and the on-solution is stable for  $w_{eq} > \frac{1 + (\Delta T_2)^2}{\alpha_0 c \tau_c}$ . So, the single-mode on-solution of the multimode rate equations is always stable above threshold!

### 3. Multimode Maxwell-Bloch Equations Stability Analysis

We now examine the stability of the MMMBE's steady state solutions. The off-solution predicts the same laser threshold that the multimode rate equations predict. The stability of the on-solution for the MMMBE however is different from that predicted by the rate equations. A convenient way to approach the problem is to normalize the equations of motion by the steady state values of the problem. The steady state values of the normalized equations are then simply unity. The steady state values of the MMMBE are

$$p_0 = \Omega_0 T_2 w_0, \quad (A.16a)$$

$$w_0 = \frac{1}{\alpha_0 c \tau_c}, \quad (A.16b)$$

$$\Omega_0 = \frac{\exp(i\psi)}{\sqrt{T_1 T_2}} \sqrt{w_{eq} \alpha_0 c \tau_c - 1}, \quad (A.16c)$$

where  $\psi$  is an arbitrary phase that, without loss of generality, we will take to be zero. We then define the normalized variables

$$\bar{p} = p/p_0, \quad (A.17a)$$

$$\bar{w} = w/w_0, \quad (A.17b)$$

$$\bar{w}_{eq} = w_{eq}/w_0 \quad (A.17c)$$

$$\bar{\Omega} = \Omega/\Omega_0 \quad (A.17d)$$

The equations of motion for these normalized variables are then

$$\dot{\bar{p}} = -\frac{1}{T_2}(\bar{p} - \bar{\Omega}\bar{w}), \quad (\text{A.18a})$$

$$\dot{\bar{w}} = -\frac{1}{T_1} \left[ \bar{w} - \bar{w}_{eq} + \frac{1}{2}(\bar{w}_{eq} - 1)(\bar{p}^* \bar{\Omega} + \bar{p} \bar{\Omega}^*) \right], \quad (\text{A.18b})$$

$$\dot{\bar{\Omega}} = \frac{1}{2\tau_c}(\bar{p} - \bar{\Omega}) - c \frac{\partial}{\partial z} \bar{\Omega}. \quad (\text{A.18c})$$

It is now convenient to convert the complex quantities  $\bar{\Omega}$  and  $\bar{p}$  to polar coordinates

$$\bar{p} = |\bar{p}| \exp(i\theta), \quad (\text{A.19a})$$

$$\bar{\Omega} = |\bar{\Omega}| \exp(i\phi). \quad (\text{A.19b})$$

The equations of motion for these real variables then become

$$|\dot{\bar{p}}| = -\frac{1}{T_2} \left( |\bar{p}| - |\bar{\Omega}| \bar{w} \cos(\phi - \theta) \right), \quad (\text{A.20a})$$

$$\dot{\bar{w}} = -\frac{1}{T_1} \left( \bar{w} - \bar{w}_{eq} + (\bar{w}_{eq} - 1) |\bar{p}| |\bar{\Omega}| \cos(\phi - \theta) \right), \quad (\text{A.20b})$$

$$|\dot{\bar{\Omega}}| = \frac{1}{2\tau_c} \left( |\bar{p}| \cos(\phi - \theta) - |\bar{\Omega}| \right) - c \frac{\partial}{\partial z} |\bar{\Omega}|, \quad (\text{A.20c})$$

$$\dot{\theta} = \frac{1}{T_2} (|\bar{\Omega}|/|\bar{p}|) \bar{w} \sin(\phi - \theta), \quad (\text{A.20d})$$

$$\dot{\phi} = -\frac{1}{2\tau_c} (|\bar{p}|/|\bar{\Omega}|) \sin(\phi - \theta) - c \frac{\partial}{\partial z} \phi. \quad (\text{A.20e})$$

Since the polar form of the MMMBE depends only on the difference of the two phases, the equations are independent of the phase angle between the rotating frame and the complex variables,  $p$  and  $\Omega$ . We now linearize these equations about the on-solution's steady state values,  $|\bar{p}| = 1 + \delta p$ ,  $\bar{w} = 1 + \delta w$ ,  $|\bar{\Omega}| = 1 + \delta \Omega$ ,  $\theta = \theta_0 + \delta \theta$ , and  $\phi = \phi_0 + \delta \phi$ . For convenience we set  $\theta_0 = \phi_0 = 0$ , without loss of generality. The equations describing the dynamics of the perturbations are

$$\delta \dot{p} = -\frac{1}{T_2} (\delta p - \delta \Omega - \delta w), \quad (\text{A.21a})$$

$$\delta \dot{w} = -\frac{1}{T_1} [\delta w + (\bar{w}_{eq} - 1)(\delta \Omega + \delta p)], \quad (\text{A.21b})$$

$$\delta \dot{\Omega} = \frac{1}{2\tau_c} (\delta p - \delta \Omega) - c \frac{\partial}{\partial z} \delta \Omega, \quad (\text{A.21c})$$

$$\delta \dot{\theta} = \frac{1}{T_2} (\delta \phi - \delta \theta), \quad (\text{A.21d})$$

$$\delta \dot{\phi} = -\frac{1}{2\tau_c} (\delta \phi - \delta \theta) - c \frac{\partial}{\partial z} \delta \phi. \quad (\text{A.21e})$$

The solution to these equations has the form

$$\begin{bmatrix} \delta p \\ \delta w \\ \delta \Omega \\ \delta \theta \\ \delta \phi \end{bmatrix} = \begin{bmatrix} \delta p \\ \delta w \\ \delta \Omega \\ \delta \theta \\ \delta \phi \end{bmatrix} \exp(i\zeta z/c + \beta t) + \begin{bmatrix} \delta p^* \\ \delta w^* \\ \delta \Omega^* \\ \delta \theta^* \\ \delta \phi^* \end{bmatrix} \exp(-i\zeta z/c + \beta^* t). \quad (\text{A.22})$$

We plug this solution into Eqns. (A.21) and obtain a set of five linear equations and five unknowns

$$\begin{bmatrix} \frac{1}{T_2} + \beta & -\frac{1}{T_2} & -\frac{1}{T_2} & 0 & 0 \\ \frac{1}{T_1} (\bar{w}_{eq} - 1) & \frac{1}{T_1} + \beta & \frac{1}{T_1} (\bar{w}_{eq} - 1) & 0 & 0 \\ -\frac{1}{2\tau_c} & 0 & i\zeta + \frac{1}{2\tau_c} + \beta & 0 & 0 \\ 0 & 0 & 0 & \frac{1}{T_2} + \beta & -\frac{1}{T_2} \\ 0 & 0 & 0 & -\frac{1}{2\tau_c} & i\zeta + \frac{1}{2\tau_c} + \beta \end{bmatrix} \begin{bmatrix} \delta p \\ \delta w \\ \delta \Omega \\ \delta \theta \\ \delta \phi \end{bmatrix} = \begin{bmatrix} 0 \\ 0 \\ 0 \\ 0 \\ 0 \end{bmatrix}. \quad (\text{A.23})$$

As before, for solutions other than the trivial solution to exist, the determinant of the matrix in Eqn. (A.23) must vanish. This implies

$$\begin{aligned} \beta^3 + \beta^2 \left[ \frac{1}{T_1} + \frac{1}{T_2} + \frac{1}{2\tau_c} + i\zeta \right] + \beta \left[ \frac{\bar{w}_{eq}}{T_1 T_2} + \frac{1}{2T_1 \tau_c} + i\zeta \left( \frac{1}{T_1} + \frac{1}{T_2} \right) \right] \\ + \frac{\bar{w}_{eq} - 1}{T_1 T_2 \tau_c} + i\zeta \frac{\bar{w}_{eq}}{T_1 T_2} = 0, \end{aligned} \quad (\text{A.24a})$$

and

$$\beta^2 + \beta \left( \frac{1}{T_2} + \frac{1}{2\tau_c} + i\zeta \right) + i\zeta \frac{1}{T_2} = 0. \quad (\text{A.24b})$$

In a manner similar to the solution of the rate equations' stability, we set  $\beta = i\beta''$  and solve for the boundary between stability and instability, that is we set



$\beta' = 0$ . Equation (A.24b) gives the dispersion relation for the phases of the electric field and polarization. Equation (A.24a) gives the dispersion relation of the inversion and the amplitudes of the polarization and electric field strength. The dispersion relation for the phases predicts no boundary of instability for the phases. However, the phases are marginally unstable, that is  $\beta' = 0$ , for  $\zeta = 0$ . Noise in the amplitude of the field or polarization, at the same frequency as the steady state laser field, may change the phase angle between the field and the polarization. This is not an instability unless noise is present.

The dispersion relation for the amplitudes of the variables reduces to two equations when we substitute  $\beta = i\beta''$

$$-\beta''^2 \left( \frac{1}{T_1} + \frac{1}{T_2} + \frac{1}{2\tau_c} \right) - \beta'' \zeta \left( \frac{1}{T_1} + \frac{1}{T_2} \right) + \frac{\bar{w}_{eq} - 1}{T_1 T_2 \tau_c} = 0, \quad (\text{A.25a})$$

$$-\beta''^3 - \zeta \beta''^2 + \beta'' \left( \frac{1}{2T_1 \tau_c} + \frac{\bar{w}_{eq}}{T_1 T_2} \right) + \zeta \frac{\bar{w}_{eq}}{T_1 T_2} = 0. \quad (\text{A.25b})$$

We solve for  $\beta'' \zeta$  in Eqn. (A.25a)

$$\beta'' \zeta = \frac{(\bar{w}_{eq} - 1)/(T_1 T_2 \tau_c) - \beta''^2 [1/T_1 + 1/T_2 + 1/(2\tau_c)]}{1/T_1 + 1/T_2}. \quad (\text{A.26})$$

We then multiply Eqn. (A.25b) by  $\beta''$ , so that all the occurrences of  $\zeta$  also contain  $\beta''$ . We substitute Eqn. (A.26) for these occurrences and obtain a quadratic equation in  $\beta''^2$

$$\beta''^4 + \beta''^2 \left( \frac{1}{T_1^2} - 3 \frac{\bar{w}_{eq} - 1}{T_1 T_2} \right) + 2 \bar{w}_{eq} \frac{\bar{w}_{eq} - 1}{T_1^2 T_2^2} = 0. \quad (\text{A.27})$$

The solution to this quadratic equation is

$$\beta''^2 = \frac{1}{2T_1} \left[ \frac{3(\bar{w}_{eq} - 1)}{T_2} - \frac{1}{T_1} \pm \sqrt{(\bar{w}_{eq} - 1)(\bar{w}_{eq} - 9)/T_2^2 - 6(\bar{w}_{eq} - 1)/(T_1 T_2) + 1/T_1^2} \right]. \quad (\text{A.28})$$

Since  $\beta''$  is real,  $\beta''^2$  must be real and positive. The quantity  $\beta''^2$  will be real if the square root in Eqn. (A.28) is positive. This condition puts a constraint on the pump parameter

$$\bar{w}_{eq} > 5 + 3T_2/T_1 + 2\sqrt{4 + 6T_2/T_1 + 2T_2^2/T_1^2}. \quad (\text{A.29})$$

The condition that  $\beta''^2$  is positive adds no further constraints, so the instability boundary is determined by Eqn. (A.29).

The frequency of the unstable mode at the boundary of the instability is given by Eqn. (A.28); in addition to this relation, the value of the frequency of the unstable mode must satisfy the cavity boundary conditions. This could cause the instability to appear at a higher threshold than the minimum threshold predicted by Eqn. (A.29).

It is interesting to note that the lowest threshold for instability occurs for  $T_1 \gg T_2$ , (i.e.,  $\bar{w}_{eq}(T_1 \gg T_2) = 9$ ). This is the limit where the rate equations are valid. If the frequency of the unstable mode or the Rabi frequency necessary for the instability is greater than  $1/T_2$ , then we should not expect the rate equations to make this prediction. The frequency of the unstable mode in the limit  $T_1 \gg T_2$  is

$$\lim_{T_2 \ll T_1} \beta'' T_2 = \lim_{T_2 \ll T_1} 2\sqrt{3}\sqrt{T_2/T_1} = 0. \quad (\text{A.30})$$

This indicates that in the limit that  $T_1 \gg T_2$  the unstable mode frequency is less than  $1/T_2$ . Therefore, the frequency of the unstable mode does not violate the adiabatic elimination assumptions. The spatial variation of the perturbation is given by the variable  $\zeta$ . From Eqn. (A.26) we find

$$\zeta T_2 = \frac{(w_{eq} - 1)T_2^2}{T_1 \tau_c (1 + T_2/T_1) \beta'' T_2} - \frac{1 + T_2/T_1 + T_2/(2\tau_c)}{1 + T_2/T_1}, \quad (\text{A.31})$$

which in the limit that  $T_1$  and  $\tau_c \gg T_2$  becomes

$$\lim_{T_2 \ll T_1, \tau_c} \zeta T_2 = \lim_{T_2 \ll T_1, \tau_c} \left[ \frac{w_{eq} - 1}{2\sqrt{3}} \frac{T_2}{\tau_c} - 2\sqrt{3} \right] \sqrt{T_2/T_1} = 0. \quad (\text{A.32})$$

Therefore the temporal and spatial oscillation frequencies of the unstable perturbation both go to zero in the limit that  $T_1 \gg T_2$ . This indicates that the rate equation approximation is not violated by the unstable mode. The field amplitude of the laser at the boundary of the instability is given by

$$|\Omega|^2 T_1 T_2 = (\bar{w}_{eq} - 1) = 8,$$

$$(|\Omega| T_2)^2 = 8 T_2 / T_1,$$

$$|\Omega| T_2 = 2\sqrt{2} \sqrt{T_2/T_1}$$

and

$$\lim_{T_2 \ll T_1} |\Omega| T_2 = 0. \quad (\text{A.32})$$

Therefore the Rabi frequency associated with the field amplitude is also less than  $1/T_2$ , for  $T_1 \gg T_2$ . So the instability predicted by the MMMBE is within the approximations of the rate equations, even though the rate equations do not predict the instability. Therefore the adiabatic elimination procedure can be invalid in the region of instability. (I say "can" here since the rate equations and the MMMBE predict the same threshold for lasing). This emphasizes that the polarization of the medium plays a dynamic role in the instability predicted by the MMMBE.

It should also be noted that Graham and Haken carried out a similar calculation including the effects of quantum noise and found the same results as

this semiclassical treatment. This indicates that the instability is not associated with quantum mechanical fluctuations, but is a semiclassical effect of the nonlinearities of the MMMBE. Physically, the instability occurs when the gain that sidemodes experience in the presence of a strong field becomes sufficient to overcome the losses of the cavity and the sidemodes begin to oscillate.

The MMMBE predict that the steady state solution will go unstable as low as 9 times above the threshold for lasing. Experiments with dye lasers, discussed in the Chapter IV, have demonstrated that a homogeneously broadened laser can go unstable as low as 1.5 times above the threshold for lasing.

## References

- [1] T. H. Maiman, "Stimulated optical radiation in ruby," *Nature* **187**, 493-494 (1960).
- [2] D. F. Nelson and W. S. Boyle, "A continuously operating ruby laser," *Appl. Opt.* **1**, 181 (1962).
- [3] M. Birnbaum, A. W. Tucker, and C. L. Fincher, "CW ruby laser pumped by an argon ion laser," *IEEE J. Quantum Electron.* **QE-13**, 808-809 (1977).
- [4] H. Statz and G deMars, "Transients and oscillation pulses in masers," in *Quantum Electronics* (Columbia University Press, New York, 1960), p. 530-537.
- [5] G. Mahkov, "On the problem of pulsed oscillations in ruby maser," *J. Appl. Phys.* **33**, 202-204 (1962).
- [6] D. M. Sinnett, "An analysis of the maser oscillator equations," *J. Appl. Phys.* **33**, 1578-1581 (1962).
- [7] C. L. Tang, "On maser rate equations and transient oscillations," *J. Appl. Phys.* **34**, 2935-2940 (1963).
- [8] V. M. Fain, "On the equations of the oscillations of the molecular generator," *Sov. Phys.-JETP* **6**, 726-729 (1958).
- [9] H. Risken and K. Nummedal "Instability of off resonance modes in lasers," *Phys. Lett. A* **26**, 275-276 (1968).
- [10] H. Risken and K. Nummedal, "Self-pulsing in lasers," *J. Appl. Phys.* **39**, 4662-4672 (1968).
- [11] R. Graham and H. Haken, "Quantum theory of light propagation in a fluctuating laser-active medium," *Z. Phys.* **213**, 420-450 (1968).

- [12] P. Gerber and M. Büttiker, "Stability domain of coherent laser waves," *Z. Physik B* **33**, 219-222 (1979).
- [13] L. M. Narducci, H. Sadiky, L. A. Lugiato, and N. B. Abraham, "Experimentally accessible periodic pulsations of a single-mode homogeneously broadened laser (the Lorenz model)," *Opt. Commun.* **55**, 370- (1985).
- [14] C. T. Sparrow, *The Lorenz Equations: Bifurcations, Chaos and Strange Attractors* (Springer-Verlag, Heidelberg, 1985).
- [15] C. O. Weiss, W. Klische, P. S. Ering, and M. Cooper, "Instabilities and chaos of a single mode  $\text{NH}_3$  ring laser," *Opt. Commun.* **52**, 405-408 (1985).
- [16] W. Klische and C. O. Weiss, "Instabilities and routes to chaos in a homogeneously broadened one- and two-mode ring laser," *Phys. Rev. A* **31**, 4049-4051 (1985).
- [17] E. H. M. Hogenboom, W. Klische, C. O. Weiss, and A. Godone, "Instabilities of a homogeneously broadened laser," *Phys. Rev. Lett.* **55**, 2571-2574 (1985).
- [18] C. O. Weiss and J. Brock, "Evidence for Lorenz-type chaos in a laser," *Phys. Rev. Lett.* **57**, 2804 (1986).
- [19] W. R. Bennet, Jr., "Hole burning effects in a He-Ne optical maser," *Phys. Rev.* **126** 580-593 (1962).  
M. Sargent III, M. Scully, and W. E. Lamb, Jr., *Laser Physics*, (Addison-Wesley, Reading, 1974).
- [20] L. W. Casperson, "Spontaneous coherent pulsations in laser oscillators," *IEEE J. Quantum Electron.* **QE-14**, 756-761 (1978).
- [21] M. Maeda and N. B. Abraham, "Measurements of mode-splitting self-pulsing in a single-mode Fabry-Perot laser," *Phys. Rev. A* **26**, 3395-3403 (1982).
- [22] J. Bentley and N. B. Abraham, "Mode-pulling, and mode-splitting and pulsing in a high gain He-Xe laser," *Opt. Commun.* **41**, 52-56 (1982).

- [23] L. W. Casperson, "Stability criteria for non-Doppler lasers," *Phys. Rev. A* **23**, 248-260 (1981).
- [24] L. Casperson and A. Yariv, "Longitudinal modes in a high-gain laser," *Appl. Phys. Lett.* **17**, 259-261 (1970).
- [25] L. W. Casperson, "Stability criteria for high-intensity lasers," *Phys. Rev. A* **21**, 911-923 (1980).
- [26] R. S. Gioggia and N. B. Abraham, "Single-mode self-pulsing instabilities at the Lamb dip of a He-Ne 3.39  $\mu\text{m}$  laser," *Opt. Commun.* **47**, 278-282 (1983).
- [27] R. S. Gioggia and N. B. Abraham, "Routes to chaotic output from a single-mode dc-excited laser," *Phys. Rev. Lett.* **51**, 650-653 (1983).
- [28] L. W. Hillman and K. Koch, "Multimode instabilities in homogeneously broadened lasers," *Optical Instabilities*, edited by R. W. Boyd, M. G. Raymer, and L. M. Narducci (Cambridge Press, Cambridge, 1986) p. 256-258.
- [29] L. A. Lugiato, L. M. Narducci, E. V. Eschenazi, D. K. Bandy, and N. B. Abraham, "Multimode instabilities in a homogeneously broadened ring laser," *Phys. Rev. A* **32**, 1563-1575 (1985).
- [30] L. A. Westling, M. G. Raymer, and J. J. Snyder, "Single-shot spectral measurements and mode correlations in a pulsed multimode dye laser," *J. Opt. Soc. Am. B* **1** 150 (1984).
- [31] L. A. Westling, M. G. Raymer, M. G. Sceats, and D. F. Coker, "Observations of intensity fluctuations and mode correlations in a broad-band cw dye laser," *Opt. Commun.* **47**, 212 (1983).
- [32] H. R. Gray, "Experimental examination of double optical resonance," University of Rochester, Ph. D. Thesis (1978).
- [33] M. M. Tehrani and L. Mandel, "Intensity fluctuations in a two-mode ring laser," *Phys. Rev. A* **17**, 694-700 (1978).

- [34] R. Roy, R. Short, J. Durnin, and L. Mandel, "First-passage-time distributions under the influence of quantum fluctuations in a laser," *Phys. Rev. Lett.* **45**, 1486-1490 (1980).
- [35] P. Lett, R. Short, and L. Mandel, "Photon Statistics of a dye laser far below threshold," *Phys. Rev. Lett.* **52**, 341-343 (1984).
- [36] P. Lett, "Investigation of first-passage-time problems in the two-mode dye laser," *Phys. Rev. A* **34**, 2044-2057 (1986).
- [37] T. S. Kim, E. C. Gage, and L. Mandel, "Relation between photon statistics and pumping fluctuations in a dye laser," *J. Opt. Soc. Am. B* **5**, 1596-1599 (1988).
- [38] E. C. Gage and L. Mandel, "Investigations of dye-ring-laser statistics with controlled asymmetry," *Phys. Rev. A* **38**, 5166-5173 (1988).  
E. C. Gage and L. Mandel, "Hysteresis effects in the two-mode dye ring laser," *J. Opt. Soc. Am. B* **6** 287-291 (1989).
- [39] H. Fu and H. Haken, "Semiclassical dye laser equations and the unidirectional single-frequency operation," *Phys. Rev. A* **36**, 4802 (1987).
- [40] H. Fu and H. Haken, "Semioclassical theory of dye lasers: the single frequency and multifrequency steady states of operation," *J. Opt. Soc. Am. B* **5**, 899-908 (1988).
- [41] H. Fu and H. Haken, "Multichromatic operation in cw dye lasers," *Phys. Rev. Lett.* **60**, 2614-2617(1988).
- [42] V. S. Mashkevich, *Kinetic Theory of Lasers* (Nauka, Moscow, 1971). (in Russian)
- [43] L. W. Hillman, J. Krasinski, R. W. Boyd, and C. R. Stroud, Jr., "Observation of higher order dynamical states of a homogeneously broadened laser," *Phys. Rev. Lett.* **52**, 1605-1608 (1984).
- [44] C. R. Stroud, Jr., K. Koch, S. H. Chakmakjian, "Instabilities and higher-order states of cw ring dye lasers," in *Optical Instabilities*, edited by R. W. Boyd, M. G. Raymer, and L. M. Narducci, (Cambridge Press, Cambridge 1986) p. 274-276.



- [45] C. R. Stroud, Jr., K. Koch, S. H. Chakmakjian, and L. W. Hillman, "Multimode instabilities in cw dye lasers," in *Optical Chaos* J. Chrostowski, N. B. Abraham, Editors, Proc. SPIE 667, 47-50 (1986).
- [46] K. Berndt and E. Klose, "High-frequency modulation of ar-ion laser radiation due to stable two-mode oscillation," *Opt. Commun.* 35, 417-420 (1980).
- [47] O. L. Gaddy and E. M. Schaefer, "Self-locking of modes in the argon ion laser," *Appl. Phys. Lett.* 9, 281-282 (1966).
- [48] M. Bass, G. deMars, and H. Statz, "Mode interactions in an argon ion laser," *Appl. Phys. Lett.* 12, 17-20 (1968).
- [49] W. H. Keene and J. A. Weiss, "The time-resolved spectrum of a neodymium glass laser," *Appl. Opt.* 3, 545-547 (1964).
- [50] H. Haken, "Analogy between higher instabilities in fluids and lasers," *Phys. Lett.* 53A, 77-78 (1975).
- [51] R. Graham, "Onset of self-pulsing in lasers and the Lorenz model," *Phys. Lett.* 58A, 440-442 (1976).
- [52] E. N. Lorenz, "Deterministic nonperiodic flow," *J. Atmos. Sci.* 20, 130-121 (1963).
- [53] L. Allen and J. H. Eberly, *Optical Resonance and Two-Level Atoms* (John Wiley & Sons, Inc., New York, 1975).
- [54] L. W. Hillman, "Interaction of modulated optical fields with saturable media and its application to laser instability," University of Rochester, Ph. D. Thesis (1984).
- [55] Y. Zhu, A. Lezama, Q. Wu, T. W. Mossberg, "Experimental study of the fluorescence spectrum emitted by two-level atoms under strong bichromatic excitation," Sixth Rochester Conference on Coherence and Quantum Optics, Rochester, NY 1989.
- [56] private communication Lloyd W. Hillman

- [57] W. Ruyten, "Multiphoton resonances in the modulated fluorescence from an inhomogeneously broadened medium," *Opt. Lett.* **14**, 506-508 (1989).
- [58] E. T. Whittaker and G. N. Watson, *Modern Analysis* (Cambridge University Press, Cambridge, 1965).
- [59] S. H. Chakmakjian, K. Koch, and C. R. Stroud, Jr., "Observation of resonances at the subharmonics of the Rabi frequency in the saturated absorption of a 100% amplitude-modulated laser beam," *J. Opt. Soc. Am. B* **5**, 2015-2020 (1988).
- [60] H. Risken and H. D. Vollmer, "Solutions and applications of tridiagonal vector recurrence relations," *Z. Phys. B* **39**, 339-346 (1980).
- [61] K. Koch, B. J. Oliver, S. H. Chakmakjian, C. R. Stroud, Jr., and L. W. Hillman, "Subharmonic instabilities in resonant interactions with bichromatic fields," *J. Opt. Soc. Am. B* **6**, 58-65 (1989).
- [62] Y. Pomeau, B. Dorizzi, and B. Grammaticos, "Chaotic Rabi oscillations under quasiperiodic perturbation," *Phys. Rev. Lett.* **56**, 681-684 (1986).
- [63] J. Eidson and R.F. Fox, "Quantum chaos in a two-level system in a semiclassical radiation field," *Phys. Rev. A* **34**, 3288-3292 (1986).
- [64] R. Badii and P.F. Meier, "Comment on 'Chaotic Rabi oscillations under quasiperiodic perturbation'," *Phys. Rev. Lett.* **58**, 1045 (1987).
- [65] Y. Band, D. F. Heller, J. S. Krasinski, "Spectrum of three-wave mixing for multimode fields," *Phys. Rev. A* **40**, 4400-4403 (1989).
- [66] F.A. Hopf, "Erratic motion in a convective optical flow," *Phys. Rev. Lett.* **56**, 2800-2803 (1986).
- [67] L. D. Landau and E. M. Lifschitz, "Fluid Mechanics" (pergamon Press, London, 1959).
- [68] D. Ruelle and F. Takens, "On the nature of turbulence," *Commun. Math. Phys.* **20**, 167-192 (1971).

- [69] S. Newhouse, D. Ruelle, and F. Takens, "Occurrence of strange axiom A attractors near quasi-periodic flows on  $T^m$ ,  $m \geq 3$ ," *Commun. Math. Phys.* **64**, 35-40 (1978).
- [70] C. Grebogi, E. Ott, S. Pelikan, and J.A. Yorke, "Strange attractors that are not chaotic," *Physica* **13D**, 261-268 (1984).
- [71] C. Grebogi, E. Ott, and J.A. Yorke, "Are three-frequency quasiperiodic orbits to be expected in typical nonlinear dynamical systems?," *Phys. Rev. Lett.* **51**, 339-342 (1983).
- [72] C. Grebogi, E. Ott, and J.A. Yorke, "Attractors on an N-torus: quasiperiodicity versus chaos," *Physica* **15D**, 354-373 (1985).
- [73] A. Libchaber, S. Fauve, and C. Laroche, "Two-parameter study of the routes to chaos," *Physica* **7D**, 73 (1983).
- [74] S. Martin, H. Leber, and W. Martienssen, "Oscillatory and chaotic states of the electrical conduction in BSN crystals," *Phys. Rev. Lett.* **53**, 303 (1984).
- [75] P. Grassberger and I. Procaccia, "Estimation of the Kolmogorov entropy from a chaotic signal," *Phys. Rev. A* **28**, 2591-2593 (1983).
- [76] A. M. Fraser and H. L. Swinney, "Independent coordinates for strange attractors from mutual information," *Phys. Rev. A* **33**, 1134-1140 (1986).
- [77] D. J. Gauthier, "Instabilities and chaos of laser beams propagating through nonlinear optical media," University of Rochester, Ph. D. Thesis 1989.
- [78] M. Hénon, "A two-dimensional mapping with a strange attractor," *Commun. Math. Phys.* **50**, 69-77 (1976).
- [79] A. Wolf, J. B. Swift, H. L. Swinney, and J. A. Vastano, "Determining Lyapunov exponents from a time series," *Physica* **16D** 285-317 (1985).
- [80] K. Koch, S. H. Chakmakjian, S. Papademetriou, and C. R. Stroud, Jr., "Modulation mixing in a multimode dye laser," *Phys. Rev. A* **39** 5744-5750 (1989).

- [81] A. L. Gaeta, R. W. Boyd, J. R. Ackerhalt, and P. W. Milonni, "Instabilities and chaos in the polarization of counterpropagating light fields," *Phys. Rev. Lett.* **58**, 2432-2435 (1987).  
Y. Silberberg and I. Bar Joseph, "Instabilities, self-oscillation, and chaos in a simple nonlinear optical system," *Phys. Rev. Lett.* **48**, 1541-1543 (1982).  
D. J. Gauthier, M. S. Malcuit, and R. W. Boyd, "Polarization instabilities of counterpropagating laser beams in sodium vapor," *Phys. Rev. Lett.* **61**, 1827-1830 (1988).
- [82] private communication N. M. Lawandy
- [83] J. A. Valdmanis and R. L. Fork, "Design considerations for a femtosecond pulse laser: balancing self phase modulation, group velocity dispersion, saturable absorption, and saturable gain," *IEEE J. Quantum Electron.* **QE-22**, 112-118 (1986).
- [84] F. P. Schafer, B. B. Snavely, C. V. Shank, E. P. Ippen, K. H. Drexhage, and T. W. Hänsch, *Dye Lasers* edited by F. P. Schafer (Springer-Verlag, Berlin 1977).
- [85] A. Yariv, *Introduction to Optical Electronics* (Holt, Rinehart and Winston, New York 1976).
- [86] A. Laubereau and W. Kaiser, "Vibrational dynamics of liquids and solids investigated by picosecond light pulses," *Rev. Mod. Phys.* **50**, 607-665 (1978).
- [87] D. Ricard and J. Ducuing, "Vibrational relaxation in the ground electronic state of large organic molecules in solution," *J. Chem. Phys.* **62** 3616-3619 (1975).